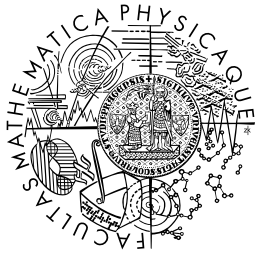

FACULTY
OF MATHEMATICS
AND PHYSICS
Charles University

MASTER THESIS

Dalibor Preisler

Oxygen-strengthened biomedical beta titanium alloys

Department of Physics of Materials

Supervisor of the master thesis:	PhDr. RNDr. Josef Stráský, Ph.D.
Study programme:	Physics
Study branch:	Physics of Condensed Matter and Materials

Prague 2018

I declare that I carried out this master thesis independently, and only with the cited sources, literature and other professional sources.

I understand that my work relates to the rights and obligations under the Act No. 121/2000 Sb., the Copyright Act, as amended, in particular the fact that the Charles University has the right to conclude a license agreement on the use of this work as a school work pursuant to Section 60 subsection 1 of the Copyright Act.

In ..... date ..... signature of the author

Title: Oxygen-strengthened biomedical beta titanium alloys

Author: Dalibor Preisler

Department: Department of Physics of Materials

Supervisor: PhDr. RNDr. Josef Stráský, Ph.D., Department of Physics of Materials

Abstract: Beta titanium alloy Ti-35Nb-6Ta-7Zr-0.7O (wt.%) exhibit a low Young's modulus and high strength thanks to interstitial strengthening effect of oxygen. These mechanical properties are promising for implant production. In this thesis, the aforementioned alloy is thoroughly studied in conditions prepared by various thermomechanical treatments, namely: material after casting, hot compression testing, die-forging, hot rolling and finally, cold-swaged and annealed condition. Mechanical properties and microstructure of prepared conditions are studied with special interest of enhancing the fatigue performance that is poor after casting due to porosity and large grains. Both the die-forging and hot rolling improve the fatigue performance significantly, mainly through grain refinement. It is shown that by combining the effects of cold-swaging and recrystallization annealing, extensive refinement of grain structure can be achieved. Industrial aspects of implant production are discussed. In the second part of the thesis, the possibility of lowering the Young's modulus by reducing the beta phase stability (by reducing of Nb and Ta content), while retaining high strength caused by interstitial oxyen is explored. Several alloys are produced and their microstructure and mechanical properties are characterized. It is found and discussed that the Young's modulus is indeed suppressed by low Ta and Nb content while the strength remains very high.

Keywords: Titanium alloys, Thermomechanical processing, Phase stability, Microstructure, Mechanical properties

I would like to thank several people. First of all, thanks to Josef Stráský, the thesis supervisor, for providing the subject of the thesis, leading me at my work and discussing all the related topics. It was a pleasure to study under his lead. I also thank: Petr Harcuba for teaching me how to operate the scanning electron microscope and for his advices; other colleagues from the titanium group for any help they provided; Jana Kálalová for help with sample preparation and all many others from Department of Physics of Materials.

The Grant Agency of Charles University is acknowledged for the financial support (project no. 1530217).

Contents

Introduction

This thesis is based on results that emerged during master studies of the author at Department of Physics of Materials in years 2016 – 2018. The title of the thesis is *Oxygen-strengthened biomedical beta titanium alloys* and its main topic is studying and development of materials for use in medicine. The work was done at cooperation with companies Beznoska, s.r.o. and COMTES FHT, a.s. under joint project TRIO (FV20147) of Ministry of Industry and Trade of Czech Republic. Company Beznoska is major producer of medical implants in Czech Republic and also the studied materials – titanium alloys Ti-Nb-Ta-Zr-O are mainly intended for implant manufacturing.

In the first chapter, literature overview with special emphasis on general properties of medical implants and titanium alloys are provided. Second chapter formulates the aims of this thesis. Prepared materials and conditions are summarized in chapter 3 and experimental techniques together with sample preparation routes are in chapter 4.

Two chapters contain the Results and Discussion. Chapter 5 presents results from thermomechanical processing of alloy Ti-35Nb-6Ta-7Zr-0.7O (wt. %), developed in previous research on Department of Physics of Materials. Special emphasis is put on improvement of fatigue resistance of this alloy. Chapter 6 presents results from the development of new alloys based on the aforementioned composition, but with reduced Nb and Ta content. The aim of the development further improvement of the material.

Several experimental techniques was used for obtaining the results. Most of them were performed by the thesis author at the Department of Physics of Materials, incl. scanning electron microscopy observations (and electron backscatter diffraction), microhardness measurements, tensile testing and acoustic resonance spectroscopy (ARS). Hot compression testing was done by the author at TU Graz, Austria.

Fatigue testing was done by company Beznoska and ultasound resonant spectroscopy (RUS) was performed by Institute of Thermomechanics, Czech Academy of Sciences.

1. Literature overview

1.1 Materials for total joint endoprostheses

Joint replacement surgery (hip, knee and elbow) is one of the most challenging medical operations that are performed today, from the perspective both of a surgeon and his skills but also from the requirements that are imposed on the material of the implant. One of the major reasons of hip or knee replacement need is osteoarthritis caused mainly by high age, obesity, physical inactivity, excessive alcohol, etc. These reasons will decrease the age of the first implant operation and with increasing life expectancy [1], the implant service life needs to be extended. In 2014, 189 hip and 130 knee replacements were performed in EU per 100 000 people and these numbers are rising each year [2].

Hip joint implant consists of several components called cup, liner, head/ball and stem, connecting to each other. The most loaded part of them is the stem that is inserted into a drilled hole in the femur [3]. Implant failure, it is most often caused by the stem. Five most common reasons of implant failure or re-operation are: mechanical loosening due to osteoporosis (42%), periprosthetic fracture - bone fracture (12%), infection (11%), wear and osteolysis - body rejection of the implant (11%) and dislocation (10%) [4]. Most of them are connected either to mechanical or chemical/biological compatibility of the implant. Let us now characterize, the desired mechanical and chemical properties of an implant material.

1.1.1 Desired properties of the material

The material that becomes long-term part of a human's body needs to be chemically inert in body fluids to prevent corrosion and other chemical reactions. Excellent biocompatibility is also desired as the body itself should accept the implant as its natural part.

From the mechanical properties viewpoint, it is essential for the implant to have the high strength [5] of at least 800 MPa. This requirement allows the construction of smaller implants and is closely connected with the need of high fatigue performance. If a person walks 2700 steps per day (this is actually near the lower limit of recommended steps per day for older healthy adults that ranges from 2000 to 9000 [6], but it corresponds to average number of steps of people with hip joint replacement [5]), then it makes almost ten million steps in ten years. This also corresponds to the number of cycles to determine the fatigue limit of the materials (maximum stress on which the material can withstand ten million cycles). In order to extend the life of such implant to be usable also by younger people, fatigue limit needs to be enhanced.

Next mechanical property of a material crucial for osseointegration of the implant is the Young's modulus (YM). The bone itself has the YM of 5 GPa–30 GPa, depending on type of bone tissue (cortical tissue is generaly stiffer than trabecular tissue) [7, 8]. If an implant with much higher YM than that of a bone is used, the so-called stress shielding effect can arise [9, 10]. The implant is then absorbing much more load than the bone. As a consequence, due to lack

of mechanical stimulation, this leads to osteoporosis caused by bone inactivity, similarly to insufficient physical activity. As stated above, mechanical loosening due to osteoporosis is main factor in implant failure and reoperation. A visualization of a stress-shielding can be observed in Fig. 1.1, which is a result of finite element method (FEM) modelling [11]. Another FEM modelling showed lowering the stress shielding effect while using material with lower YM [12]. Experimental analysis of the effect of different Young's moduli on recovery of fractured bone can be found in [13]. The lower the YM, the better and faster recovery of the bone.

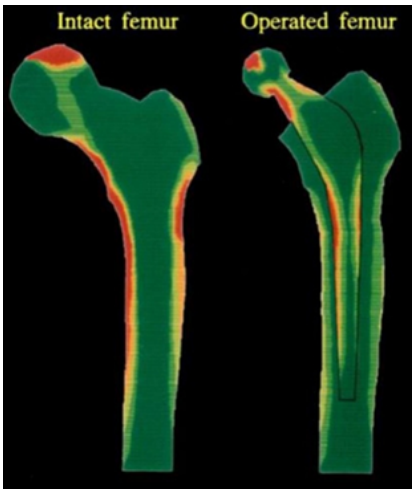

Figure 1.1: Stress distribution in intact femur (left) and operated femur with hip implant (right) [11].

Last but not least "property" of the final product is obviously the price. The price for a complete process including the implant manufacturing and following surgery exceeds 5500 EUR (average price in EU countries) [2]. Therefore, new improvements such as newly developed materials and the technology of their preparation (including energy price) could not be too expensive.

1.1.2 Currently used materials

There are three types of materials used for an implant manufacturing: ceramics, polymers and metals. Each of them is used for a different purpose, depending on their properties.

- Polymers, such as ultra-high molecular-weight polyethylene (UHMWP), used in the field, have suitable biocompatibility, YM comparable to a bone but on the other hand, they suffer from low strength and also undergo excessive creeping. Therefore, they are used either as cement for fixation of metallic parts or as a liner for the head/ball of the implant.
- The ceramics (e.g. Al_2O_3) have very high compressive strength but suffer from brittleness and very high YM.
- Metals differ in their properties depending mainly on the composition of the alloy but also in the technology of preparation. Three types of alloys have been used: stainless steel, Co-Cr alloys and titanium alloys.

The stainless steel has high YM (190 GPa) and poor fatigue performance. Therefore it is used only for a short term fixation. Cr-Co alloys have even higher YM (220 GPa) and better fatigue resistance. However, both Co and Cr are considered carcinogens and ion release into body tissue is the main drawback.

Commercially pure titanium (CP Ti) and titanium alloys have many advantages in comparison with the above described materials. They have excellent corrosion resistance thanks to formation of thin TiO_2 layer on the surface and with the appropriate choice of alloying elements, they are bioinert. Both the strength and fatigue resistance are sufficient for use in long-term joint implants.

The most used alloy is Ti-6Al-4V wt. % (all compositions in this work are given in weight %) [12, 14]. This alloy has the YM of 100 – 130 GPa [15] (depending on preparation and heat treatment), that is approx. half than that of stainless steels or Co-Cr alloys, but still, it is at least four times higher than the YM of a bone. Another drawback is the content of toxic V [16] and allegedly neurodegenerative Al [17, 18]. The yield strength (YS) ranges from 830 MPa to 1100 MPa and fatigue limit from 500 MPa to 600 MPa [19, 15]. Properties depend on the heat treatment that produces the final microstructure.

To summarize this section, there is still a potential for improvement of the materials for implant manufacturing. Firstly, through use of purely biocompatible alloying elements, secondly through further lowering of YM closer to that of a bone and finally by improvement of the fatigue performance. Let's now describe the properties of Ti alloys in more detail.

1.2 Titanium alloys

Titanium was discovered in 1791 in an Ilmenite mineral ($FeTiO_3$) but it took till 1910 to isolate it as a pure element. Due to this reason, Ti obtained its name after Titans, gods from the Greek mythology. Today, Ti is produced by the so-called Kroll process, using the rutile ore (TiO_2) or ilmenite. Ti has atomic number 22 and is located in the fourth group of periodic table among other transition metals. The electron configuration [Ar] $3d^2$ $4s^2$, therefore Ti has 4 valence electrons. For a number of convenient properties including low weight (density of $4.5\,\mathrm{g\,cm^{-3}}$), Ti is used as a structural material in the areas such as aircraft manufacturing (engines), dental and joint implant manufacturing, petrochemical industry (corrosion resistant tubes) and also jewelry. However, some large scale expansion to other fields, e.g. automobile industry, is limited due to the high price of Ti and its processing.

After solidification at 1668 °C, the pure Ti crystallizes in high temperature body centered cubic (bcc) structure – the β phase. Upon cooling down to room temperature (RT), the β phase transforms into the hexagonal close-packed (hcp) structure – the α phase, with c/a=1.587 at a temperature called β transus temperature (882 °C for pure Ti). The α phase is harder and has a higher YM than the β phase. Various elements can have different effect on the β transus temperature as indicated in schematic diagrams in Fig. 1.2 [20].

- The α stabilizers increase the β transus temperature. The most important α stabilizer is Al that is used in an important class of Ti-based materials, titanium aluminides. Other α stabilizers are O, N and C.

- β stabilizers reduce the β transus temperature. Some of them are the so-called isomorphous β stabilizers, such as Mo, V, Nb and Ta, and pure β phase composition can be achieved with sufficient alloying. The other group of β stabilizers are eutectoid elements that are not fully soluble and upon reaching the miscibility gap, they form the intermetallic compounds with Ti.

- Some elements, such as Zr or Sn, do not have a significant impact on the β transus temperature. However, they can possibly affect the resulting alloy in combination with other alloying elements or in a different manner than the α–β phase stability.

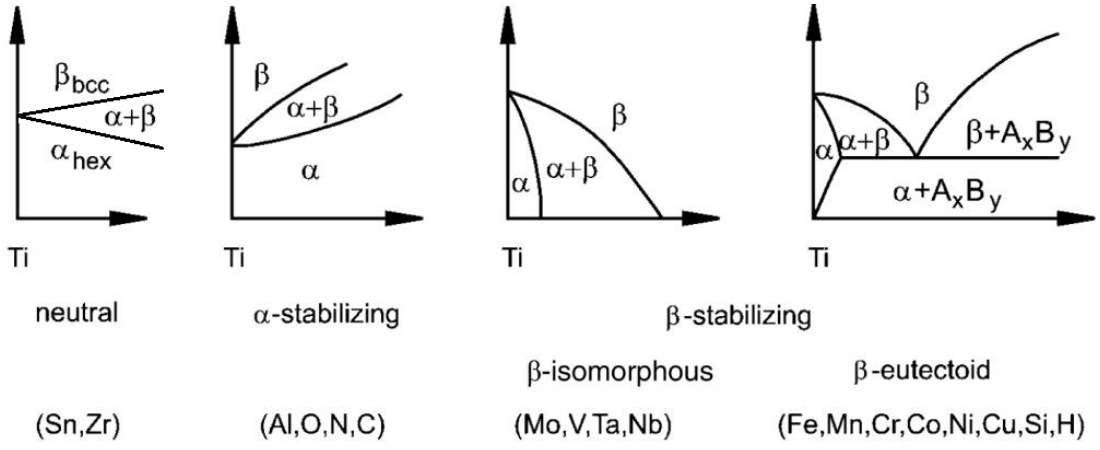

Figure 1.2: Schematic phase diagrams for neutral, α stabilizing and β stabilizing elements [20].

Phase diagram of Ti with isomorphous β stabilizers will be described in detail below.

1.3 Beta titanium alloys - properties and behaviour

In order to quantify the β stabilizing effect of individual elements, the so called Mo equivalence has been created for comparison of their wt.% content in Ti, needed for avoiding the martensitic transformation and retaining the pure β phase at RT [21].

$[Mo]_{eq} = [Mo] + 0.67[V] + 0.44[W] + 0.28[Nb] + 0.22[Ta] + 2.9[Fe] + 1.6[Cr] + 1.25[Ni] + 1.7[Mn] + 1.7[Co]$–$1.0[Al]$

For Mo, the stabilization occurs at the concentration of 10%. The stabilizing concentration of other elements in binary alloys can be computed from the above equation. The negative coefficient before aluminum reflects its α stabilizing effect. However, this equation should not be used for more complex alloys (ternary, quaternary), as the alloying elements can affect each other and their stabilizing effect can be either suppressed or even enhanced.

1.3.1 Metastable phases and phase transformations

The pseudo-binary phase diagram common for Ti and any of the isomorphous β stabilizing elements is shown in Fig. 1.3 [20]. This phase diagram allows us to divide Ti alloys into three groups according to equilibrium phase composition at RT. In α alloys, there is not enough β stabilizing elements and therefore, only the α phase is present. With increasing the β stabilizing content, there are the α+β alloys, that are separated from metastable β alloys by the intersection of dashed line denoting the start of a martensitic temperature with RT. In metastable β alloys, pure β phase can be obtained by solution treatment (ST) the β region and water quenching (WQ) down to RT. With even higher content of the β stabilizer, pure β phase is stabilized and then we obtain β alloys.

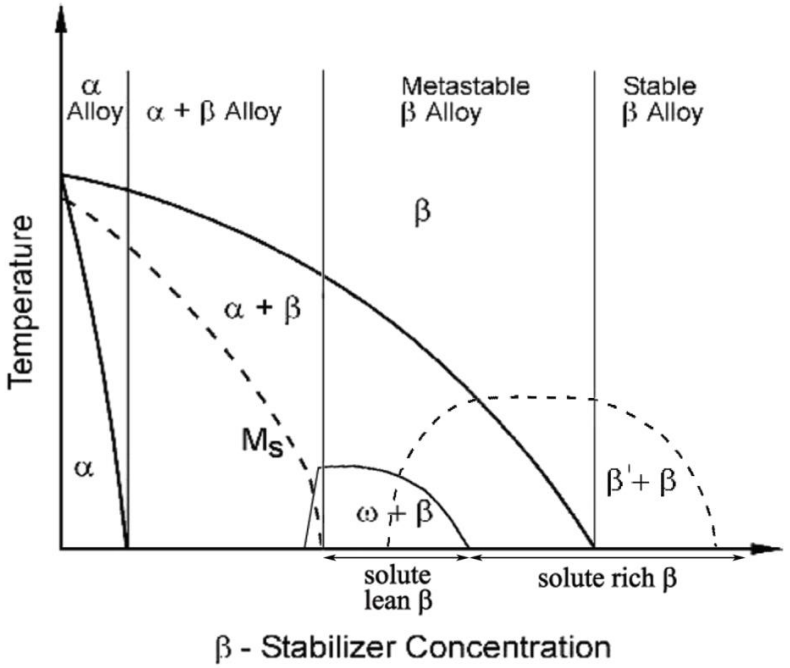

Figure 1.3: Pseudo-binary phase diagram of Ti with an isomorphous alloying element [20].

In addition to the α and β phase, several metastable phases can be formed by the appropriate processing:

- Quenching of the α+β alloys from β region to RT results in the formation of lamellar metastable α' martensite with hcp structure [19] that is supersaturated with β stabilizers. Upon annealing in the α+β region, this phase can be decomposed to equilibrium mixture of α and β phase [22].

- After ST of the metastable β alloys, supersaturated β phase is obtained, often containing some other metastable phases. Upon aging in the α+β region, the α phase precipitates heterogeneously on β-β grain boundaries (GBs) and homogeneously as Widmanstätten lamellar structure inside the β grains due to different misfits on the α-β interfaces until equilibrium phase composition is achieved [23]. This lamellar structure is harder and stronger than other α-β morphologies [15].

- Another metastable phase is the hexagonal (although not hcp) ω phase that can form either upon quenching (the so-called athermal ω) or upon annealing of the quenched metastable β alloy (isothermal ω) [24]. This phase is stiff and brittle. The athermal ω exists in the form of small ellipsoidal or cuboidal particles with the size of nanometers. The isothermal ω particles are about one order of magnitude bigger (tens of nm). The ω phase can exist only in low β stabilized alloys (close to martensitic transformation).

- In highly stabilized yet metastable β alloys, the phase separation into two bcc phases can occur during quenching, namely a solute rich and a solute lean β phase with higher and lower content of β stabilizing element, respectively [19].

- The phase diagram in Fig. 1.3 does not show the last common phase found in metastable β Ti alloys which is the α" martensitic phase. This phase has an orthorhombic structure and frequently it forms during deformation (as a stress induced martensite - SIM). It can be also present even after ST (enhanced by stress formed during quenching). A special pseudo-elastic deformation behavior such as super-elasticity and shape memory is connected to martensitic phase transformation $\beta \leftrightarrow \alpha$" [25, 26, 27, 28, 29, 30].

The material exhibits super-elasticity when large amount of apparent elastic strain (up to few percent) can be stored by the transformation of highly symmetrical austenite into low-symmetry martensite upon loading. After unloading, the original or nearly original shape is restored by reverse transformation. Shape memory effect is similar to super-elasticity, but after unloading, the shape is not restored and SIM remains in the material until heated to sufficient temperature, when reverse transformation into austenite occurs and original shape is restored. Both these effects are favorable for use in medical instruments (easy shaping and restoring the original shape), but not for implant production (uncontrollable changes of shape of the implant during loading).

1.3.2 Young's modulus and phase stability

The phases described at previous subsection differ in their properties and therefore they may significantly affect the resulting material.

The α phase has the Young's modulus ranging between 110 GPa – 130 GPa and relatively high hardness. On the other hand, the β phase has the Young's modulus ranging between 50 GPa – 80 GPa, depending on the stability, i.e. the content of β stabilizers [31]. The β phase stability is closely connected with the ratio of valence electrons per atom (e/a) [32, 33].

Fig. 1.4 shows schematic dependence of Young's modulus on the e/a ratio. From the value e/a=4 that corresponds to pure Ti or α phase, the Young's modulus drops until a minimum is reached. This corresponds to $\beta + \alpha$" phase mixture that shows the apparent Young's modulus about 60 GPa. In this case, the deformation induced $\beta \rightarrow \alpha$" transformation that causes the super-elasticity or shape memory. With rising content of β stabilizers, i.e. with higher e/a ratio – the β, α" and ω phases coexist and because the stiff ω phase (YM around 160 GPa [34]), the overall YM rises [35]. With more stabilization, the ω and α" phases are

no longer present and YM reaches another minimum retaining the pure β phase at e/a=4.24. Rising the e/a ratio results in the final increasing YM. The peak caused by ω phase formation can be avoided under special circumstances and then the YM–e/a dependence follows dotted line with a minimum under e/a=4.15. The explanation given in [33] is a nano-scale chemical concentration variations that are smaller than the ω phase particles and thus inhibit their formation.

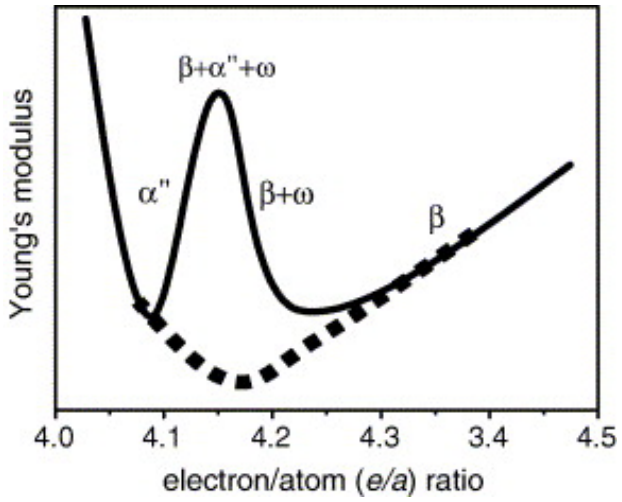

Figure 1.4: Dependence of Young's modulus on e/a ratio in β Ti alloys [32].

1.4 Ti-Nb-Ta-Zr-O system

One of the most studied β Ti systems with the perspective of the use in medicine are alloys with Nb, Ta and Zr. All alloying elements are highly biocompatible [36] and consequently the final alloying systems show biocompatibility and also corrosion resistance [37, 38, 39]. Several compositions were reported, that exhibit very low YM without the α" or ω phase formation (not even as a SIM). One example is the alloy with the composition Ti-35.3Nb-5.7Ta-7.3Zr [40]. This alloy has the Young's modulus of 63 GPa in the ST condition but its YS reaches only 450 MPa [41], which is significantly inferior to the Ti-6Al-4V benchmark alloy and to YS needed for implant manufacturing.

With the addition of 0.7% of oxygen, the YS can be increased to a satisfactory value over 1000 MPa. However, the YM also increases to a value of 80 GPa [41, 42], which is still significantly lower than that of Ti-6Al-4V alloy. This alloy with the composition Ti-35.3Nb-5.7Ta-7.3Zr-0.7O is the main subject of this thesis and will be denoted shortly as TNTZO. Let us now look on how the individual elements influence the alloy properties.

1.4.1 Effects of alloying metals

According to the Mo equivalency, the Nb and Ta are β stabilizers whereas Zr is a neutral element. Both Nb and Ta were found to strengthen the alloys by substitutional solid solution strengthening mechanism [43, 44].

It was found that both ω and α" phase formation can be hindered by Zr content [31]. However, Zr has only little effect on the strength or other mechanical properties of the β Ti alloys [45].

1.4.2 Oxygen content

Interstitial atoms of oxygen have a significant impact on the β Ti matrix. Following effects are caused by oxygen in TNTZO alloy:

- High strength. Although mostly studied Ti-Nb based alloys contain 0.3% – 0.5% of O [29, 46, 47, 48, 30], the addition of 0.7% O have doubled the YS of Ti-35.3Nb-5.7Ta-7.3Zr [27, 41, 49]. The value of 1000 MPa is achieved in forged material [41] by interaction of the interstitial oxygen atoms with dislocations through pinning effect in the stress field of oxygen called Cottrell atmosphere, initially observed in Fe with carbon interstitials [50].

- Sharp yield point and deformation strengthening. Together with the strengthening effect, the interaction of oxygen with dislocations causes a sharp yield point in the stress-strain curve and also produces a significant deformation strengthening and high ductility of the alloy (the true plastic strain $> 10\%$).

- Higher β phase stability and higher YM [48]. Concurrently with the strengthening effect, the YM also increases to 80 GPa, probably because of higher stabilization of the β phase by oxygen with respect to α" phase transformation (higher e/a ratio as oxygen has 6 valence electrons). The stabilization can be even higher than oxygen content suggests, because as an interstitial element, the electrons are added to electron gas of the alloy but the number of atoms in lattice sites remains the same as without the oxygen. Enhanced oxygen content was reported to hinder both ω [48] and α" [51] phase formation.

- Deformation mechanism. The oxygen content increases the critical stress for twinning [25]. As a consequence, dislocation slip is the preferred mode of deformation.

- Clustering around Zr. Another effect of oxygen is connected with Zr content. Oxygen nano-clustering around Zr atoms was reported to cause obstacles for dislocation motion and thus another strengthening in cold-worked material [52].

1.4.3 Thermomechanical processing

The TNTZO alloy developed during the doctoral studies of thesis supervisor exgibits the potential in replacing the currently used Ti-6Al-4V alloy. However, the right thermomechanical (TM) treatment has to be established for practical use of this alloy as an implant material. Different approaches of TM processing will be studied in this thesis. Therefore, some aspects of TM processing will now be reviewed with respect to TNTZO forming.

In general, the TM processing is the application of heat and deformation aiming to change the shape and structure of the material. The shape can be changed primarily when the metallic material is heated to sufficiently high forming temperature. Another effect that can be achieved during deformation is the multiplication of dislocations (or deformation twinning in certain cases). High dislocation density causes higher strength, but also reduces the ductility and formability of the material.

There are also thermally activated mechanisms of reducing the dislocation density: recovery and recrystallization. Recovery refers to a process, when dislocations annihilate and also form dislocation walls (subgrain formation). The driving force for recovery is the reduction of the dislocation density and consequently also reducing total energy of the material. Recovery can be either static or dynamic: the dynamic recovery reduces the dislocation density while forming the material and thus allows further deformation. On the other hand, the static recovery is achieved by annealing of previously deformed material. The temperature for diffusion controlled recovery has to be higher than 0.3 T_m (T_m – melting temperature) [53].

Another way, how the material can reduce its dislocation density is the recrystallization. Recrystallization refers to the formation of refined grains in the deformed structure. This is the main difference from the recovery. Recrystallization can be static and dynamic, analogically to the recovery. On the other hand, recrystallization can be either continuous or discontinuous. Discontinuous (or primary) recrystallization is characterized by the formation of new grains that nucleate in heavily deformed nucleation sites (with locally high dislocation density). These newly created grains have high misorientation from the maternal grains. The continuous recrystallization occurs when dislocation walls emerged from recovery achieve a misorientation high enough to form a refined grain structure.

The last thermally activated process is the grain growth. This process occurs when the structure is recovered or recrystallized and thus the driving force is not reducing the dislocation density but rather reducing of GB fraction in the material.

The material property that controls, whether the recovery or recrystallization will occur, is called stacking fault energy (SFE). It governs the distance of partial dislocations — when the partials are sufficiently separated (low SFE), then cross-slip is inhibited and material undergoes the recrystallization rather than recovery. In case of low or no separation of the partials (high SFE), recovery is preferred over recrystallization while heating the deformed material. β Ti alloys have high stacking fault energy [54] and the TM processing has to be adapted while considering this fact. Preferring of the recovery was confirmed also experimentally [55, 56]. Therefore, if we want the deformed material to recrystallize, rather high temperatures and high deformations have to be used.

Very high dislocation densities can be achieved through cold working (CW), that refers to the deformation of the material under 0.3 T_m, which prevents the dynamic recovery. Many papers were published concerning CW, either cold-rolling (CR) or cold-swaging (CSW), of the TNTZO-type alloys. One of the most famous is the alloy called "Gum Metal" (Ti-35Nb-2Ta-3Zr) [57]. Its name reflects the low YM it possesses. The preparation of this alloy into low-YM state involves

CW. It was argued that this alloy undergoes dislocation-free plastic deformation and this allows having low YM and high strength at the same time [58]. The dislocation-free deformation was supposedly possible by the formation of "giant faults" (β transformed to α" in nanodomains) in the material [59]. However, later, the dislocations were found in this material [60]. Low YM is caused by high density of dislocations and GBs or the formation of strong 110 texture [61] considering anisotropy of single crystalline β Ti [35].

It is also possible to recrystallize the deformed microstructure at sufficiently high temperatures (to avoid recovery). The Gum Metal was reported to have the minimum recrystallization temperature (under which primarily recovery occurs) of about 820 °C [61]. Note that this temperature depends on the melting point of each alloy and needs to be established first for new materials.

1.4.4 Low Young's modulus + high strength alloys design

The development of new alloys based on TNTZO is described in the second part of this thesis. As it was mentioned in previous sections, the area of research of Ti-Nb-Zr-Ta-O based alloys strengthened by various amounts of oxygen is very wide and many papers have been published on the phase composition, microstructure, mechanical properties and also biocompatibility of this type of alloys. For further development, a review of these properties has been made during fall 2016 before designing new alloys. The table summarizing this review can be found in the attachment 1 of this thesis. Based on this review, new alloys were designed and produced. The design idea will now be shortly described.

Majority of the alloys contains 0.3% – 0.5% of oxygen. This provides interstitial solution strengthening and with the help of cold working, very low YM is achievable together with high YS. On the other hand, elongation suffers from the lack of formability of the cold worked material.

Few developed alloys have oxygen content higher than 0.5% (such as the TNTZO [41]). The TNTZO alloy exhibits extraordinary high strength exceeding 1000 MPa, deformation strengthening, elongation around 10% and pure β phase already in the ST condition. The YM, on the other hand, is raised by the high oxygen content from 65 GPa to 80 GPa.

The rise of YM is attributed to the rise of e/a ratio caused by interstitial oxygen. The next logical step was therefore the lowering the e/a ratio while preserving the oxygen content at the same level. This was achieved by lowering the content of β stabilizing elements (Nb, Ta – both have 5 valence electrons). Zr content was maintained the same because firstly, it has 4 valence electrons as Ti, and, more importantly, possible nano-clustering of O atoms around Zr could cause the strengthening in TNTZO alloy. Lowering Nb and Ta content was done in favor of the Ti content. This has also a positive impact on the final price of the material, since Nb is 8× more expensive and Ta is 30× more expensive than Ti [62].

Final elemental contents of newly developed and studied alloys with high oxygen content of 0.7% are specified in the section 3.4, describing the preparation of materials.

2. Aims of the thesis

This diploma thesis has two aims. Each of them is divided into several tasks necessary for fulfilling the aim.

1. Characterization of Ti-35Nb-6Ta-7Zr-0.7O (TNTZO) alloy after various thermome-chanical (TM) treatments.
    - Experimental characterization of the cast material.
    - Investigation of the formability and deformation mechanisms at elevated temperatures, discussion of results and proposing the ways of TM treatment of TNTZO alloy.
    - Characterization of microstructure and mechanical properties of the material prepared by three methods: die-forging, hot rolling and cold-swaging with subsequent annealing. Discussion with respect to correlation of microstructure and mechanical (fatigue and tensile) properties.
    - Comparison of prepared conditions TNTZO alloy and proposing the most feasible processing route to achieve material for implant manufactuing.
2. Development of new alloys with high strength and low Young's modulus (YM).
    - Designing of alloys based on initial TNTZO alloy. Lower Nb and/or Ta content is used for achieving low YM and while concurrently retaining high oxygen content to achieve high strength.
    - Characterization of produced alloys by microstructural observations, tensile testing and microhardness measurements and YM measurements.
    - Discussion of achieved properties in comparison to the initial TNTZO alloy. Selection of the best alloy composition for an implant manufacturing.

3. Studied materials and their preparation

3.1 Casting of initial TNTZO alloy

The initial material with the composition Ti-35.3Nb-6.7Ta-7.3Zr-0.7O was cast at the company Retech Systems LLC, USA in May 2015 by the following procedure. In the first stage, Ti and Zr sponge, Nb and Ta pieces and TiO_2 powder were weighted and compacted into approx. 2 kg pieces by plasma arc melting. These compacts were subsequently remelted in pure He atmosphere by the so-called sequential pour melting process, yielding a rod with the diameter of 55 mm and the length of approx. 1 m. The approximate melting temperature of the TNTZO alloy is estimated to lie between 1800 °C and 1900 °C. This rod served as input material for all processing procedures that will be described below. Solution treatment was not needed as this condition already contains pure β phase [63, 64].

3.2 Hot compression testing

In order to analyze deformation behavior of the cast TNTZO alloy during deformation at elevated temperatures, hot compression tests were performed.

Gleeble 1500 machine equipped with a servo-hydraulic system was used for the testing. The testing was done at TU Graz by the author of this thesis. Cylindrical samples with the diameter of 8 mm and the length of 12 mm were cut from the cast ingot for this purpose. Two types of test were performed: single hit and double hit. Table 3.1 summarizes conditions and routes of produced samples.

Table 3.1: Conditions of hot compression testing.

Single hit experiments: deformation to strain 0.5			
Strain rate	Deformation temperatures		
0.01/s	800 °C	900 °C	1000 °C
	1100 °C	–	–
1/s	800 °C	900 °C	1000 °C
	1100 °C	1300 °C	1400 °C
Double hit experiments: two deformations with intermediate annealing			
Strain rate	First deformation	Annealing	Second deformation
0.01/s	400 °C, strain 0.3	1000 °C / 15 min	400 °C, strain 0.6
		1200 °C / 15 min	

Maximum heating rate of 5 K/s (300 K/min) was used. After end of deformation sequence all samples were water quenched. Cooling rate before second deformation in the case of double hit experiments was also 5 K/s. The tests were conducted in Ar atmosphere. The true stress-strain curves were recorded in-situ.

3.3 Thermomechanical processing of the cast alloy

Several techniques of TM treatment were used to process the cast ingot. Table 3.2 summarizes the material prepared in the form of circular rods.

Detailed descriptions of the used TM treatments follow in the next sections. The amount of material prepared by die-forging and hot rolling was sufficient to both tensile and fatigue testing. The fatigue testing is very material demanding since multiple samples have to be measured at different stress amplitudes.

Table 3.2: TM processed material in form of circular rods.

TM treatment	Prepared rod diameters (area reductions)		
Die-forging	35 mm (40%)	25 mm (70%)	–
Hot rolling	33 mm (65%)	25 mm (80%)	20 mm (87%)
Cold-swaging series 1	7 mm (40%)	5.4 mm (65%)	4.1 mm (80%)
Cold-swaging series 2	8 mm (72%)	7 mm (78%)	6.4 mm (82%)
Recrystallization annealing	Prepared conditions specified in table 3.3		

3.3.1 Die-forging

Forging is one of the oldest technologies used for metal working. It has two main functions: to shape a piece of metal into desired shape and also to cause microstructural changes that affect macroscopic mechanical properties. The microstructural changes can include: work hardening caused by dislocation multiplication, dynamic recovery or dynamic recrystallization. Although the desired shape can be achieved only by forging with a hammer and anvil, as it was done for centuries. Another option is forging into a die by a hydraulic press.

Two rods with diameter 35 mm and 25 mm were produced by die-forging at the company ALPER a.s., Prostějov. In the first stage, two piece of initial ingot were machined to 45 mm and heated approx. to 1200 °C in furnace on air (heating took approx. 20 min). The heated pieces were subsequently forged to 35 mm diameter (the process took approx 1 min). The forged rods were cooled in water to 30 °C – 50 °C after forging. One of the forged pieces was reheated back to 1200 °C in furnace and forged to diameter 25 mm. During forging of the second piece, the temperature dropped below approx. 800 °C and this piece had to be reheated again. The piece with diameter 25 mm was accordingly cooled in water to 30 °C – 50 °C.

The final shape of the forged piece was cylindrical for 35 mm rod as it was desired. The 25 mm rod had some material outflow, where the two dies meet, forming a “wings” on each side that had to be cut away.

3.3.2 Hot rolling

The cast TNTZO alloy was processed by hot rolling, resulting in three conditions: rods with diameter 33 mm, 25 mm and 20 mm.

Typically, two cylindrical rolls are in defined distance (lowering until the desired thickness is reached) and a metal is passing through the rolls that impose a work hardening and reduce the thickness. In our case the the initial material had the shape of a cylindrical rod and the rolling was performed with rolls that had grooves for cylindrical rods.

Hot rolling was performed at VŠB TU Ostrava and final rods of diameters 33 mm, 25 mm and 20 mm were produced by the following procedure. Two parts of the initial rod (55 mm in diameter) were heated up to 1200 °C in air for more than 1 h and rolled to the diameter of 33 mm by several rolling passes without reheating. The rod was rotated by 90° after each pass. One of the rods was reheated back to 1200 °C and further rolled to diameter 25 mm by the same procedure. This rod was cut into two pieces and one of them was again heated back to 1200 °C and rolled to the diamete of 20 mm. After the last rod was finished, all three final pieces with diameter 33 mm, 25 mm and 20 mm were cooled in water.

Due to the rolling procedure, each rod cross-section was not exactly round but was elongated in one direction. This allows us to name the positions of samples using the nomenclature from rolling of sheets. The material was studied in three positions as shown in Fig. 3.1 (C - center, T - transversal edge, N - normal edge). The transverse diameters 33 mm, 25 mm and 20 mm correspond to normal diameters of 25 mm, 22 mm and 18 mm, respectively. Each sample will be referred to as by its position and the transversal diameter of the corresponding rod (e.g. C33).

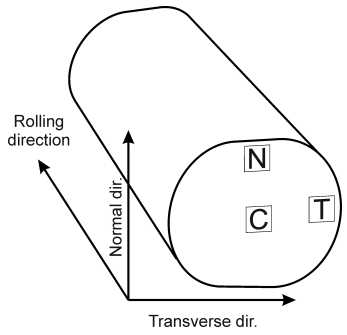

Figure 3.1: Graphical representation of samples positions after hot rolling.

3.3.3 Cold swaging

Cold swaging is performed at RT. The high density of dislocations is introduced during this process because due to low temperature, the thermally activated processes such as recovery are inhibited. Another advantage of cold deformation is that oxidation and oxygen contamination is completely avoided. Cold swaging machine scheme is shown in Fig. 3.2. It consists of four dies that are placed around the cylindrical rod. Each die is connected to a hammer that is brought to motion by rotating rollers inside an outer shell called a liner. The dies can be replaced after each pass in order to reach lower diameter and thus also impose higher deformation.

Cold-swaging and subsequent recrystallization annealing were proposed as possible TM processing for enhancing the mechanical properties by closing pores

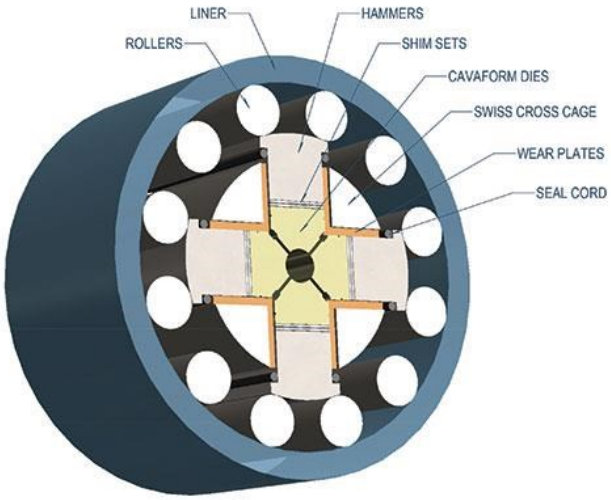

Figure 3.2: Cold-swaging machine scheme [65].

and refining the microstructure.

First try of cold-swaging was performed at UJP Praha a.s. The initial diameters of the rods machined from cast ingot were 9 mm and three final diameters were achieved: 7 mm, 5.4 mm and 4.1 mm which corresponds to approx. 40%, 65% and 80% of area reduction (AR). The samples from series 1 will be denoted as CSW40, CSW65 and CSW80, according to their area reduction. The rods were not rotating inside the machine during the process therefore the swaging had four-fold symmetry and this resulted in deformation instabilities ("wings") that formed in a part of rod with 80% of area reduction.

Second set of samples was produced from rods with diameter 15 mm in COMTES FHT a.s., Plzeň. They were cold-swaged to diameters 8 mm, 7 mm and 6.3 mm while reaching area reductions of 72% – CSW72, 78% – CSW78 and 82% – CSW82), respectively. These rods will be denoted as series 2. Rotation of sample inside the swaging machine was used to ensure the stability of the process as well to avoid the four-fold symmetry of the resulting microstructure.

3.3.4 Recrystallization annealing

For recrystallization annealing, the samples were machined and cut from all three conditions prepared in UJP: CSW40, CSW65, CSW80, and from two conditions prepared in COMTES FHT: CSW72 and CSW82. The samples had the diameter of 5 mm (4.1 mm for CSW80) and the length of 9 mm. The annealing was performed at COMTES FHT in quenching dilatometer Linseis L78 RITA in He atmosphere at conditions (temperatures/times) shown in Table 3.3. The heating rate was 10 K/s (600 K/min). Samples from the series 1 of cold swaging (CSW40, CSW65 and CSW80) were helium quenched after annealing and the samples from the series 2 of cold swaging (CSW72 and CSW82) were cooled by rate 2 K/s (120 K/min) to simulate cooling on air.

Table 3.3: Temperatures/times of annealing in dilatometer.

Cold swaging	Thermal processing		
CSW40	800 °C/15 min	1000 °C/15 min	1200 °C/15 min
CSW65	–	1000 °C/15 min	1200 °C/15 min
	1200 °C/2 min + 800 °C/15 min		
CSW80	800 °C/15 min	1000 °C/15 min	1200 °C/15 min
	1200 °C/2 min + 800 °C/15 min		
CSW72	–	1100 °C/2 min	1200 °C/2 min
	1000 °C/5 min	1100 °C/5 min	1200 °C/5 min
	1000 °C/15 min	1100 °C/15 min	–
CSW82	1000 °C/5 min	–	1200 °C/5 min

3.4 New alloys fabrication

Six alloys with optimized Nb and Ta content were designed on the basis of the literature review presented in section 1.4 and in the Attachment 1 of this thesis. Their nominal composition is shown in Table 3.4. Four alloys contain the original content of Ta and differ in Nb content that starts at the original value of 35% (for comparison) and drops down to 26%. Two alloys do not contain Ta and the content of Nb is 35% and 29%. The content of 7% Zr and 0.7% O is maintained the same for all alloys. Alloy labeling will be based on the Nb, Ta and Zr content such that the contents in percent will be added after the TNTZO, separated by dashes. For example, the original alloy TNTZO will be in the context of other new alloys (section 4.7) designated as TNTZO-35-6-7 and alloys without Ta will have only two numbers after the TNZO designation (only for Nb and Zr, e.g. TNZO-35-7).

Table 3.4: Nominal composition of newly developed alloys

Alloy	Ti	Nb (%)	Ta (%)	Zr (%)	O (%)
TNTZO-35-6-7	Bal.	35	6	7	0.7
TNTZO-32-6-7	Bal.	32	6	7	0.7
TNTZO-29-6-7	Bal.	29	6	7	0.7
TNTZO-26-6-7	Bal.	26	6	7	0.7
TNZO-35-7	Bal.	35	0	7	0.7
TNZO-29-7	Bal.	29	0	7	0.7

Alloys were produced at UJP Praha a.s. by a method verified already during the development of the original TNTZO alloy [41]. Powders of elementary metals and TiO_2 for oxygen addition were precisely weighted and mixed and subsequently remelted 6 times to ensure homogeneous mixing of all elements in the ingots. The TiO_2 was added after the first melting. Electric arc with tungsten electrode doped by ThO_2 (for better performance of the arc) was used for melting process under low pressure of He atmosphere. Casting weight was controlled after each melting and weight variations between the first and the last melting (and also between each melting) did not exceed 0.5%. Therefore, the highest possible electrode burn-off contamination by tungsten does not exceed 0.5% and contamination by ThO_2 is less than 0.02%. During production of TNTZO-35-7 alloy, the electrode

did stick to the casting and had to be ground away. As a consequence, precise chemical composition (especially due to W and ThO_2 contamination) was not guaranteed and other casting was produced with the same composition. This possibly deteriorated casting will be denoted as TNZO-35-7-a.

After last remelting, the boat-like shaped castings were heated to 1000 °C/6 h in vacuum (and furnace cooled) with the aim to homogenize the chemical composition. These conditions differ from the material prepared in [42], where 1200 °C/2 h was used for homogenization. Before machining, the ingots were solution treated at 820 °C/10 min on air and water quenched to dissolve α phase possibly formed during the slow cooling after homogenization annealing. The example of such ingot is shown in Fig. 3.3.

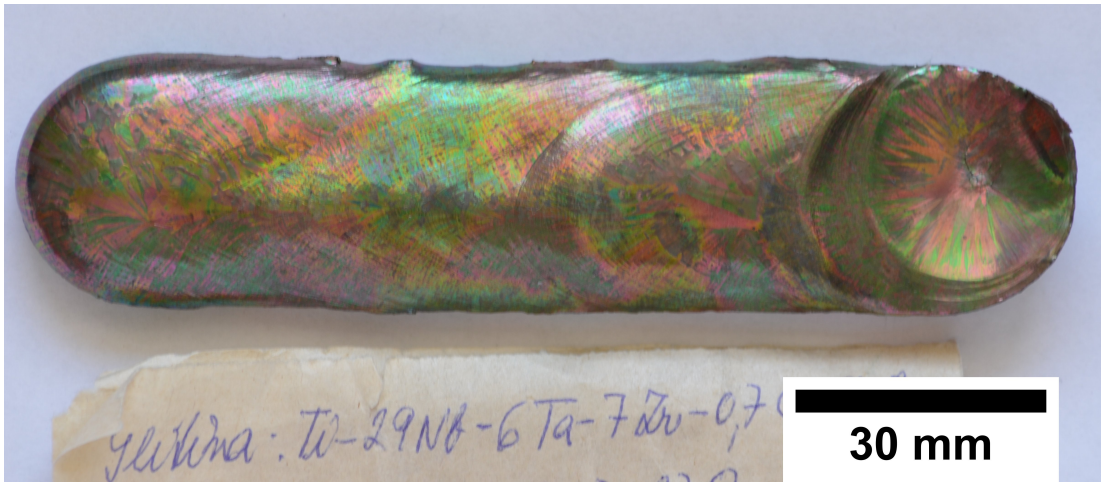

Figure 3.3: Ingot of TNTZO-29-6-7 after ST at 820 °C/10 min + WQ.

4. Sample prepatation and characterization techniques

4.1 Sample preparation

Sample preparation for scanning electron microscopy (SEM), electron back-scatter diffraction (EBSD) and Vickers microhardness measurement (HV) is very similar.

4.1.1 SEM + EBSD + HV

For these three methods, a flat surface is needed for obtaining accurate results. All samples were cut from prepared conditions or alloys by an automatic precision saw Struers Accutom-50 with Struers diamond wafering blade. The feed rate used was 0.005-0.020 mm/s and rotation speed was 3000 rpm.

The cut slices were subsequently mounted in PolyFast mounting resin or attached to aluminum holders. Their surface was ground and polished on Struers Tegramin-25 automated polisher with SiC papers using gradually increasing grits of 120, 220, 320, 500, 800, 1200, 2400 and 4000.

The next preparation step was the vibratory polishing using Buehler VibroMet 2. Samples were polished in three steps using two alumina suspensions for the first two steps (0.3 µm and 0.05 µm) for 7-8 hours on each suspension. Final polishing was done on Colloidal Silica suspension (0.02 µm - 0.05 µm) for 4 hours. The samples and sample holders had to be cleaned carefully between each polishing step to avoid contamination from the previous suspension. Also the final polishing duration was shortened from initial 7-8 hours to optimal 4 hours. This prevents excessive contamination of the surface by Silica particles.

If the contamination by the silica particles was too high for observations in SEM, the surface was cleaned using Leica EM RES102 argon ion polisher for 30 min with voltage 5 kV, current 2 mA and incident angle 6°.

4.1.2 Tensile testing

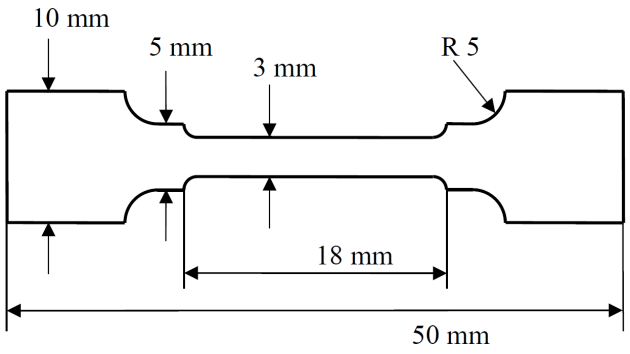

Figure 4.1: Shape and dimensions of tensile samples [42].

Samples for tensile testing had circular cross-section and their shape with corresponding dimensions is shown in Fig. 4.1. The gauge length of specimens was 15 mm and diameter was 3 mm, they were thus compliant with standard A5.

Circular rods were prepared by electric discharge cutting and turned into the final shape at the company Beznoska a.s., Kladno.

4.1.3 Fatigue testing

Typical hourglass-shaped samples with the diameter of 3 mm in the narrowest part of the sample were used for the testing as shown in Fig. 4.2.

The fatigue resistance samples were prepared at company Beznoska a.s, by electric discharge cutting and turning as the tensile samples.

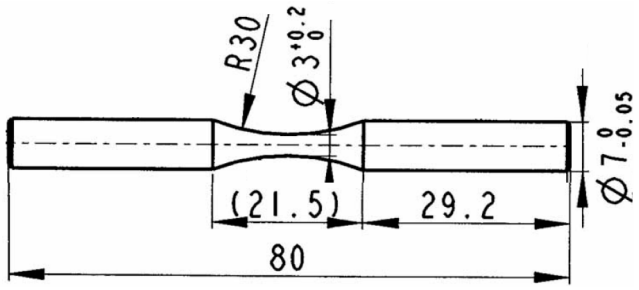

Figure 4.2: Shape and dimensions of fatigue samples.

4.2 Experimental techniques

4.2.1 Scanning electron microscopy (SEM)

All studied conditions and alloys were analyzed primarily by scanning electron microscope. SEM uses voltages of 10 kV – 30 kV and needs very well polished surface for microstructure observations. The image in SEM is created by scanning the surface and of detection signals wchich are formed by interaction of the electron beam with the specimen.

The scheme of such microscope is in Fig. 4.3. The electrons are emitted from electron gun. Field emission gun (FEG) produces coherent and bright electron beam that is suitable microstructure observations.

After emission, the electrons are collimated by a pair of electromagnetic condenser lenses and aperture that sets the resolution and brightness. The other parts of SEM include the deflection coils that provide the scanning of the surface and an objective lens for electron beam focussing on the specimen surface.

After an electron reaches the sample surface, a number of signals is formed which are detected by a series of detectors. Depending on their type and nature, the signals can originate from different depths and have a different resolution. Fig. 4.4 shows a schematic figure of these signals. The main signals used in SEM imaging are secondary electrons (SE), back-scattered electrons (BSEs) and characteristic x-rays.

Secondary electrons (SE) have the energy much lower than the primary electrons. They were originally part of electron gas of the metal but primary electrons

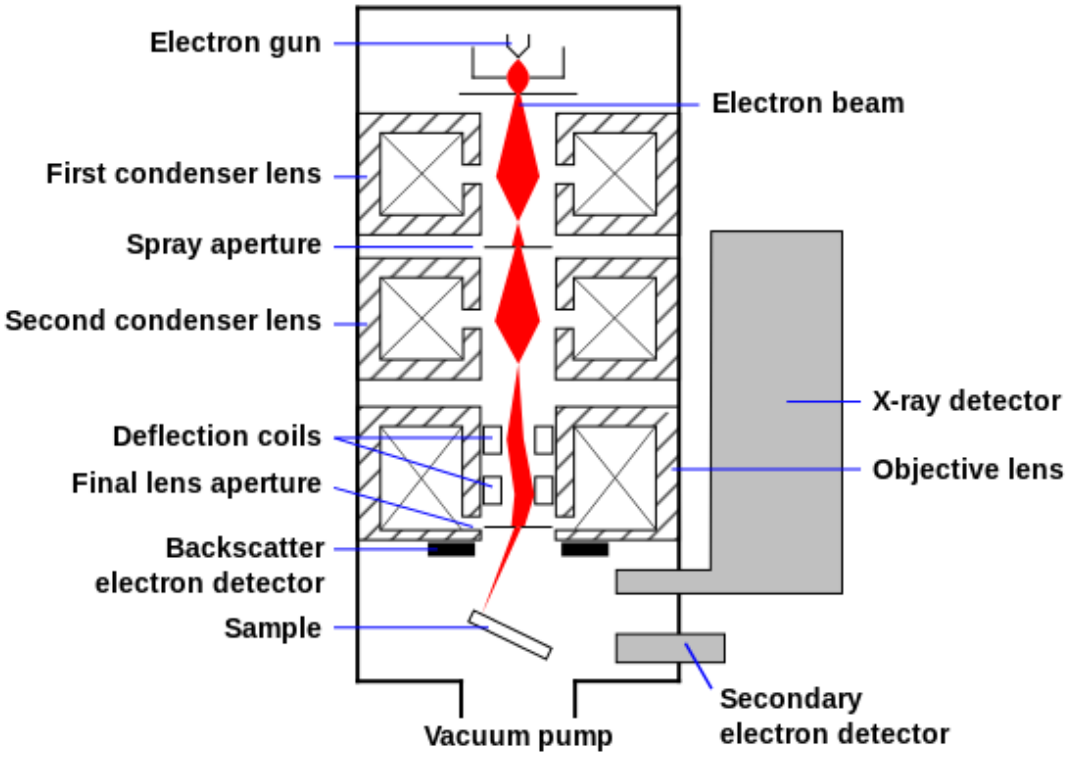

Figure 4.3: Scheme of a scanning electron microscope [66].

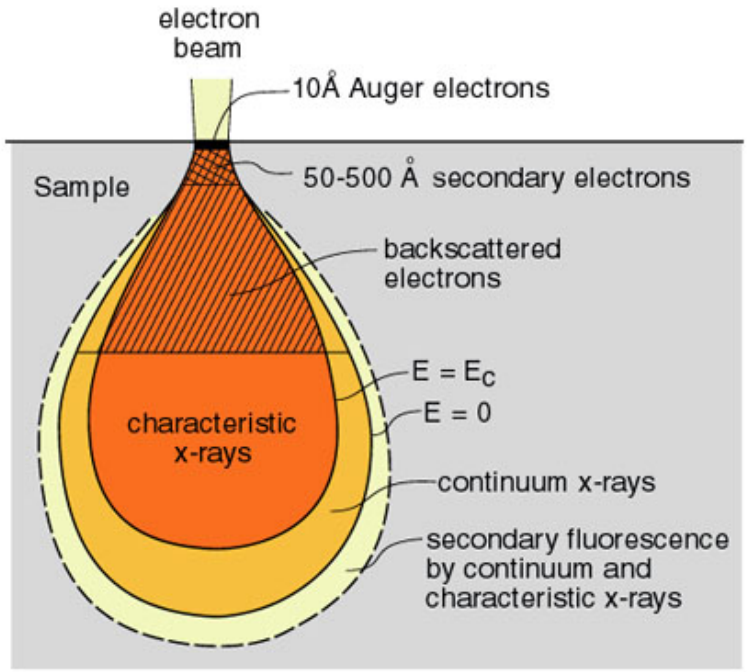

Figure 4.4: Signals excited by an alectron reaching a sample surface [67].

have transferred a part of their energy so that they could leave the sample and be detected by a SE scintillator detector. SE carry mainly information about the surface topography - because of their low energy (tens of eV), they can only escape from a thin layer of 5 nm – 50 nm under the surface (depending mainly on the material of the sample and the primery beam energy).

Back-scattered electrons (BSEs) are originally primary electrons that were scattered by a crystal back into chamber of the microscope either elastically or with only minor energy loss. Thus they have energy nearly the same as the primary beam electrons. The BSEs possess a qualitative information about chemical composition (heavier elements scatter more than lighter elements) and also about crystallite/grain arrangement. The latter is due to a fact that different grains scatter the incident electrons differently, some orientations allow the electrons to channel through many layers of atoms whereas some of them do not. Because of the nature of the channeling through planes of atoms, this signal is called "channeling contrast" whereas the signal emerging from chemical composition is called "Z-contrast". BSEs originate from a volume up to 1 µm below the surface (again, this depth is dependent on a sample material). The diffraction of BSEs can be also detected, more about this signal is in section 4.2.2.

Characteristic X-rays are formed by a recombination of electron shells after excitation by primary electrons. By their detection, we can get quantitative information about local chemical composition. X-rays can be analyzed either on the basis of their wavelength or energy. The latter is used in this thesis and the method is therefore called energy dispersive x-ray spectroscopy (EDX).

For all observations in this thesis, the scanning electron microscope FEI Quanta 200F equipped with FEG, SE detector, BSE detector and EDX detector and also EBSD camera was used operating mainly with accelerating voltage of 10 kV for BSE observations and 20 kV - 30 kV, when excitation of characteristic x-rays of Ta was needed for EDX. Sample preparation was described in previous section 4.1.1.

4.2.2 Electron back-scatter diffraction (EBSD)

As described above, the BSEs can diffract under special circumstances. This diffraction is called simply electron back-scatter diffraction (EBSD) and possesses qualitative information about local crystallographic orientation. When the electrons are scattered inelastically inside the crystal, continuous distribution of their energies is formed. These electrons can diffract on crystallographic planes in Bragg angle according to their energy. Each system of planes creates electron–filled cone where the surface electrons have the highest energy (energy of the incident beam). This cone forms lighter Kikuchi band upon reaching the fluorescent screen of the detector. Kikuchi bands are therefore planar intersections with cones.

By indexing these bands (with help of Hough algorithm for easier detection of lines), we can get orientations of crystal in individual points of the sample where the EBSD signal is acquired. If the crystal orientation is clear from the indexing, high confidence index (CI) is obtained for the measured point. However, if two or more non-equivalent orientations share a similar Kikuchi pattern, lower confidence index is obtained and the most probable orientation is chosen. Another measure of indexing success is image quality (IQ), that is a measure of detected Kikuchi pattern quality. If poor IQ is obtained by measured point, then this point's orientation is probably not measured correctly and with struggle to index the pattern, the CI is also low. Depending on the size of the EBSD scan and step size used, one measurement can take from 0.5 h up to a day.

Surface for the EBSD measurements needs to be very flat with a minimum of flaws that could destroy the coherence of diffracting electrons and cause low IQ (and CI). In the beginning of the work on this thesis, accelerating voltage of 10 kV was used during EBSD measurements but the IQs and CIs were too low. The voltage was thus optimized to 20 kV and data started showing much better both IQ and CI.

Usually, the data obtained by an EBSD scan are shown in the so-called inverse pole figure (IPF) map. This map shows different orientations as different colors, based on the orientation triangle with three principal orientations ([100], [110] and [111]) in the corners for cubic materials. For characterization of texture in material, either pole figure (PF) as two-dimensional projections of orientations or inverse pole figure showing intensity of all symmetrically equivalent direstions, can be used.

There are some other methods of visualizing and processing the measured data. If we want to characterize the local deformation present in the material, the kernel average misorientation (KAM) is very useful choice. KAM is determined for each data point as the mean misorientation of all points within the maximum distance around each point (note that hexagonal grid was used for measurements of EBSD). In this thesis, triple step size was used as the kernel diameter and points separated by GBs (points with misorientation higher than 5° from reference point) are excluded from each kernel.

If we want to measure the overall deformation present in each grain, grain orientation spread (GOS) can be computed. GOS is a characteristic angle for every grain and is calculated as an average misorientation between all measured points in single grain and their mean orientation. GOS is very useful for determining the recrystallized fraction in deformed and annealed material. Usually GOS value under 1° signifies recrystallized (or non-deformed) grain.

4.2.3 Microhardness measurements

For a basic characterization of mechanical properties, the microhardness is a fast and simple method that needs the spacimen surface to be prepared in a same way as for the SEM and EBSD measurements; sometimes even less flat surface is sufficient (e.g. after only the first step of vibratory polishing). In our case, Vickers microhardness was used. This method utilizes a precisely manufactured diamond pyramid indenter that is pressed into measured material under a given load F for a defined time. By measuring the diameter d of a diagonal of the indent, Vickers microhardness can be computed using a simple formula [68]:

$$HV = 2 \sin \frac{136^\circ}{2} \times \frac{F}{d^2}, \tag{4.1}$$

where F is in kilogramforce and d is in millimeters. Qness Q10A automatic hardness tester was used to measure the microhardness employing a load of 0.5 kgf and duration of each indentation 10 s.

4.2.4 Tensile testing

Microhardness is a useful mechanical property. However it does not reflect all aspects of the material behavior under loading, especially, when the grain size

is larger than individual indent diameter, the GB strengthening is completely neglected by microhardness measurements. For this purpose, the tensile test gives much more information. Generally, precisely machined sample is gripped to some holder and deformed by a given velocity v. If we measure the force F needed to deform the sample, complete stress-strain curve can be obtained from following equations:

$$\dot{\varepsilon} = \frac{v}{l_0}, \tag{4.2}$$

$$\varepsilon_{ENG} = \frac{l}{l_0}, \tag{4.3}$$

$$\sigma_{ENG} = \frac{F}{\frac{\pi d^2}{4}}, \tag{4.4}$$

where σ_{ENG} denotes the engineering stress, ε_{ENG} denotes the engineering strain (resulting stress – strain curve is also called an engineering curve) and ε is the strain rate. The gauge length of the sample is denoted l_0 and diameter d.

For better characterization of plastic deformation during the tensile test, the so-called true stress – true strain curve is evaluated. These true values mean that instantaneous load is applied on instantaneous cross-sectional area . Following equations are used to get the true stress σ and true strain ε from their engineering counterparts:

$$\sigma = \sigma_{ENG} \times (1 + \varepsilon_{ENG}) \tag{4.5}$$

$$\varepsilon = \ln \times (1 + \varepsilon_{ENG}) \tag{4.6}$$

For even better characterization of plastic part of the stress-strain curve, the elastic part can be subtracted resulting in the plastic tensile curve and we can get easily total plastic true strain.

For the tensile testing, deformation machine Instron 5882 was used with a maximum capacity of 100 kN and the strain rate of 10^{-4} s^{-1} was set for each measurement.

4.2.5 Fatigue testing

When the material is repeatedly loaded with stress that does not exceed the YS, it can still fail after a certain number of cycles depending on the applied stress amplitude. For characterization of the so-called fatigue resistance, several samples need to be measured, while changing the applied stress, in order to obtain the Woehler/S-N plot with stress amplitude on y-axis and number of cycles in logarithmic scale on x-axis. For our purpose, the R = -1 tension-compression method was used. The fatigue limit is determined as the maximum stress amplitude at which the material could sustain 10 million cycles.

Fatigue testing was conducted at companies: SVÚM a.s., Čelákovice, COMTES FHT a.s., Plzeň and Beznoska a.s., Kladno.

4.2.6 Acoustic and ultrasound resonance spectro-scopy

The acoustic resonance spectroscopy (ARS) and ultrasound resonance spectroscopy (RUS) were used for Young's modulus determination of the newly developed alloys.

Let us first describe the ARS method. When we an object undergoes some kind of mechanical excitation, it excites a whole spectrum of frequencies (maximal excited frequency depends on the object and excitator stiffness). However, only those frequencies that are compatible with the shape of this object are retained. These are called eigenfrequencies and for sufficiently simple objects (rod, brick) the elastic properties can be computed from the eigenfrequencies, dimensions and weight of this object. IMCE RFDA Professional system was used for YM measurement which consists of an automatic excitation unit and microphone with the frequency range of 10 Hz — 10 kHz, both fully controlled by a PC. The YM is automatically computed from sample dimensions and weight and measured frequency by a standard equation [69]. Samples used for measurement were in the form of rods with the diameter of 8 mm and the length of 90 mm.

RUS method is based on similar physical behavior of samples as the ARS. The main difference follows from the name of this method: ultrasound frequencies are used for the determination of Young's modulus whereas for ARS, the frequencies lie in audible region. In this case the excitation is provided by a short laser pulse and also the detection is laser-based. The samples are in shape of small bricks with dimensions 2×3×4 mm. After excitation, the sample eigenmodes are recorded with a laser and fitted by a computer model allowing to obtain the Young's modulus. YM measurements by RUS were performed at the Institute of Thermomechanics at The Czech Academy of Sciences on PolyTec MicroSystem Analyzer.

The ARS technique is suitable for materials that have larger grain size (provides larger statistics) but relatively large samples must be used. On the other hand, in RUS smaller smaples are usually used. As a consequence, the measurements can be affected by an insufficient number of grains in the material.

5. Results and discussion - thermomechanical processing of TNTZO alloy

5.1 Previous work and characterization of cast ingot

5.1.1 Previous work

Characterization of the cast ingot of TNTZO in as-cast condition and after aging at 400 °C and 500 °C by SEM, microhardness and tensile testing was done already in bachelor thesis of the author [63]. Also, first attempt of die-forging into a shape of hip stem semi-product was performed and experimentaly characterized.

SEM image of the microstructure present in cast material is shown in Fig. 5.1a. It was found that the casting produces material with very large grains (0.5 mm - 2 mm) and porosity (20 µm - 20 µm pores) that is concentrated more in the central part of the ingot cross section. The edge contains significantly lower amount of pores. This indicates that the porosity is formed with the help of the well-known shrinkage effect described in [70]. This also indicates that the temperature range of coexistence of solid and liquid phase of this alloy is quite wide. Otherwise, the central cavity would be present instead of pores. Another defect found in the cast material was chemical inhomogeneity in the form of dendrites. These dendrites were again, located more in the center rather than on the edge of the ingot.

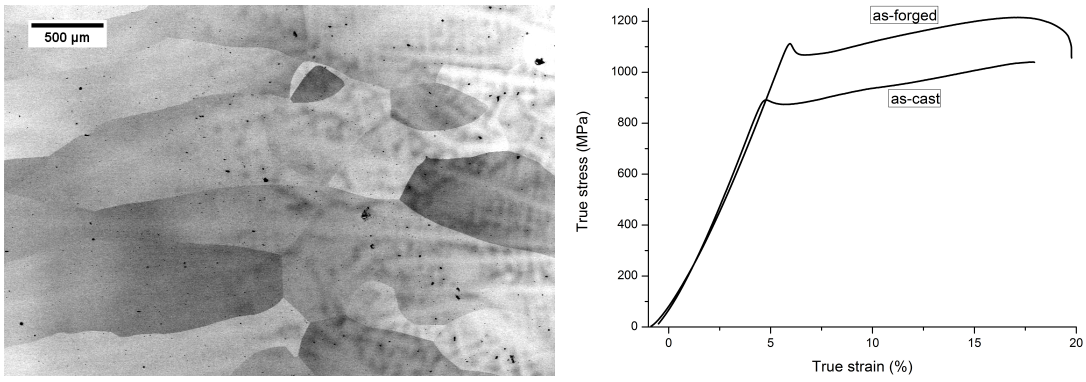

(a) (b)

Figure 5.1: a) SEM image of the structure of the cast TNTZO alloy, b) tensile curves of the cast and forged material [64].

The investigation of the aged samples revealed high β stability of this alloy as the α phase precipitation was observed only on a few GBs after long aging at 500 °C/16 h. The forging exhibited a deformed grain structure but the grain refinement occurred only near GBs. On the other hand, the porosity was removed by this procedure. In Fig. 5.1b, the tensile curves of the as-cast and forged

material are shown. The YS of the cast alloy is 900 MPa but forging causes significant enhancement of strength to 1100 MPa [41, 64].

5.1.2 EBSD of the as-cast ingot

In order to further extend the knowledge about the cast ingot, the so-called "combo" EBSD scan was performed by measuring multiple EBSD scans next to each other and then merging these sub-scans into one large scan and cleaning the resulting data from artefacts. The information about the grain orientations is shown as an inverse pole figure (IPF) map in Fig. 5.2 together with pole figure (PF) of [100] orientations. The high angle GBs (misorientation>15°) are denoted by black lines (this convention will be used in whole thesis) and low-angle GBs are white (this color will be chosen each time to enhance the contrast with respect to IPF map colors).

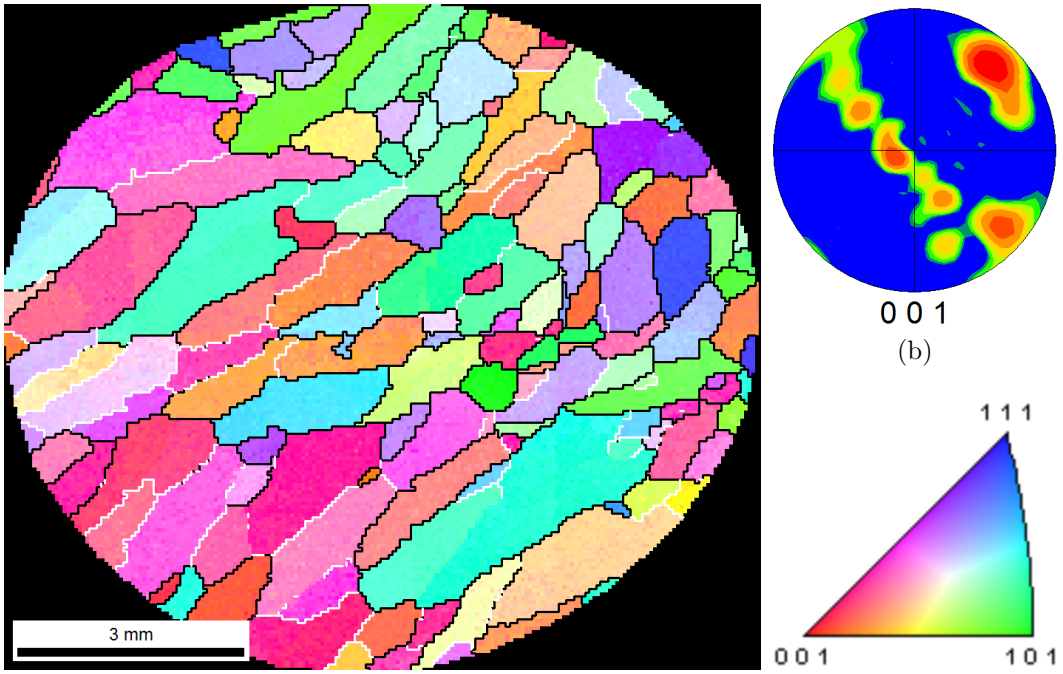

(a) (b) (c)

Figure 5.2: a) IPF map of the as-cast sample. b) PF is from the lower left half of the map, c) orientation triangle for bcc structure.

This sample with the diameter of 9 mm was taken from the ingot between center and the edge. The center of the ingot is in the top right direction and the edge in the opposite direction. Closer to the edge, columnar zone of the ingot is easily recognized. These columnar grains grow into the center in [100] direction, that is seen from the [100] PF in the inset that was computed from lower left part of the map. This growth direction is typical for all cubic materials [70]. Closer to the center, the equiaxed zone emerges that contains grains that are oriented more randomly and also are smaller than the columnar grains. Note that the equiaxed zone intersects with the part of sample, where higher porosity and inhomogenieties were found. These findings can be used when designing the final production procedure of a material.

5.1.3 Fatigue testing of the as-cast ingot

In Fig. 5.3, the S-N plot of the cast ingot is shown. The red line indicates fatigue limit of Ti-6Al-4V. The fatigue resistance after casting is very low. Five samples were measured with stress amplitudes down to 350 MPa and all of them failed before reaching 100 000 cycles while 10 million cycles are is usually used for the determination of the fatigue limit. The testing was therefore aborted. Possible causes of low fatigue performance are the porosity from casting and very large grain size that is comparable to the sample gauge size, therefore no GB strengthening occurs. Further work will therefore be aimed to closing the pores and refining the grain structure.

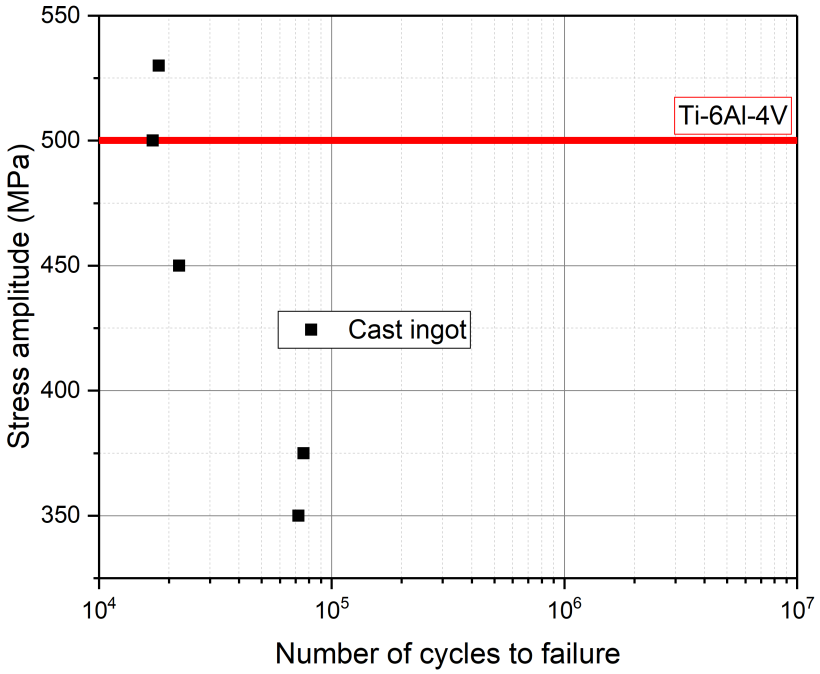

Figure 5.3: S-N plot of cast ingot and forged stem semi-product.

5.2 Hot compression testing

In order to characterize the behavior of the TNTZO alloy during forming, hot compression tests were performed. The single-hit test results will be shown first.

5.2.1 High temperature mechanical properties (single-hit deformation experiments)

Flow curves from compression tests at elevated temperatures are shown in Fig. 5.4. It should be noted that curves recorded at high strain rate of $\dot{\varepsilon} = 1$ s^{-1} contained artifacts and massive smoothing procedure was employed with care to preserve their fine wavy structure. The noise was recorded also on the curves for lower strain rate of $\dot{\varepsilon} = 0.01$ s^{-1}, but it was so extensive that possible fine structure could not be preserved or observed.

As expected, lower temperatures and higher strain rates lead to higher compressive strength. The samples deformed at the temperature of 800 °C and 900 °C with $\dot{\varepsilon} = 0.01$ s^{-1} exhibit either the sharp yield point similarly to the tensile flow curves performed at room temperature or this undulation is caused by dynamic recovery/recrystallization during straining. Some undulation can be observed also on curves from 1000 °C and 1100 °C with $\dot{\varepsilon} = 1$ s^{-1}, but in much smaller extent. The wavy structure of the curves from $\dot{\varepsilon} = 1$ s^{-1} could be a sign of dynamic recovery of dislocations.

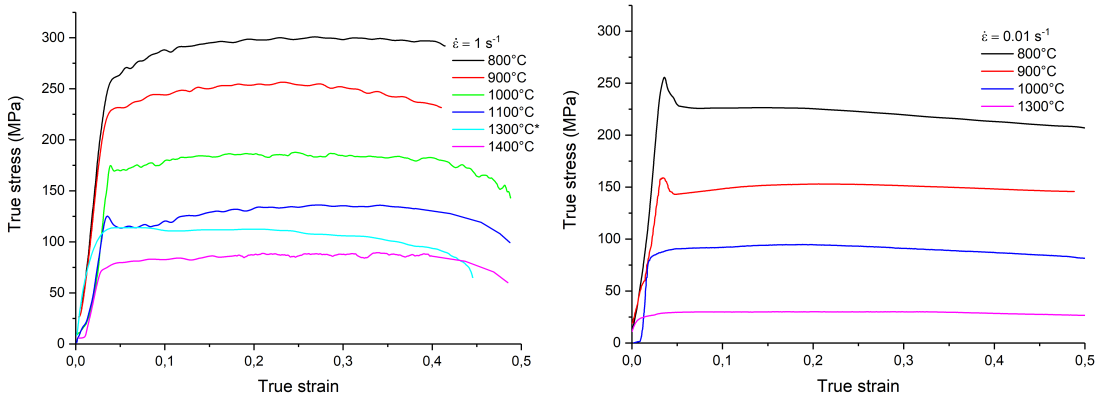

(a) (b)

Figure 5.4: Single-hit compression flow curves for a) $\dot{\varepsilon} = 1$ s^{-1} and b) $\dot{\varepsilon} = 0.01$ s^{-1}. The strain rate of sample deformed at 1300 °C in the left graph was around 2.5 s^{-1} due to the fault of testing machine (not used for compressive strength determination).

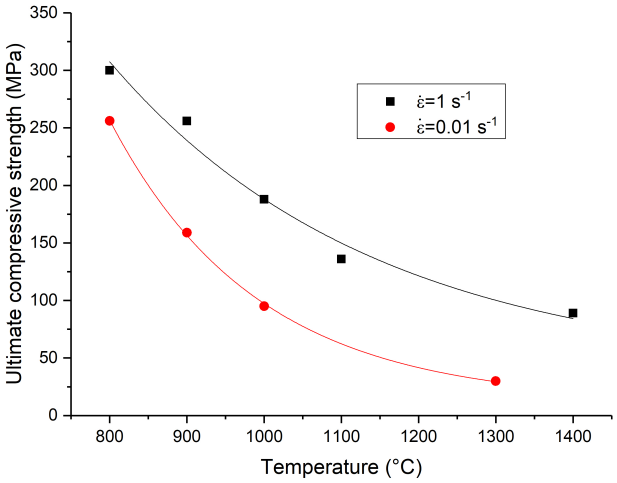

Figure 5.5: The temperature dependence of the UCS for the strain rates used.

Ultimate compressive strength (UCS) was determined from each flow curve. The temperature dependence of UCS is shown in Fig. 5.5 for both strain rates used. Fitted exponential is steeper for $\dot{\varepsilon} = 0.01$ s^{-1} than for $\dot{\varepsilon} = 1$ s^{-1}. The main reason of this difference is the sharp yield point (or recovery induced undulation) on the curve of sample deformed at 800 °C. The strength of studied material at $\dot{\varepsilon} = 1$ s^{-1} exceeds 170 MPa at 1000 °C and decreases below 100 MPa only

at 1400 °C. For comparison, the strength of Ti-6Al-4V deformed at 1000 °C and $\dot{\varepsilon} = 1\ s^{-1}$ drops below 50 MPa [71]. On the other hand, commercial stainless steel AISI 304 has similar values as TNTZO [72].

5.2.2 SEM observations after single hit experiments

SEM observations revealed that porosity present in the cast condition was not completely removed by high temperature deformation. Gleeble processing deformed the area around the pores and closed some of them. The deformed zones can be observed in channeling contrast of back-scattered electrons in Fig. 5.6a (T=1100 °C; $\dot{\varepsilon} = 1\ s^{-1}$) as lighter area near both pores.

Some new cracks of the size of tens of micrometers were also observed, located at the grain boundaries, especially in triple points, see Fig. 5.6b (T = 1300 °C; $\dot{\varepsilon} = 1\ s^{-1}$). These cracks reflect quite low formability of this alloy even at these high temperatures. The cracks were not present in all deformed samples but correlation with temperature or strain rate is rather inconclusive.

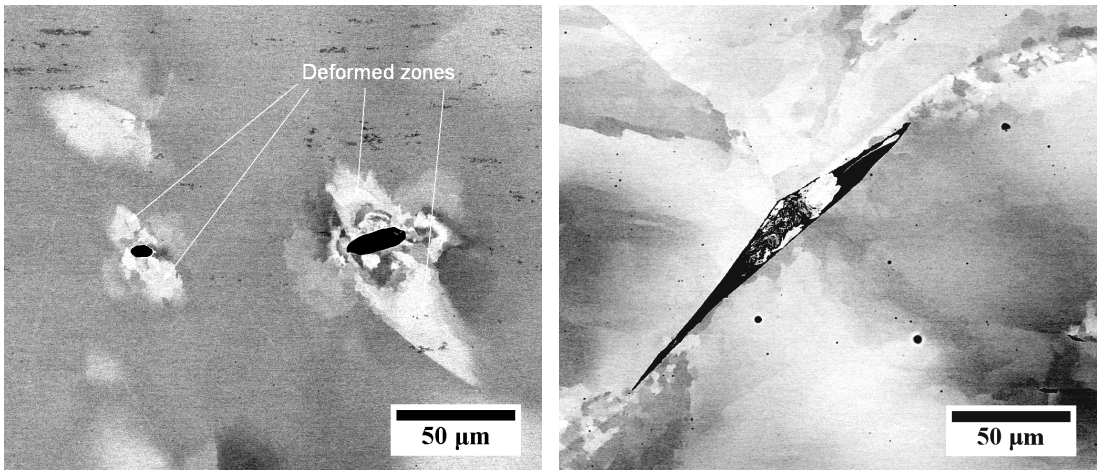

(a) (b)

Figure 5.6: a) Pores with deformed surrounding area (T=1100 °C; $\dot{\varepsilon} = 1\ s^{-1}$), b) Crack on grain boundary (T=1300 °C; $\dot{\varepsilon} = 1\ s^{-1}$).

5.2.3 EBSD measurements after single hit experiments

EBSD measurements were performed to analyze the grain refinement by dynamic recrystallization and the degree and the distribution of deformation imposed to individual samples. The area of 1300 µm × 1800 µm and the step size of 4 µm were employed. Significant grain refinement was not observed in any of the samples after single-hit deformation. Possible grain size variations observable in images shown below are caused only by the selection of the EBSD scan area, thus are not representative.

For the purpose of studying the deformation present in the structure, kernel average misorientation (KAM) was determined for each data point. Example of IPF map for sample deformed at T=1300 °C and $\dot{\varepsilon} = 1\ s^{-1}$ is shown in Fig. 5.7a,

the corresponding KAM map is displayed together with the color code of respective misorientations in Figs. 5.7b and 5.7c. It is clearly seen that the deformation (higher KAM value) is concentrated near grain boundaries, especially near triple points. This concentration of deformation was present in most samples deformed at the strain rate of $\dot{\varepsilon} = 1\ s^{-1}$ (images for other deformation temperatures are not shown here due to their similarity) and is typical in β-Ti deformed at high temperatures [56]. Changes of crystal orientation inside the grains are not as significant as on the GBs and manifesting only small plastic deformation in grains.

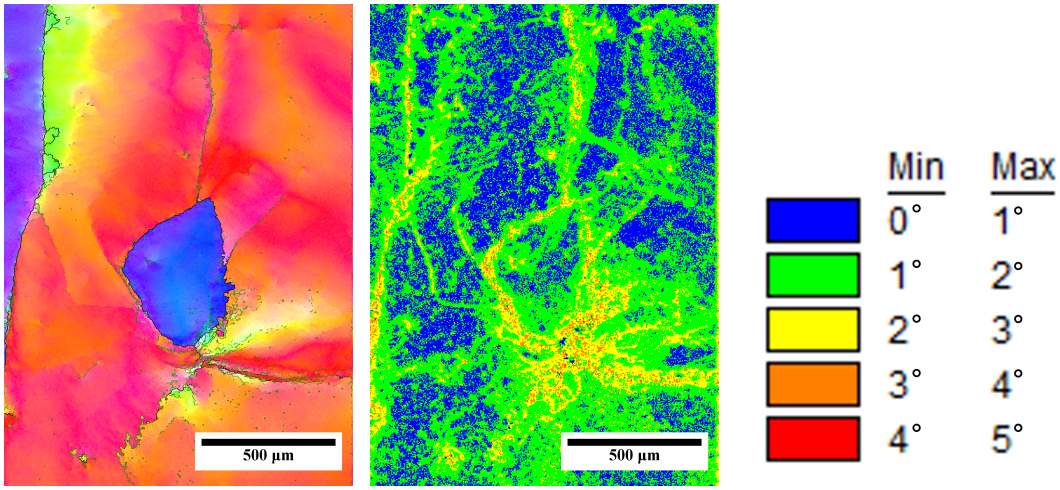

(a) (b) (c)

Figure 5.7: Sample deformed at T=1300 C and $\dot{\varepsilon} = 1\ s^{-1}$. a) IPF map, b) KAM map, c) KAM color code.

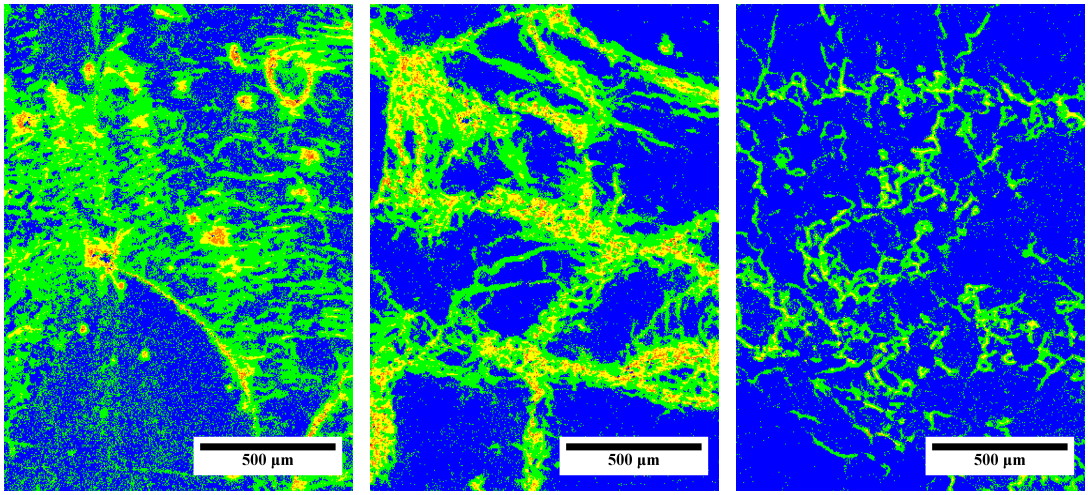

(a) (b) (c)

Figure 5.8: KAM maps of samples deformed at $\dot{\varepsilon} = 0.01\ s^{-1}$ and (a) T=800 °C, (b) T=1000 °C and (c) T=1300 °C. For the orientation color code, see Fig. 5.7c.

The KAM maps of samples deformed at the lower strain rate of $\dot{\varepsilon} = 0.01\ s^{-1}$ are shown in Fig. 5.8. The KAM distribution at this lower strain rate strongly depends strongly on the temperature of deformation. Fig. 5.8a shows that at

lowest temperature of 800 °C the KAM values are distributed very homogeneously (homogenous distribution of green-colored areas), while at higher temperature of 1000 °C (Fig. 4.2.5 b)), the deformation is concentrated at grain boundaries that are characteristic by higher KAM value (green and yellow colors). In addition, several spots of enhanced deformation (higher KAM value) can be seen in Fig. 5.8a. These spots indicate the presence of pores around which the material is highly deformed as observed also in BSE image; cf. Fig. 5.6a.

The highest deformation temperature of 1300 °C leads to lowest amount of deformation imposed to the material; see Fig. 5.7c. The blue color denoting low local misorientation is present almost in the whole image with some tiny areas of green, indicating slightly deformed structure. The cause for this behavior is apparently the dynamic recovery of dislocations formed during deformation that is more pronounced in higher deformation temperatures (1300 °C).

The dynamic recovery effects at $\dot{\varepsilon} = 0.01$ s^{-1} were not captured by the compressive curves, probably because these effects are too quick in comparison with time resolution during the compressive tests at $\dot{\varepsilon} = 0.01$ s^{-1}. On the other hand, time resolution during the tests at strain rate 1 s^{-1} was much higher and the wavy curves were measured.

Fig. 5.9 shows, that while deforming the TNTZO alloy below approx. 1000 °C (at 900 °C and 800 °C) at high strain rate of 1 s^{-1}, different behavior of microstructure appears during deformation 1000 °C; cf. Fig. 5.7a), where the deformation was concentrated at GBs.

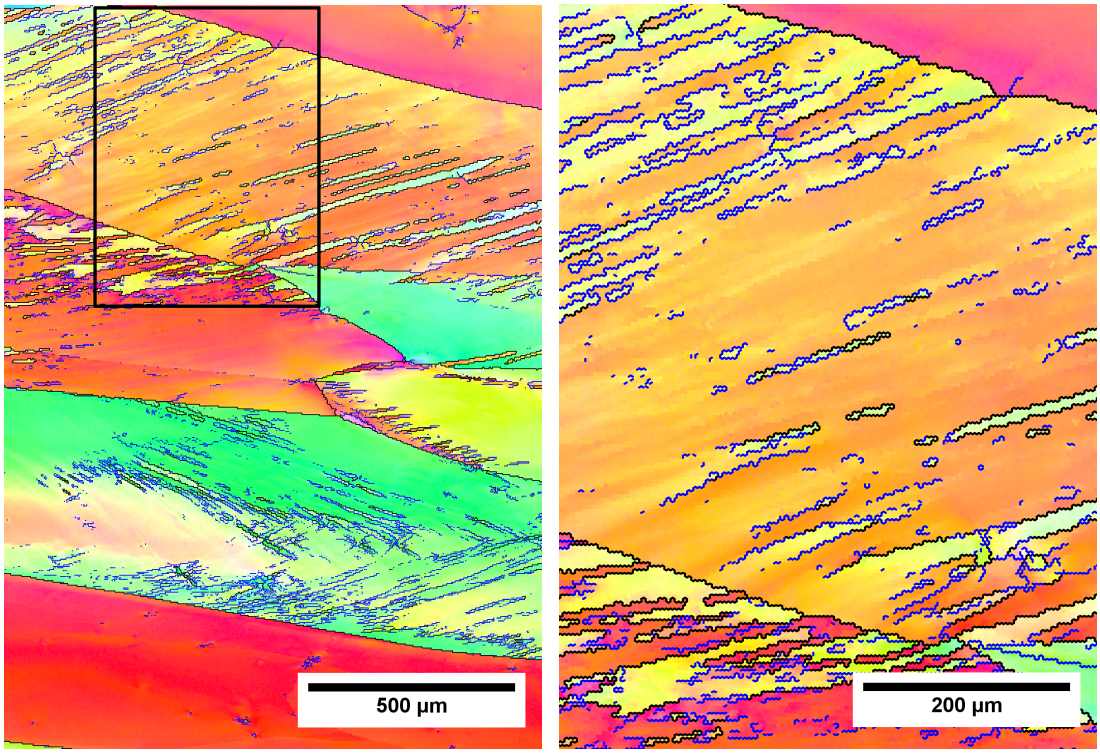

(a) (b)

Figure 5.9: IPF map of sample deformed at 800 °C and $\dot{\varepsilon} = 1$ s^{-1} a) overview, b) detail of deformation bands from area highlighted at a).

Fig. 5.9a shows IPF map of sample deformed at 800 °C and $\dot{\varepsilon} = 1$ s^{-1}. The

band-like structures were not observed after deformation at temperatures over 900 °C. They resemble twins, however, twinned material differs from these structures. As seen in Fig. 5.9b, the high-angle GBs are continuously transforming into low-angle GBs, that are formed by individual dislocations. The presence of dislocations confirms the fact, that these bands are not twins. Since the bands are actually formed by dislocations (either walls or more complex GBs) and exhibit uniform orientation, it may be concluded, that only few slip systems with highest Schmidt factor are active. In the lower part of Fig. 5.9a, the green-colored grain contains actually two types/directions of the slip bands (probably both active slip systems have similar Schmidt factor). Because of high number of active slip systems in bcc structure, these materials have generally wavy and ill-defined slip lines after high-temperature deformation [53]. This is not the case of the shown structure. Apparently the combination of T =800 °C and $\dot{\varepsilon} = 1$ s^{-1}, together with high melting temperature of this alloy, cause the material to deform by mechanisms operating low temperatures. This is confirmed by low number of active slip systems.

5.2.4 Double-hit deformation experiments

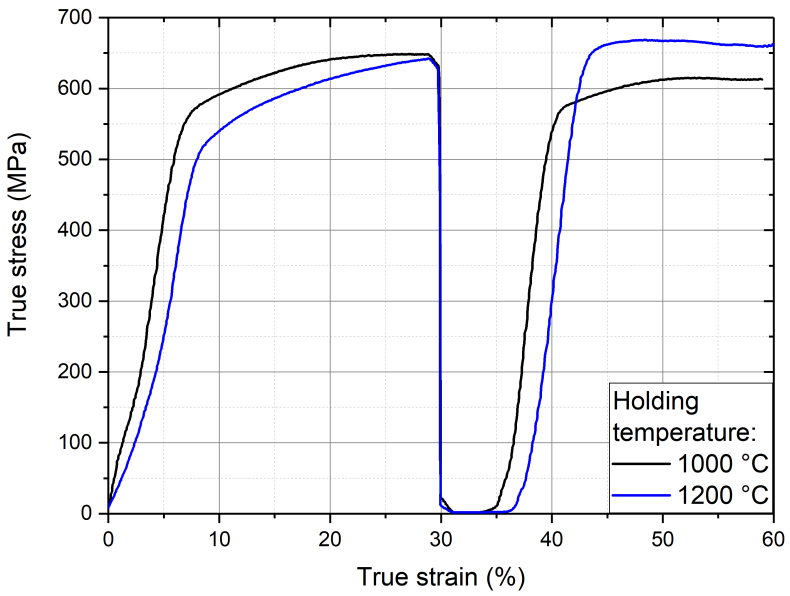

Figure 5.10: Double hit experiments with deformation at 400 °C and strain rate 0.01 s^{-1}. Annealing was for 15 min between the two hits.

Fig. 5.10 shows two compression curves from two samples measured at double-hit experiments. For each sample, the temperature of 400 °C and strain rate of 0.01 s^{-1} were used for deformation. One sample was annealed at 1000 °C/15 min after first deformation to the strain of 0.3, the other sample was annealed at 1200 °C/15 min. Second deformation was continued until reaching total strain of 0.6. Despite having some deviations in the initial stage of the first deformation, both curves reach approx. the same value of stress at deformation 0.3. The differences in the early stage of first deformation, could be caused by different orientation of grains in scale of mm and thus different average Schmidt factor.

Upon reaching the strain of 0.3, more slip systems are activated and both samples reach approx. the same true stress value.

After annealing, the deformation continues until the strain of 0.6. Deformation introduced into material during the second deformation is lower than 0.3, as seen in compressive curves (large gap between strain 0.3 and start of second elastic deformation).

True stress reached during the second hit is higher for sample annealed at 1200 °C by approx. 50 MPa. This difference might be connected to microstructural differences of both samples cause during the annealing, as explained below together with the EBSD measurements). An interesting observation is, that sharp yield point is not observed at this temperature, therefore the undulation present at 800 °C and 900 °C is caused probably by dynamic recovery of defects (recrystallization was not observed in the microstructure).

5.2.5 EBSD measurements after double hit experiments

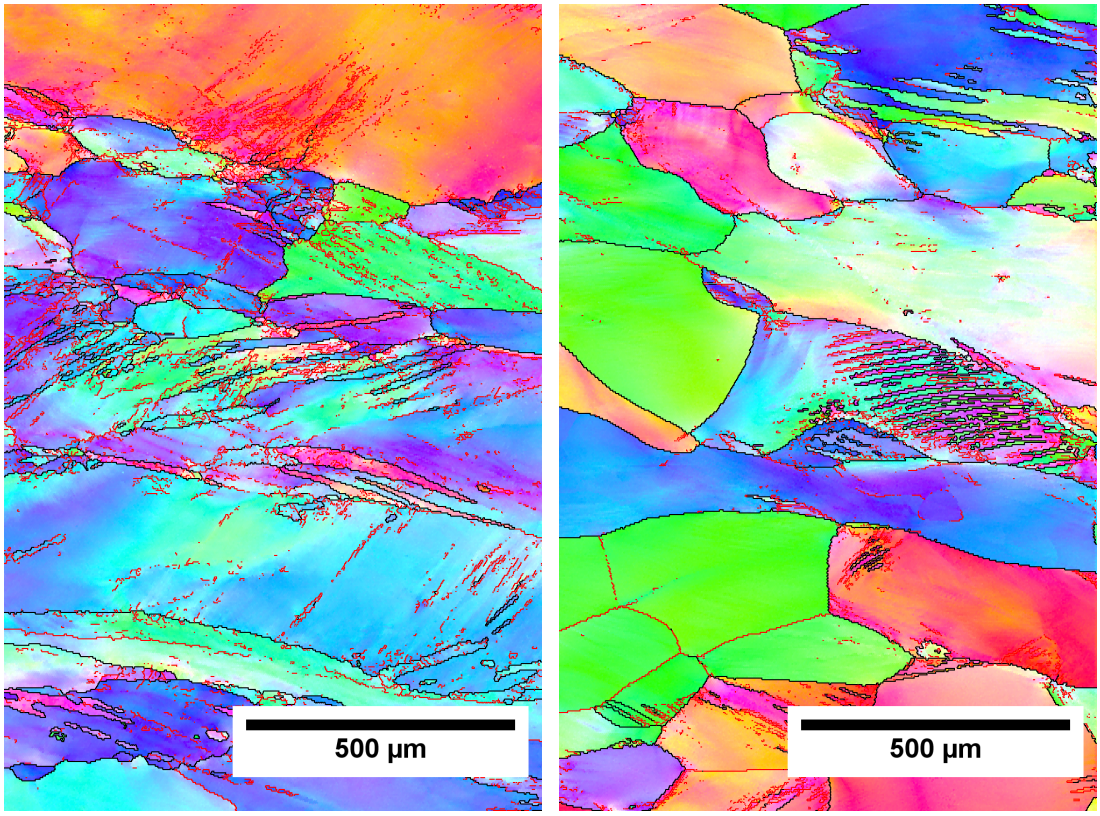

(a) (b)

Figure 5.11: IPF maps of samples after double hit experiments, with annealing temperature a) 1000 °C and b) 1000 °C.

EBSD scans with the size of 1×2 mm were taken with the step size of 3.5 µm. Resulting IPF maps are shown in Fig. 5.11. Both samples contain accordingly oriented low-angle GBs and deformation bands, therefore the deformation conditions used (T = 400 °C; $\dot{\varepsilon} = 0.01$ s^{-1}) share the deformation mechanism with conditions T= 800 °C - 900 °C; $\dot{\varepsilon} = 1$ s^{-1}. Grain size in both samples is very

similar, some smaller grains (hundreds of µm) are present on GBs, that possibly recrystallized during annealing between the two hits. Some grains in the sample annealed at 1200 °C are separated only by low angle GBs (lower part of the Fig. 5.11b – denoted as red lines). This observation indicates, that the continuous recrystallization has occurred, by formation of dislocation walls inside the grains and by increasing the misorientation. The continuous recrystallization and the presence of dislocation walls can explain the higher true stress achieved by sample annealed at 1200 °C. The walls and GBs refrain the dislocations from movement and thus, increase the true stress.

5.2.6 Summary

Single hit experiments showed that UCS of TNTZO is much higher than that of Ti-6Al-4V for the same deformation conditions. On the other hand, the high-temperature mechanical properties are similar to stainless steel AISI 304. In order to achieve sufficient formability, the material should be heated to temperatures over 1100 °C, considering the strain rates, used in industrial practice (around 1 s^{-1}).

The mechanism of deformation changes with temperature and strain rate. At higher temperatures, deformation is concentrated at GBs, whereas at lower temperatures, dislocation slip forms highly oriented deformation bands without apparent recovery.

Double-hit experiments showed that slight continuous recrystallization can be achieved by annealing of the material pre-deformed at low temperatures. The deformation mechanism producing deformation bands and low-angle GBs takes place.

5.3 Die-forging

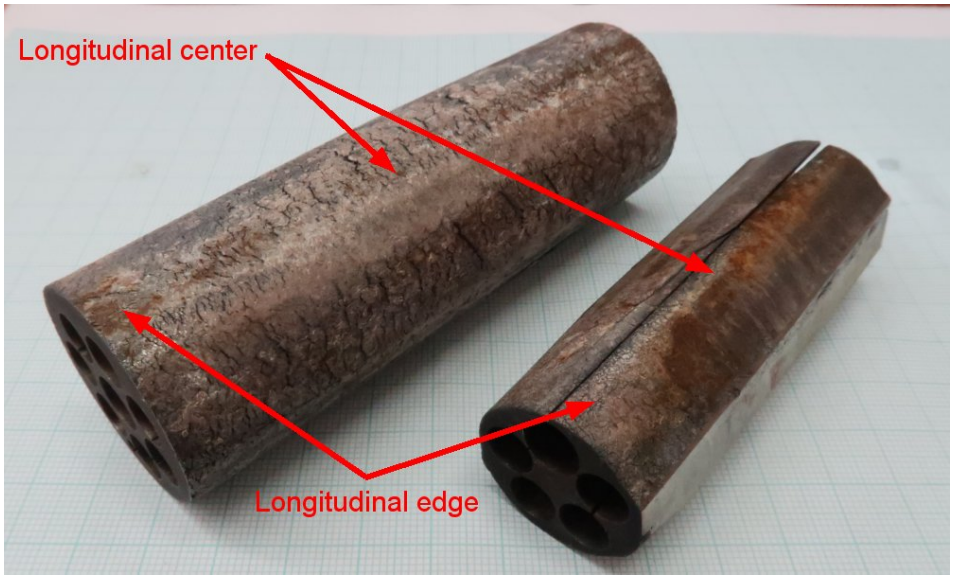

Figure 5.12: Photography of die-forged rods with the diameter 35 mm (left) and 25 mm (right).

Die-forged rods were produced as described in section 3.3.1 with the aim to reduce the porosity and to refine the grain structure. The rods were heated to 1200 °C, however, the rods cooled down below approx. 800 °C during the process and this severely reduced their formability.

The picture of both produced rods is shown in Fig. 5.12. The forged rods contain macroscopic surface cracks propagating into the depth of 1 mm - 3 mm. On the other hand, the oxidation is limited to the surface layer only, as the surface color is not white as in case of thick layer of TiO_2 when compared to hot rolled rods (shown in next section 5.4).

5.3.1 Scanning electron microscopy

Samples for SEM were cut from longitudinal center of both 35 mm rod and 25 mm rod, and only from longitudinal edge of 25 mm rod.

Fig. 5.13a shows the microstructure of longitudinal center of 35 mm rod. It is clearly seen, that the porosity from casting was removed, cf. Fig. 5.1a. The grains did not undergo significant refinement during forging but the band-like structure in their interior is the evidence of introduced deformation and formation of deformation bands. However, this deformation is not homogeneous and some grains contain much less of these bands that the others. One example of such grain is in Fig. 5.13b. The channeling contrast in a large grain interior changes continuously, indicating only minor imposed strain. Similar microstructure was found in the whole cross-section with no big differences on the edge and in the center.

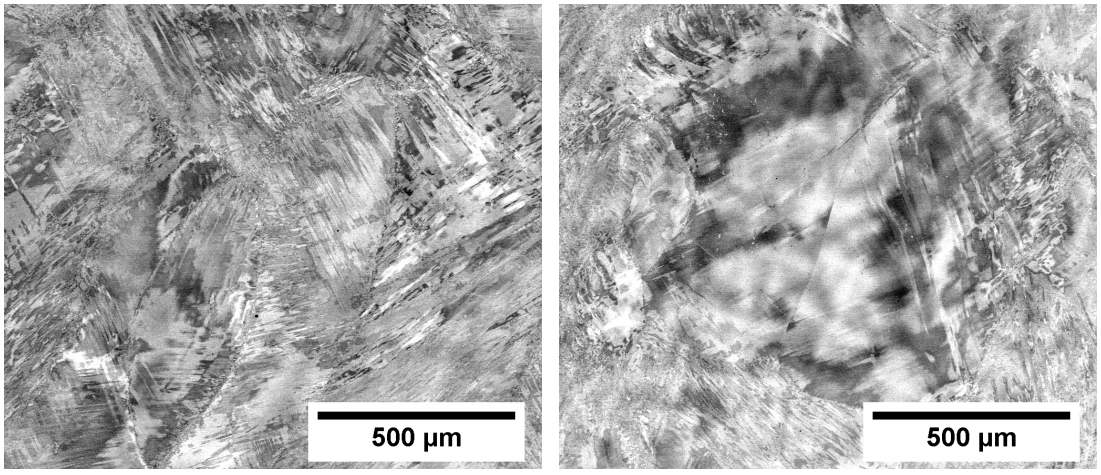

(a) (b)

Figure 5.13: Microstructure (BSE) of 35 mm forged rod: a) overview, b) example of non-deformed grain.

Fig. 5.14a shows the microstructure of the 25 mm rod on the longitudinal edge. As observed also in the 35 mm rod, the porosity from casting is removed. Moreover, GB cracks that are present in samples after formability testing, cf. Fig. 5.6b, are not introduced during die-forging. Possible reason is that the deformation during die-forging is multidirectional, while the compression tests were only in single axial direction. Significant structure refinement is observed. Note

that the scale bar in Fig.5.14 is 5 times smaller than in the case of 35 mm rod images (cf. Fig. 5.13). Dark regions are chemical inhomogeneities from casting. Fig. 5.14b shows the microstructure of 25 mm rod in the longitudinal center. In both images, heavily deformed structure disallows to recognize individual grains. It is therefore necessary to employ the EBSD technique to characterize the microstructure.

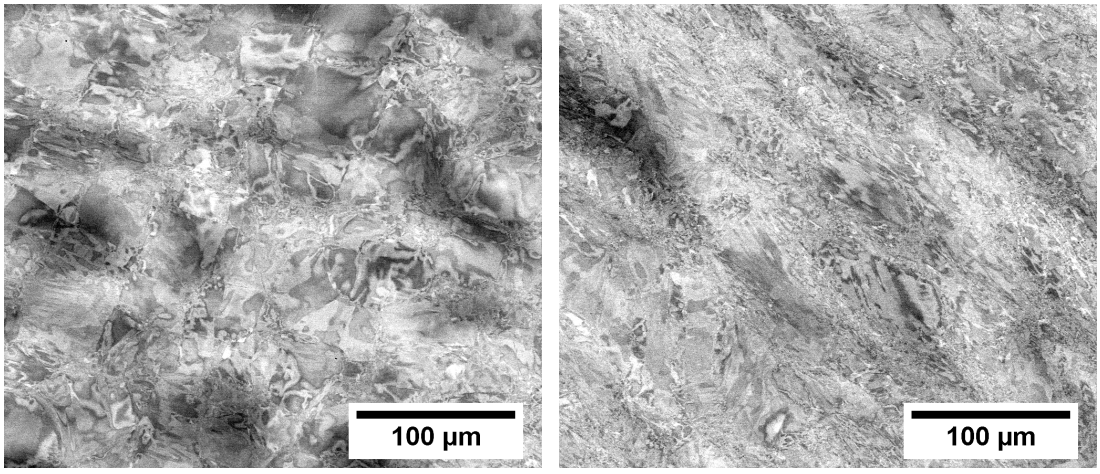

(a) (b)

Figure 5.14: Microstructure (BSE) of 25 mm forged rod: a) longitudinal edge, b) center.

5.3.2 EBSD measurements

IPF map from the rod forged to 35 mm is shown in Fig. 5.15. High resolution EBSD scan was taken to obtain this image (1100 µm × 1100 µm with step size 0.5 µm) to capture both the large scale and small scale effects.

On the large scale, large grains are present from casting as already seen. The grains have mainly [110] orientation parallel with axial direction of the rod. Although the number of grains present from casting is not sufficient for definite conclusion about texture formation, the fraction of these green colored areas is certainly large. On the other hand, Ti-Nb-Zr-Ta-O based alloys are known to form [110] texture during cold swaging [73] and thus even hot die-forging could behave in a similar way, especially when the temperature of forged material substantially dropped due to the contact with die and air. By the end of each step of forging, the temperature dropped below approx. 800 °C.

On the small scale of several micrometers or tens of micrometers, parallel low-angle GBs in the individual grains as seen. The boundaries are in fact the bands that were seen in the BSE images; cf. 5.13a. They probably formed by dislocation slip and not twinning as seen in section 5.2. In the large grain in the center, dislocations from multiple slip systems are active. Resulting low-angle and also high-angle GBs form a new, refined grain structure, by intersecting each other. Unfortunately, this mechanism of refining the grains was not active in the whole structure and some of the grains remained non-deformed or only slightly deformed (such as the two grains above the scale bar) as their Schmidt

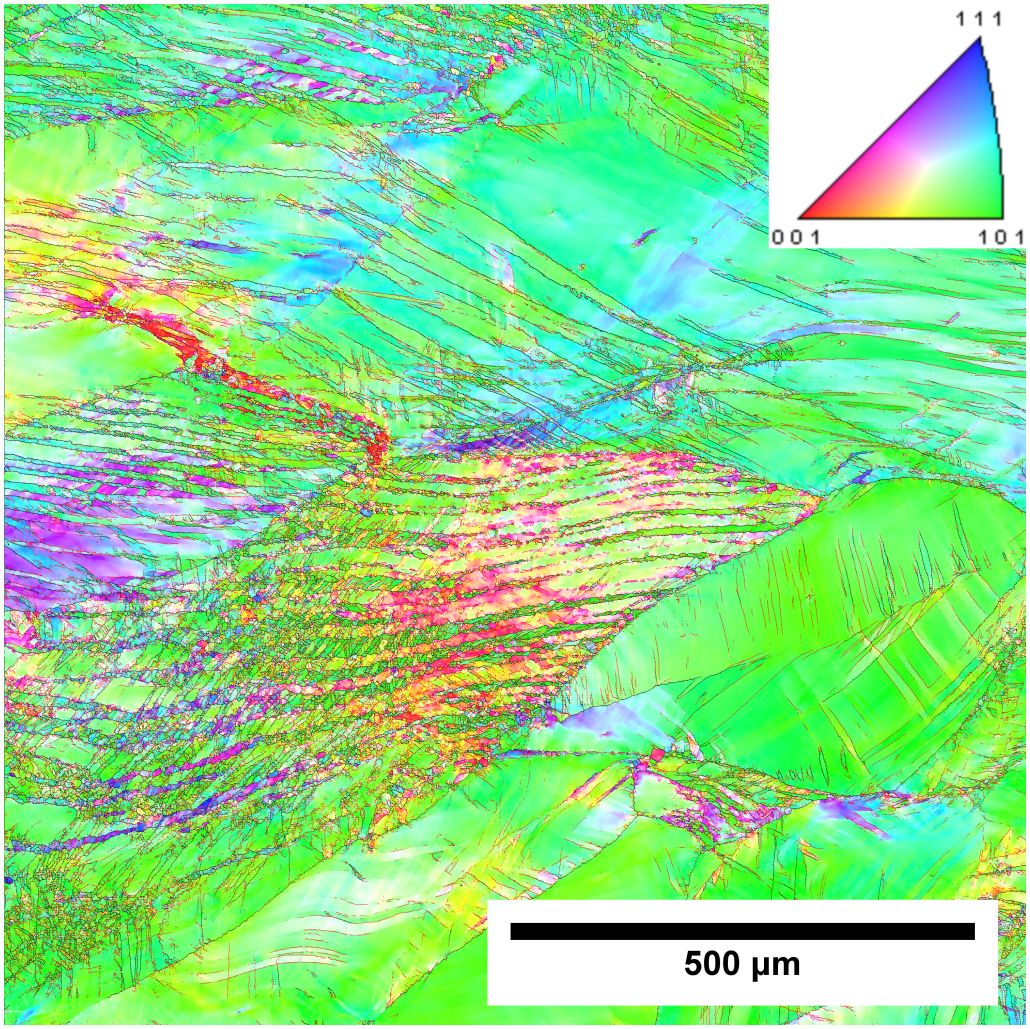

Figure 5.15: IPF map of rod forged to 35 mm.

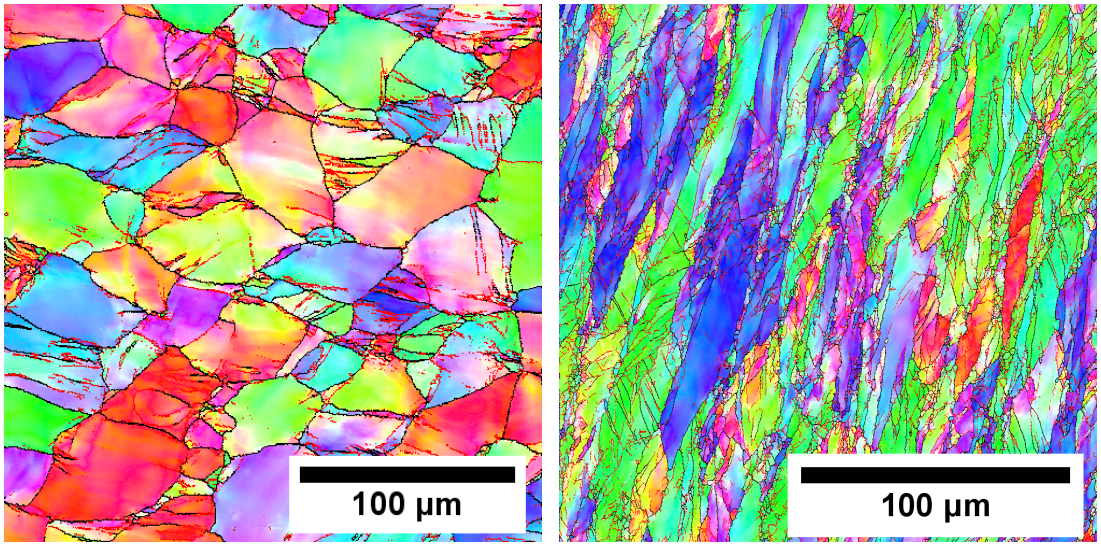

(a) (b)

Figure 5.16: IPF maps of 25 mm forged rod: a) longitudinal edge, b) center.

factor was low even for this multidirectional deformation. The presence of these slip bands reflects the low deformation temperature at which this mechanism operates and is consistent with the [110] texture previously seen in cold-swaged rods. Recrystallization was not observed, probably due to substantial drop of the temperature of the forged rod.

IPF maps from rod forged to 25 mm from longitudinal edge and center are shown in Figs. 5.16a and 5.16b respectively. The edge contains grains with the size around 50 µm. These grains contain only few deformation bands which indicates that they recrystallized from the deformed structure during three-step heating and deformation (rods forged to 25 mm were heated three times before reaching the final diameter as described in section 3.3.1). There is no apparent texture, therefore the recrystallization was most probably discontinuous.

In the center of the rod, the grains are elongated and smaller than on the edge. They also contain high fraction of low-angle GBs. This is probably caused by higher deformation in this part of the rod (longitudinal center), since there was an outflow of material between the dies during forging. The average grain size in this region is around 20 µm. The [110] texture is again visible. It may be formed by higher deformation that again, corresponds to cold deformation that forms this texture, or by incomplete recrystallization during the temperature drop. In this case, the texture was formed already in the previous forging step.

5.3.3 Microhardness measurements

Microhardness values of die-forged rods are shown in Table 5.1 together with microhardness of the cast condition. Slight increase of microhardness is observed for 25 mm rod.

Table 5.1: Microhardness in die-forged rods and cast ingot.

Microhardness (HV)		
Position	Center	Edge
35 mm rod	339 ± 6	–
25 mm rod	348 ± 10	344 ± 5
Cast ingot	326 ± 6	

5.3.4 Tensile testing

Four tensile samples from 35 mm rod and three samples from 25 mm rod were measured. Apparently, the microstructural inhomogeneity of the 35 mm affected the tensile properties since one of the samples had YS below 950 MPa while others had values around 1100 MPa. Moreover, exhibited ductility of one sample was below 10% while the others exhibited ductility above 15%. The samples from 25 mm rod also exhibited different tensile properties. However, the difference was only minor caused probably by initial position of samples (edge vs. the center).

Representative flow curves from forged rods, together with the flow curve from as-cast material, are shown in Fig. 5.17. The differences in the YS are obvious. Also the sharp yield point is more pronounced in the forged rods due to higher dislocation density introduced during deformation, that causes more progressive

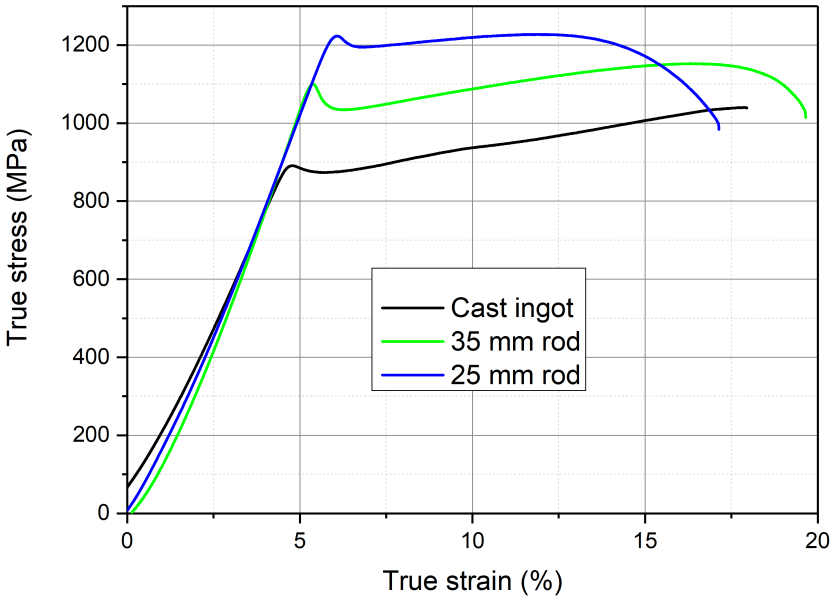

Figure 5.17: Tensile curves from forged rods and cast ingot.

pinning by oxygen atoms. The three flow curves differ in fracture mode. The cast material undergoes sudden brittle fracture while in forged material, the necking occurs. In the 25 mm rod, the neck is formed much sooner than in the 35 mm rod, probably by saturated hardening rate in 25 mm rod that does not exceed the instability of deformation.

5.3.5 Fatigue testing

Fig. 5.18 shows S-N plot measured for both die-forged conditions together with data from the cast ingot. The data from both conditions showed large spread of values. This spread is attributed to microstructural inhomogeneity of the material.

The 35 mm rod shows poor fatigue resistance. Even after measuring 11 samples on stress amplitudes as low as 350 MPa, the 10 million cycles to failure were not reached. The low fatigue strength is most probably caused by inhomogeneously distributed deformation in the material and lack of significant grain refinement, as shown in IPF map, cf. Fig. 5.15. One of the samples, tested on stress amplitude below 400 MPa failed even before 2000 cycles, which is worse than in the case of cast ingot.

The spread of values was large also in 25 mm rod, but the numbers of cycles to failure was higher or at least comparable to the cast ingot. The fatigue limit was estimated to be below 400 MPa as two samples tested with slightly higher stress amplitude between 410 MPa and 440 MPa failed before reaching 100 000 cycles. Therefore, the determined fatigue limit is ambiguous. The large spread of values in 25 mm rod is attributed to macroscopic inhomogeneity of the rod, as there was different microstructure in the center and on the edge of produced rod.

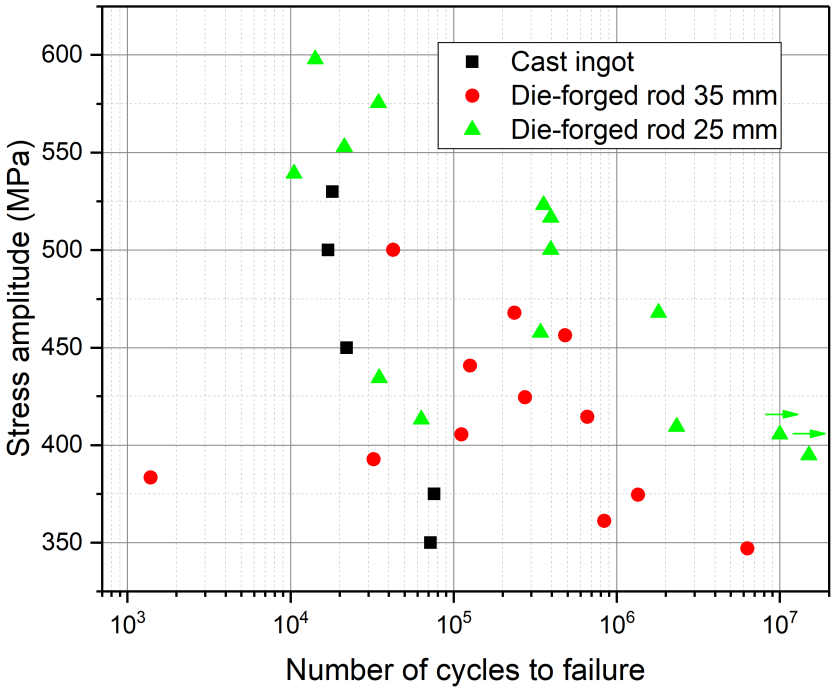

Figure 5.18: S-N plot for the forged rods and cast ingot.

5.3.6 Summary

Characterization of two die-forged rods showed very significant differences. Grain structure cannot be refined by single step die-forging (35 mm rod - single heating). The deformation introduced into the material is not homogeneous as significantly lower amount of deformation bands was found in some grains. On the other hand, three-step die-forging (25 mm – three heatings), resulted in the recrystallized microstructure with average grain size of 50 µm in the longitudinal edge of the rod and 20 µm in the longitudinal center. This difference is probably caused by higher deformation imposed in the center of the rod. Porosity from casting is removed in both produced conditions.

The [110] texture thet was formed during a single step die-forging (35 mm rod) is common in cold-swaged β Ti alloys [[61]. The melting temperature of the TNTZO alloy is estimated to lie between 1800 °C and 1900 °C while the the temperature during forging dropped below 800 °C. Therefore, this texture is probably caused by low homological temperature during the deformation, leading to texture formation, observed in cold deformation. This texture is not present after three step forging on the edge of rod, due to discontinuous recrystallization, taking place either during heating or during deformation. In the center of rod, the [110] texture is partially present. It is either caused by the deformation of the recrystallized structure at the low homological temperature or it is indicating incomplete recrystallization. The reason of reappearing during further deformetion is more likely true, as the grain size was smaller in the center of rod, where this texture was again found.

Tensile properties were significantly enhanced by die-forging. Achieved YS is approx. 1050 MPa for 35 mm rod, while for the 25 mm rod, the YS is approx. 1250 MPa. The main reason of strengthening is a higher deformation (work hardening) introduced into material during forging and reduced grain size.

Fatigue measurements exhibit large spread of values in both conditions that is attributed to microstructural inhomogeneities. Fatigue resistance is poor in 35 mm rod. The fatigue limit could not be determined. Since the porosity is removed by die-forging, the cause for the poor fatigue resistance is a large grain size that was not significantly affected by the processing. On the other hand, 25 mm rod exhibits much better fatigue properties, although the spread of values is still large. Fatigue limit lower than 400 MPa is estimated. This time, the large spread is attributed to microstructural differences (i.e. grain size, texture) in various positions in the produced rod.

Die-forging was shown to be capable of producing material with high scatter of fatigue properties even after reduction of diameter from 45 mm to 25 mm. Microstructure without porosity and with grain size in range of tens of µm is formed. The fatigue properties limit the practical use of TNTZO alloy after die-forging.

5.4 Hot rolling

The TNTZO alloy after casting was subjected to hot rolling. This type of TM treatment is relatively economic as large amount of a material (long rod), can be processed.

Hot rolled rods are shown in Fig. 5.19. The rods have white surface after processing indicating thick layer of TiO_2 that has naturaly white color. This means, that as compared to die-forging, there was much more oxidation due to longer exposure to high temperatures (rolling process took around 3 h). Surface cracks were also forming in die-forged rods. However the oxidation this time deteriorated thicker layer than the cracks.

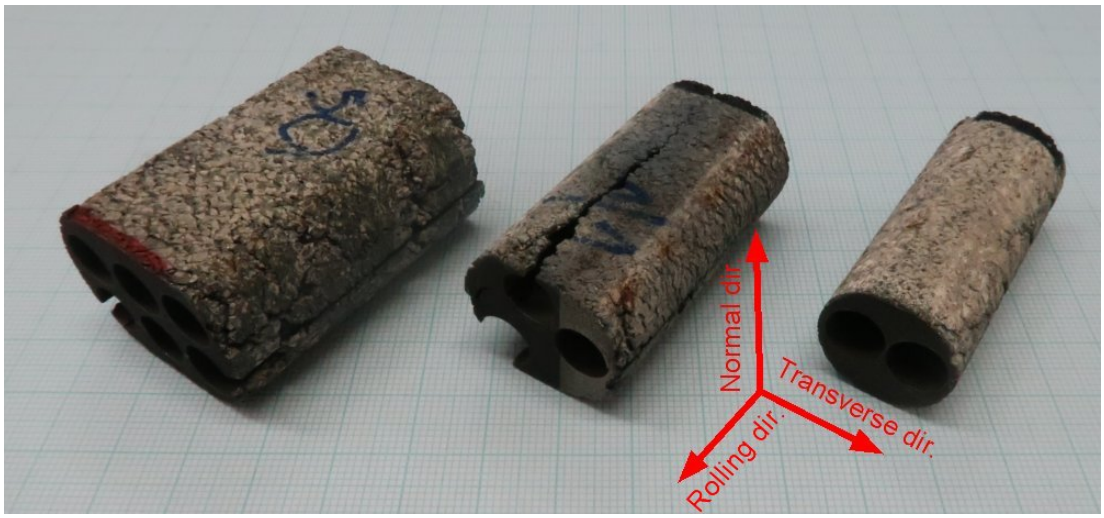

Figure 5.19: Photography of the three rods produced by hot rolling. From left to right: 33 mm, 25 mm and 20 mm condition. Main directions are marked.

5.4.1 Scanning electron microscopy

Samples for SEM observations were taken from 3 positions in each rod, as shown in Fig. 3.1. Table 5.2 summarizes their marks.

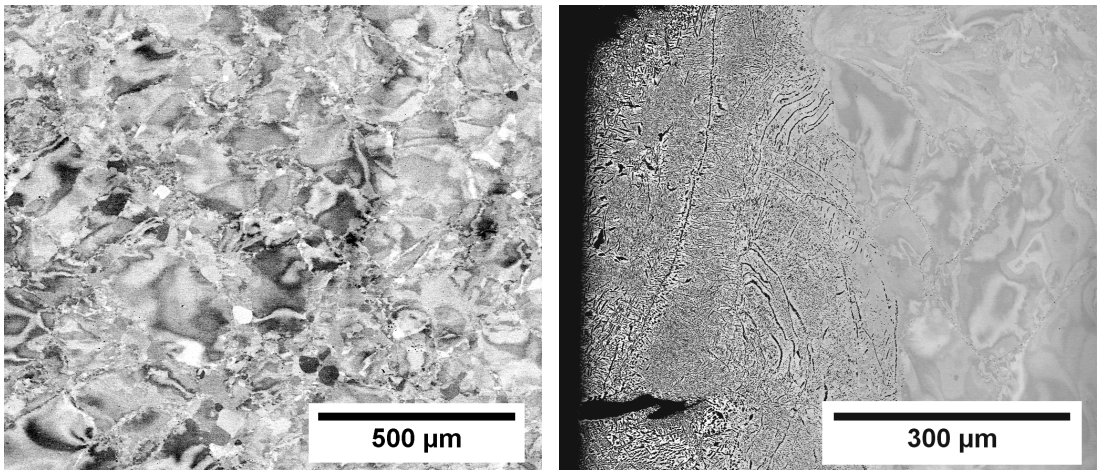

(a) (b)

Figure 5.20: a) Microstructure of rod with diameter 33 mm – center (C33), b) α phase and crack on normal edge of rod with diameter 20 mm.

SEM observations revealed that porosity present in the as-cast material is removed already in the least deformed condition (diameter 33 mm) as is shown in Figure 5.20a for sample C33. This figure also shows heavily deformed microstructure in which it is difficult to distinguish individual grains and EBSD method needs to be employed as shown below. Fig. 5.20b shows normal edge of rod rolled to diameter 20 mm. α phase is grown to the depth of few hundreds of µm homogeneously and subsequently along the GBs. This is most likely caused by oxygen (α stabilizer) contamination during rolling. Microhardness measurements (shown below) can provide useful information on the depth of the penetration of α phase, since the $\alpha + \beta$ structure is much harder than the β matrix itself.

5.4.2 EBSD measurements

EBSD measurements were taken with the scan size of 1100 µm × 1100 µm and step size of 6 µm. Results are shown in Figs. 5.2, 5.22, 5.13 employing grain orientation spread (GOS) maps.

GOS maps in Fig. 5.21 show the central parts of the three rods (C33, C25 and C20). Increased deformation by rolling clearly causes a progressive grain refinement. The sample C33 contains grains of the size of approx. 0.5 mm, while grain size decreases to values below 100 µm in the 20 mm rod. Moreover, we can observe a growing fraction of blue colored small grains having low GOS values below 1° (4% for C33, 11% for C25 and 18% for C20). The values of GOS below approx. 1° are characteristic for discontinuously recrystallized grains

Table 5.2: Marks of samples from hot rolled rods.

Rod's transversal diameter	Center	Normal edge	Transversal edge
33 mm	C33	N33	T33
25 mm	C25	N25	T25
20 mm	C20	N20	T20

in β-Ti alloys [56]. We can therefore conclude that the fraction of recrystallized grains in the central part increases with increasing deformation. Recrystallized grains nucleate preferentially at GBs of larger grains. As observed in samples after formability testing, there is a higher deformation stored along the GBs.

GOS maps from the normal (N33, N25 and N20) and transverse (T33, T25 and T20) edges of the rolled rods are shown in Figs. 5.22 and 5.23, respectively. Unlike the central parts there is a negligible fraction of recrystallized grains (less than 2% in all conditions). Grain refinement with decreasing rod diameter is less evident on the edges. On the other hand, an increasing amount of low-angle grain boundaries and an increasing deformation within grains (more red and orange grains) is observed with increasing degree of rolling.

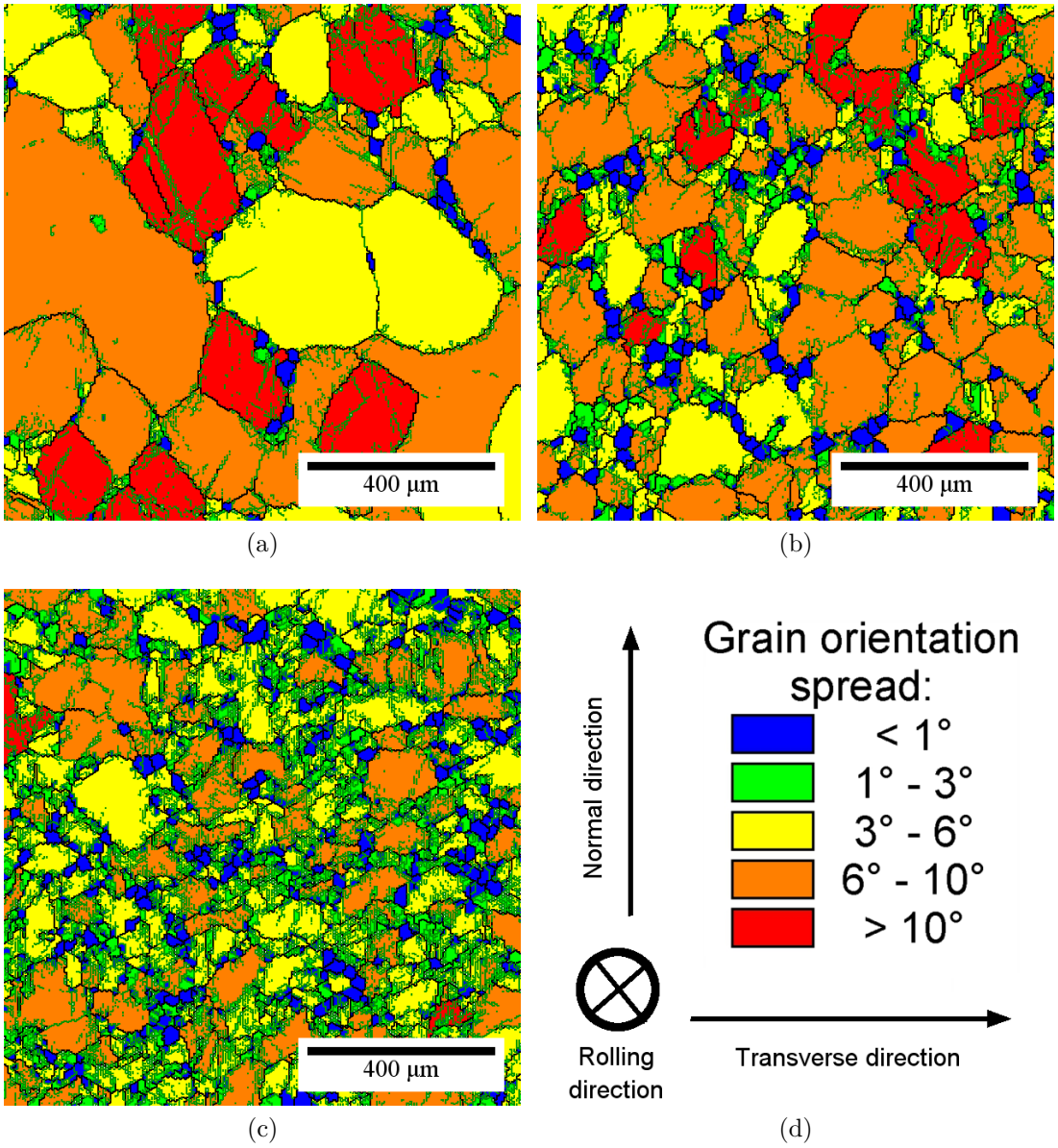

Figure 5.21: GOS maps of hot rolled rods, samples: a) C33, b) C25, c) C20 and d) GOS color code and orientation of EBSD scans.

The absence of recrystallized grains in edges of rods follows from lower degree of deformation and lower temperature when compared to central parts. Higher

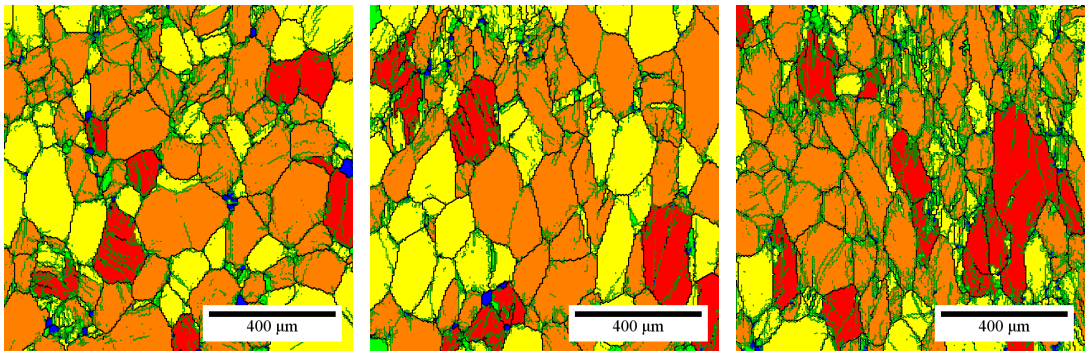

(a) (b) (c)

Figure 5.22: GOS maps of hot rolled rods, samples: a) N33, b) N25 and c) N20.

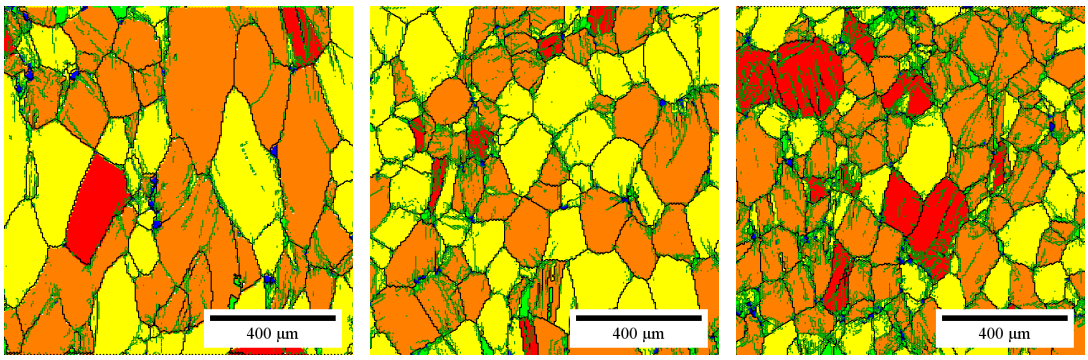

(a) (b) (c)

Figure 5.23: GOS maps of hot rolled rods, samples: a) T33, b) T25 and c) T20.

deformation in the central parts compared to edges was found by FEM modeling for a similar rolling process of a magnesium alloy AZ31 [74]. Furthermore, the central parts of the three rods remained very hot throughout the process due to low thermal conductivity of titanium. On the other hand, the edges were cooled both by contact with the rolls and by surrounding air. These conditions led to discontinuous recrystallization in the central parts while the edges could undergo only recovery processes which were recently found to take place in β-Ti alloys deformed at lower temperatures (820 °C - 900 °C) [56]. Partly recovered dislocation structure can be seen in all present GOS maps as low-angle grain boundaries.

The results indicate, that annealing at temperatures around 1200 °C could refine the deformed grains by discontinuous recrystallization. However, further experiments need to be performed to verify this hypothesis. For more details, see section 5.5, where results from cold swaging and recrystallization annealing are shown.

5.4.3 Microhardness measurements

As observed by SEM, the α phase grows extensively from the surface of the rods. Microhardness was measured with increasing distance from surface in all prepared rods on the normal edge. Resulting plots are shown in Fig. 5.24.

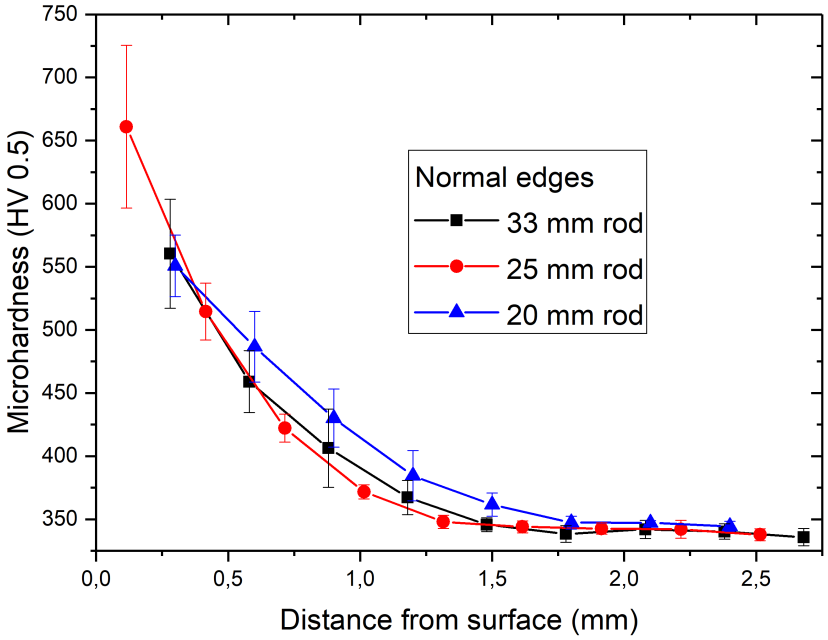

Figure 5.24: Microhardness dependence on distance from surface of the rod.

Table 5.3: Microhardness measurements of different rods/positions.

	Microhardness (HV		
↓ Diameter/position →	Center	Normal edge	Transversal edge
33 mm	343 ± 5	339 ± 7	338 ± 5
25 mm	344 ± 6	342 ± 6	336 ± 6
20 mm	345 ± 7	346 ± 4	335 ± 6

In the nearest proximity to the surface, microhardness achieves values almost double values than in the bulk. The material reaches microhardness of the pure β in the depth of approx. 2 mm. This amount of material is therefore not usable after processing and should be removed for the desired use (implant production). The contamination depth was very similar for all three rods. Only the 20 mm rod (which was held hot the longest time) had slightly higher microhardness in depth around 1 mm, which is within the statistical error.

In Table 5.3, the results of microhardness measurements are shown. The values on the edges were taken from the sufficient distance from the surface, to prevent α phase to affect the measurements. All microhardness variations are within the statistical error (standard deviation); although central parts seem to exhibit slightly higher hardness, as well as the normal edges compared to transverse edges in the more deformed states. Microstructural changes in the central parts (recrystallization and grain refinement) did not significantly affect the microhardness values. However, in comparison with the microhardness of the cast condition, (326 ± 6) HV, the microhardness in rolled material is significantly higher.

5.4.4 Tensile testing

Tensile properties were improved by rolling in all conditions, as compared to cast ingot. Three samples were measured from each rod and the reproducibility of data was very good. Representative flow curves of rolled and cast material are shown in Figure 5.25. The sharp yield point is present and is more pronounced in rolled material, again arguably due to higher dislocation density induced through deformation similarly to the die-forged rods. After the yield point, an extensive strain hardening occurs until the formation of a neck and a ductile fracture. Even more pronounced is the plastic true strain, that reaches values of 20%, that is significantly superior to the ductility of the cast ingot or die-forged rods.

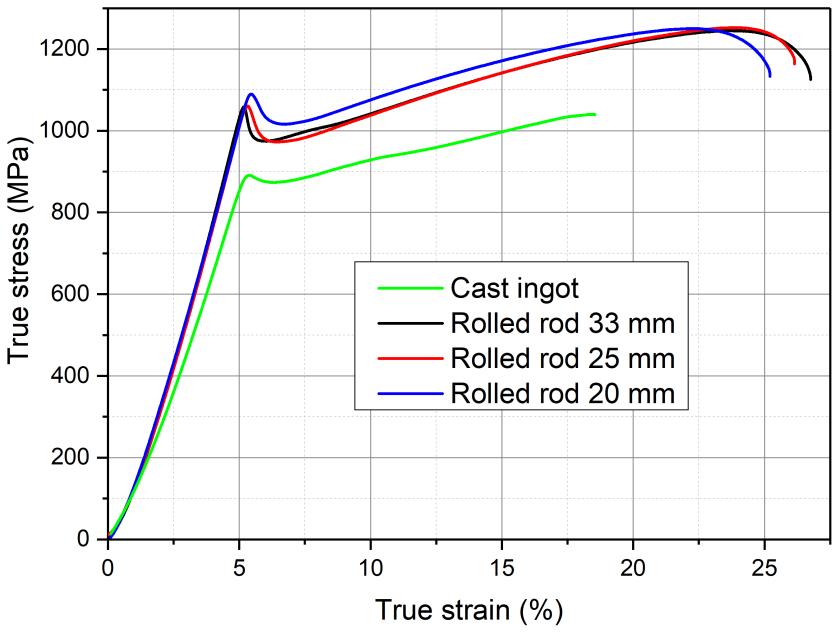

Figure 5.25: Tensile curves of rolled rods and cast ingot for comparison.

5.4.5 Fatigue testing

Fatigue tests were performed on the samples from 33 mm rod and 20 mm rod. The S-N plot containing also the data from cast ingot is shown in Fig. 5.26. The measured values exhibited much lower spread than in die-forged rods, obviously due to much more homogeneous microstructure.

The fatigue resistance for stress amplitudes over 500 MPa is comparable or worse than that of the cast condition. A significant difference is observed between the two tested rods. Rod with diameter of 33 mm continues to have similar fatigue properties even at low stress amplitudes down to 350 MPa.

The rod with the diameter of 25 mm exhibits much better fatigue resistance in the range 400 MPa – 500 MPa. The fatigue limit is about 400 MPa. Therefore, significant improvement is achieved with the highest area reduction. Since the porosity was removed already in the 33 mm rod, this improvement is attributed to grain refinement by deformation and recrystallization during the rolling process. The scatter of values even at 20 mm rod is probably caused by the microstructural differences between the edges and the central parts.

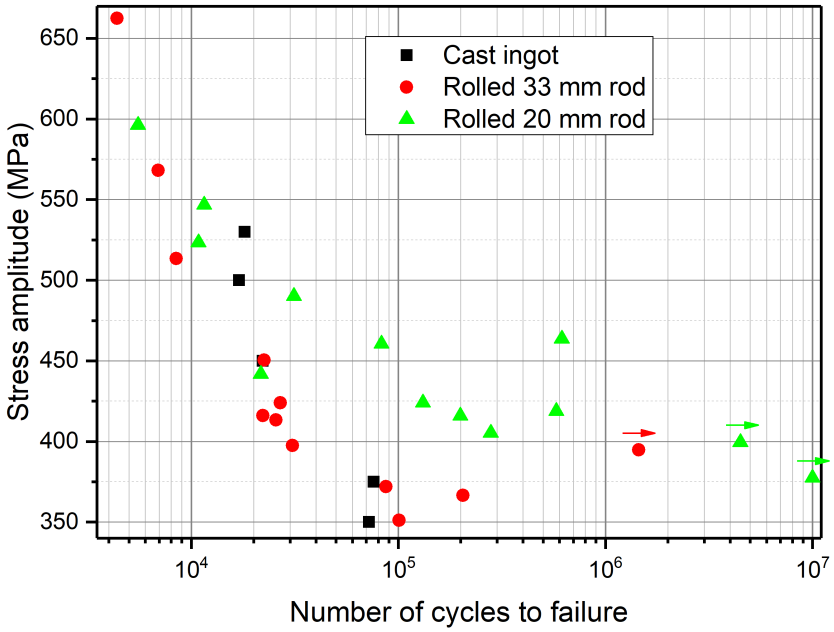

Figure 5.26: S-N plot for the rolled rods (33 mm and 20 mm) and cast ingot.

5.4.6 Summary

Microstructural characterization by SEM and EBSD of three hot rolled rods with diameters 33 mm, 25 mm and 20 mm was performed. Porosity from casting is removed in all three conditions and deformation introduced into material increases with each rolling step. Discontinuous recrystallization occurs in the rod centers due to higher deformation and longer exposition to high temperatures that are needed to suppress the recovery. Recovery is preferred over recrystallization at lower temperatures due to high SFE of β Ti alloys. As a consequence, the material on edges is not recrystallized.

Because of the long exposure to high temperatures in air, significant oxidation has occurred at the surface layer. White color of the surface indicates relatively thick layer of TiO_2. Microhardness measurements showed that the oxidation is significant in 2 mm depth as the α phase is present in this layer enhancing the hardness. For practical use of hot rolling processed material, this layer contaminated by oxygen must be removed.

Tensile properties are significantly enhanced by hot rolling in comparison with the cast ingot. Achieved YS values are comparable to those of the die-forged rod to 35 mm diameter. Moreover, much higher ductility of approx 20% is achieved.

Fatigue measurements showed much lower scatter than in die-forged rods. Fatigue performance of 33 mm rod is similar to that of cast ingot and the fatigue limit could not determined from the measured data. The 20 mm rod exhibits much better fatigue performance, especially for stress amplitudes in the range 400 MPa – 500 MPa. The fatigue limit was estimated to be 400 MPa.

The achieved tensile and fatigue properties in both conditions, the die-forged and the hot rolled rods are summarized in Table 5.4. All TM processed conditions show superior YS and UTS to those of the cast ingot. Significantly higher YS (by approx. 200 MPa) was observed in hot rolled material as compared to cast ingot. The highest value over 1250 MPa is attained in the die-forged rod with

a diameter of 25 mm. The UTS values are also enhanced mostly by approx. 200 MPa as compared to the cast ingot. Only die-forged rod with the diameter 35 mm exhibits the UTS value by only 100 MPa more than in the cast ingot.

Strain to fracture (DF) is enhanced in hot-rolled conditions significantly, by 6% – 8%. The die-forged conditions show comparable (35 mm rod) or lower (25 mm rod) ductility. Also, both die-forged conditions have very high scatter of all measured values. Hot rolled rods are much more homogeneous.

Fatigue limit (FL) could be estimated only in the most deformed condition after hot rolling: 20 mm hot rolled rod. This condition achieved the FL of 400 MPa. The die-forged rods, shows a very large scatter of values attributed to mictrostructural inhomogeniety while the hot rolled rod was much more homogeneous. Most conditions exhibited a poor fatigue performance and the FL was not achieved even at low stress amplitudes of 350 MPa.

Table 5.4: Tensile and fatigue properties of die-forged (DF) and hot rolled rods (HR): yield strength (YS), ultimate tensile strength (UTS), strain to fracture (SF) and fatigue limit (FL).

Rod diameter	YS (MPa)	UTS (MPa)	SF (%)	FL (MPa)
Cast ingot	870 ± 25	1039 ± 38	13.8 ± 1.7	< 350
DF - 35 mm	1053 ± 71	1129 ± 76	14.1 ± 2.9	< 350
DF - 25 mm	1256 ± 68	1264 ± 62	10.4 ± 2.0	< 400
HR - 33 mm	1053 ± 4	1251 ± 4	21.9 ± 0.3	< 350
HR - 25 mm	1078 ± 14	1256 ± 6	20.9 ± 1.2	–
HR - 20 mm	1084 ± 7	1237 ± 19	20.0 ± 1.2	400 ± 10

The conditions after TM processing did not contain porosity from casting, but significantly differed in grain size and deformation introduced into material. This indicates, that the porosity itself does not cause the poor fatigue performance of the cast ingot and the grain structure also plays its role. Moreover, the impact of microstructure is much larger on the fatigue properties than on the tensile properties – difference in YS in hot rolled conditions is less than 3% but difference in FL is well over 15%.

Microstructural observations of both TM processed conditions showed that using appropriate temperature, the grains can be refined in deformed regions by (probably) discontinuous recrystallization. In the next part, we will explore much easier method of TM processing, which is combination of cold swaging and recrystallization annealing. The aim of this method is to produce homogeneously recrystallized grain structure with grain size at least below 100 µm. A fatigue limit of 400 MPa may be expected from this grain size as indicated from results of 20 mm hot rolled rod.

5.5 Cold-swaging + recrystallization annealing

Cold-swaging, as described in section 3.3.3, is a method of metal forming at low temperatures (below 0.3 T_m) aiming to suppress recovery. This method is automatized and introduces deformation into material much more easily than the two methods described in previous sections. It is also much cheaper and easier

because no furnace heating or temperature control is needed, operating personnel is reduced and due to suppressed oxidation at these low temperatures, no material wastage occurs.

The good quality of surface of the material processed by cold-swaging is seen in the photography of rods from series 2 shown in Fig. 5.27.

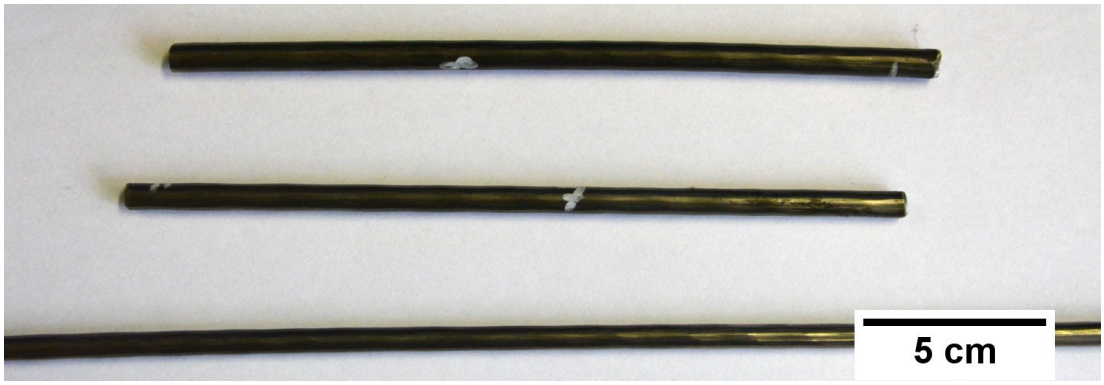

Figure 5.27: Photography of three cold-swaged rods from series 2. From top to bottom: 8 mm, 7 mm and 6.4 mm rod.

The cold-swaging is expected to close the pores if sufficient area reduction (AR) is used. In order to boost the fatigue resistance, subsequent grain refinement achieved by recrystallization annealing should have a positive effect on the fatigue resistance. Since the conditions (amount of cold deformation, temperature and time of annealing) were completely unknown for this material, rather wide intervals of the input parameters were chosen in the first attempt and were further optimized.

In contrast to previous sections, the subsections will not be named according to characterization method used, but according to sample preparation route:

- Series 1 of CSW - rods with area reduction of 40%, 65% and 80% and no rotation of rods during CSW.
- Annealing of series 1 at wide range of temperatues for a defined time.
- Series 1 of CSW - rods with area reduction of 72%, 78% and 82% with rotation of rods during CSW.
- Annealing of series 2 at narrower range of temperatures for various times.

5.5.1 Cold-swaging series 1

As described in subsection 3.3.3, three rods were prepared in UJP Praha, a.s. by cold-swaging from 9 mm rod with following area reductions: 40%, 65% and 80% (CSW40, CSW65, CSW80 respectively).

Fig. 5.28a shows SEM – BSE image of CSW40. Large grains from casting are still present, but heavily deformed. Black area in lower part of the image is a pore that was not closed by the deformation. Apparently, the deformation was not sufficient. In CSW65, the pores are closed, but cracking was observed in the material. An example of such a crack is shown in Fig. 5.28a. Even after thorough

examination, neither pores or cracks were not found in CSW80. Therefore the deformation needed to completely close both the pores and the cracks is located between 65% and 80% of area reduction.

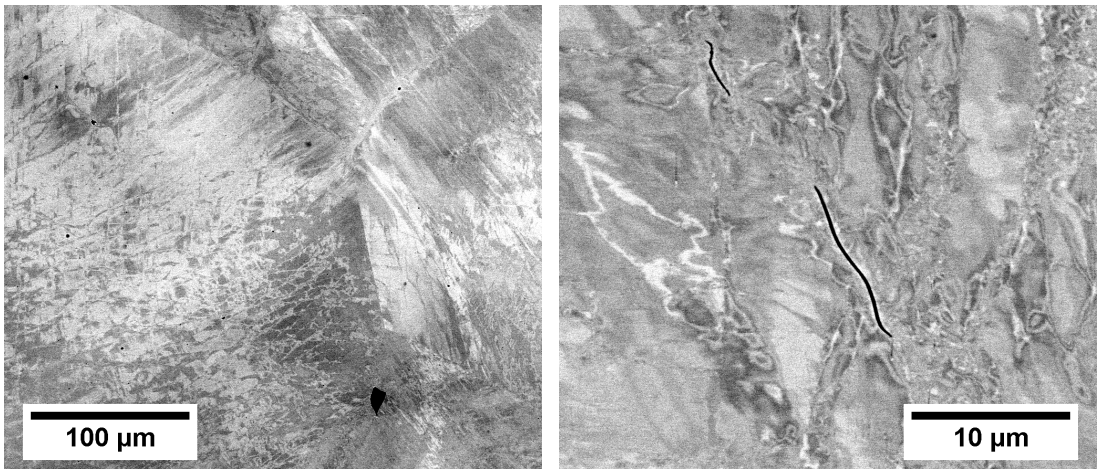

(a) (b)

Figure 5.28: SEM images of a) overview of CSW40, b) pore in CSW65.

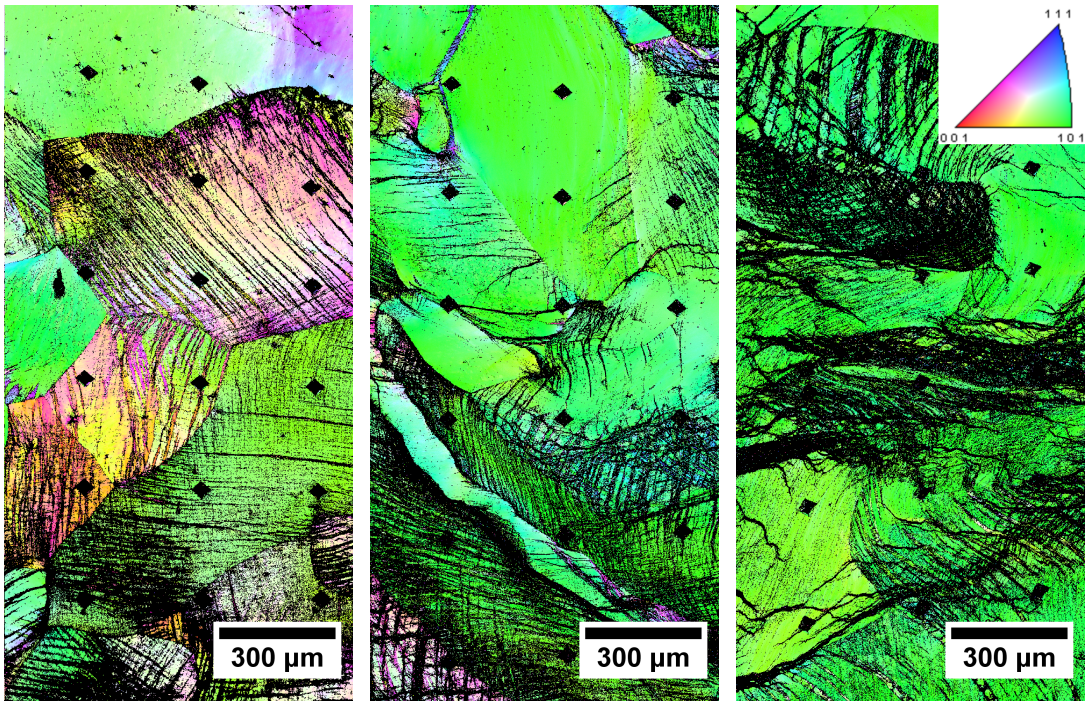

(a) (b) (c)

Figure 5.29: IPF maps from a) CSW40, b) CSW65, c) CSW80. CI $>$ 0.2.

EBSD measurements were performed on all three cold-swaged conditions with scan area of 3×1 mm. Representative IPF maps are shown in Fig. 5.29 where points with confidence index (CI) $<$ 0.2 are drawn in black. Indentations from microhardness measurements are visible in the images as black dots that were not indexed. Bands inside the grains were also not indexed. These bands are

the deformation bands containing high dislocation density. Regions with high dislocation density do not diffract and thus, the Kikuchi patterns are not formed while measuring these points. Upon closer inspection, the distribution of the deformation bands varies with area reduction of samples. Samples CSW40 and CSW65contain grains which are nearly completely free of these bands. All grains measured in CSW80 sample contain the deformation bands and the 80% area reduction provide more homogeneous deformation of all grains in this material.

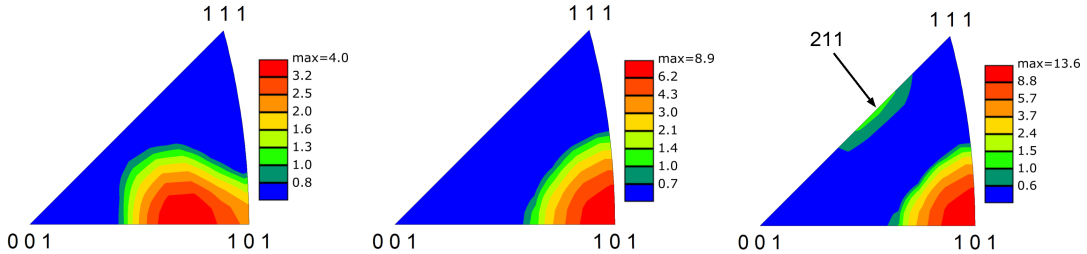

Figure 5.30: IPFs from a) CSW40, b) CSW65, c) CSW80.

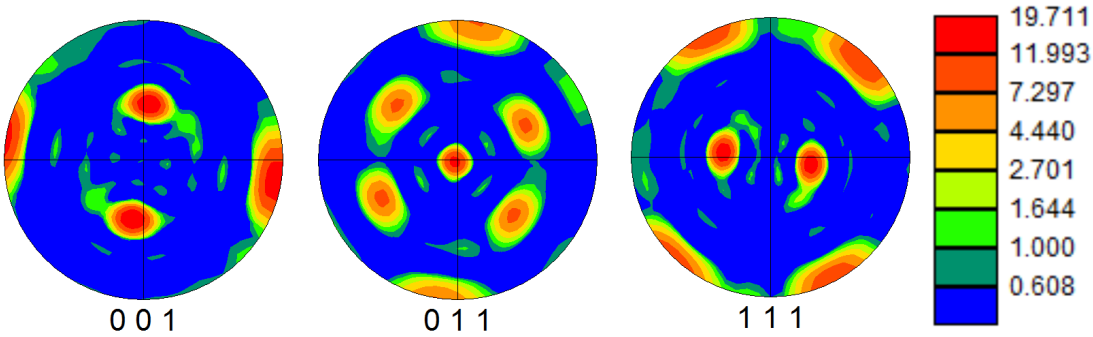

Figure 5.31: PFs of CSW80.

In the IPF maps [110] texture formation is seen that is parallel to swaging (axial) direction. In order to examine this texture more thoroughly, inverse pole figures (IPF's) were computed from the whole EBSD scans (of the size 3 m $\times$ 1 mm) of all three cold-swaged rods. The results are shown in Fig. 5.30. The intensity of texture of the three conditions varies is different. The texture index (intensity of the strongest orientation that signifies, how this orientation is stronger than a random orientation) reaches values of approx. 4 at 40% of AR, nearly 9 at 65% of AR and over 13.5 in case of 80% of AR.

The texture formation can be used as the explanation, why some grains do not deform until reaching some area reduction. The [110] texture is preferred to others in the Ti-Nb-Zr-Ta-O based alloys processed by cold-swaging [73]. Therefore, through stress introduced into material by cold deformation, grains are preferentially deformed in such way to form the [110] texture. However, if the grain is initially already in the [110] orientation, there is lack of the driving force for deformation and grain remains non deformed even at high area reductions. If the grain finally undergoes the plastic deformation by dislocation slip, there is another texture component in approx. [211] direction arising in the IPF. However, this component is very weak in contrast to the main [110] component.

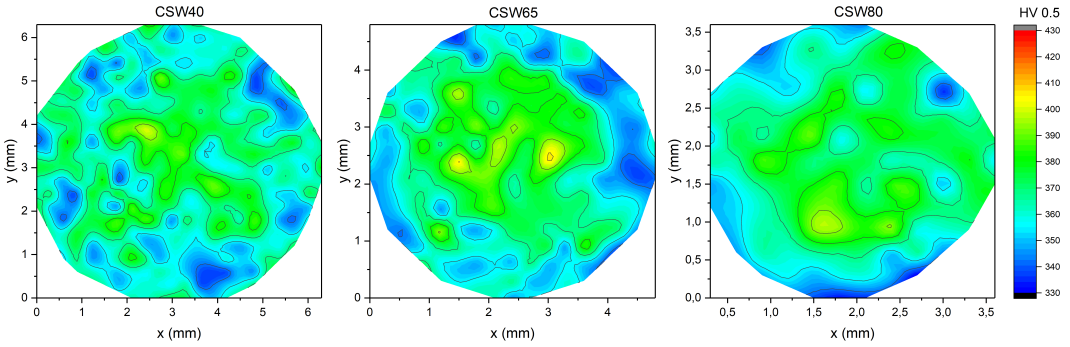

(a) (b) (c)

Figure 5.32: Microhardness maps of cold-swaged rods a) CSW40, b) CSW65, c) CSW80.

Another interesting texture property is connected to the geometry of the cold-swaging process. In the CSW80 sample, the texture became strongly oriented with respect to swaging dies (rods were not rotated in the machine while swaging). Fig. 5.31 shows complete pole figures (PF's) of CSW80. The texture shown there is very similar to that of a single crystal. Most points attain such orientation that the [001] direction that is perpendicular to [110] plane in the swaging direction is oriented to the left and right in the figure. Some minor components are also observed in the IPF above.

Microhardness maps measured in the cross sections of the cold-swaged rods are shown in Fig. 5.32. Microhardness decreases towards the edges, which indicates that the deformation and related dislocation density causing higher hardness are higher at the center of the rods. However, this growth is not very homogeneous (axially symmetric) probably because of lack of deformation in the grains initially oriented in the [110] direction. The highest hardness is observed in sample CSW65 and not in CSW80 as expected from higher introduced deformation. The reason is probably in different texture: orientations [110] and [100] are the softest orientations in BCC materials and after 80% of area reduction, there is almost only the [110] orientation as shown in Fig. 5.31.

5.5.2 Cold-swaging series 1 + recrystallization annealing

Rather wide range of temperatures was chosen for testing of recrystallization annealing. Prepared conditions from series 1 of CSW rods are summarized in Table 5.5.

Table 5.5: Conditions prepared by annealing of series 1 of CSW rods.

CSW series 1	Thermal processing		
CSW40	800 °C/15 min	1000 °C/15 min	1200 °C/15 min
CSW65	–	1000 °C/15 min	1200 °C/15 min
	1200 °C/2 min + 800 °C/15 min		
CSW80	800 °C/15 min	1000 °C/15 min	1200 °C/15 min
	1200 °C/2 min + 800 °C/15 min		

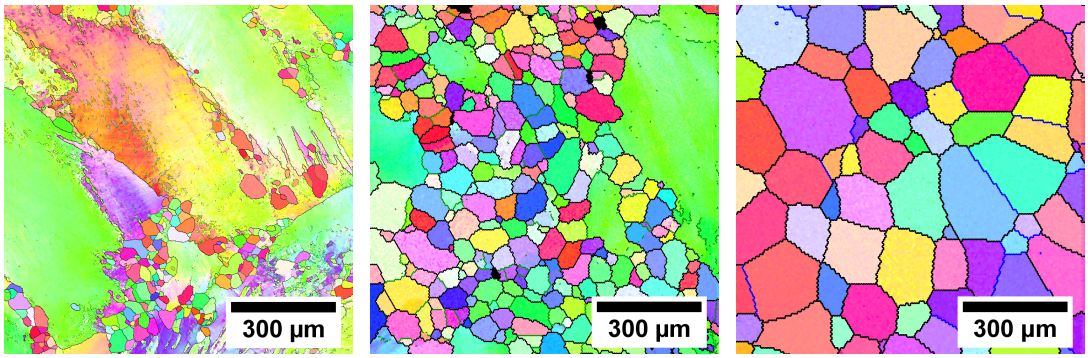

(a) (b) (c)

Figure 5.33: IPF maps from CSW40 samples annealed for 15 min at: a) 800 °C, b) 1000 °C, c) 1200 °C.

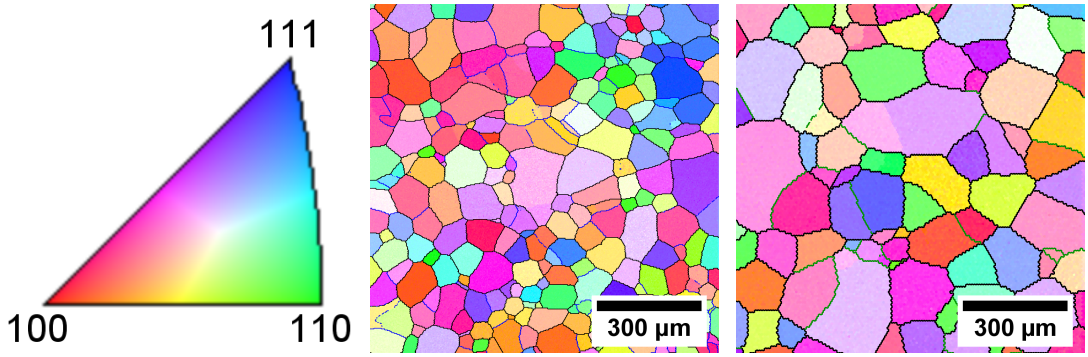

(a) (b) (c)

Figure 5.34: a) Orientation triangle. IPF maps from CSW65 samples annealed for 15 min at: b) 1000 °C and c) 1200 °C.

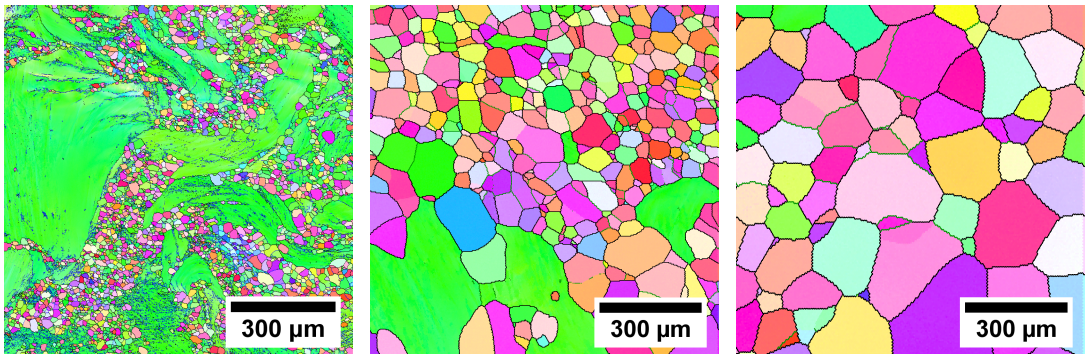

(a) (b) (c)

Figure 5.35: IPF maps from CSW80 samples annealed for 15 min at: a) 800 °C, b) 1000 °C, c) 1200 °C.

Upon annealing in the studied range of temperatures for 15 min, new grains begin to nucleate and grow in the deformed structure. Depending on the temperature of annealing and amount of stored deformation, the resulting microstructure changes significantly. EBSD measurements were conducted for each sample. The scan size was 3 × 1 mm and the step size was chosen accordingly to a fineness of a

measured structure. Figs. 5.33, 5.34 and 5.35 shows representative 1 × 1 mm IPF maps of annealed samples from CSW40, CSW65 and CSW80 rods respectively.

Samples annealed at the lowest temperature of 800 °C for 15 min (Figs. 5.33a, 5.35a) show only minor refinement of the grain structure. Most of the deformed grains are not recrystallized and have preserved their [110] texture while undergoing recovery (unlike the cold-swaged samples, here majority of points, the diffraction could be successfully obtained and indexed). Recrystallized fraction contains grains of size of only tens of µm. However, due to preferred recovery, prolonging of the annealing would probably not result in further recrystallization.

Annealing at 1000 °C leads to more homogeneous recrystallization. Few remaining large grains with [110] texture can be still found. Apparently, there was not enough deformation introduced by cold-swaging for recrystallization, even in the most deformed condition, CSW80. The recrystallized grain size is approx. 100 µm.

Annealing at 1200 °C leads to complete recrystallization, but also to progressive grain growth of the recrystallized grains. The achieved grain size over 150 µm is similar for all three CSW samples. The [110] texture completely vanishes.

Two-step annealing was proposed to profit from high recrystallization rate at 1200 °C and suppressed grain growth at 800 °C. Samples CSW65 and CSW80 were annealed at 1200 °C/2 min to nucleate new grains and immediate annealing at 800 °C/15 min followed to stabilize the recrystallized microstructure. Fig. 5.36 shows representative IPF maps from both conditions annealed in two steps. While in the CSW65 rod, this heat treatment leads to incomplete recrystallization, the CSW80 rod is completely recrystallized with the grain size of approx. 100 µm.

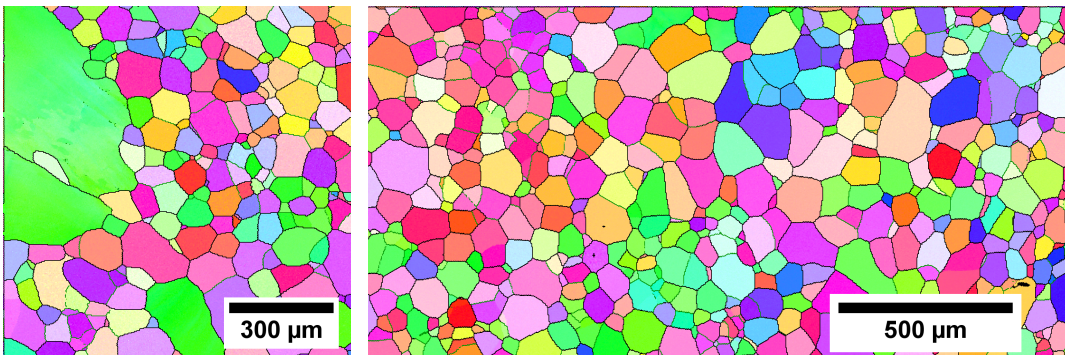

(a) (b)

Figure 5.36: IPF map from samples annealed at 1200 °C/2 min + 800 °C/15 min from a) CSW65 rod and b) CSW80 rod.

The achieved average grain sizes of recrystallized fractions from all measured samples are summarized in Table 5.6. As the EBSD scans of sizes of 3 mm×1 mm measured, a significant area of the samples with diameters of 5 mm was captured. At temperatures 800 °C and 1000 °C, the grains are smaller with higher area reduction. The deformed structure is blocking the grain growth. This is not the case at temperature 1200 °C, where two conditions with lesser area reduction have by coincidence the same grain size and the condition with the highest area reduction has the largest grains. This phenomenon shows that the structure indeed undergoes the grain growth during annealing at 1200 °C for 15 min. In case of

two-step annealing (1200 °C/2 min + 800 °C/15 min), complete recrystallization was achieved in the CSW80 sample. The average grain size is under 100 µm. This approach seems to be promising, but it is difficult if not impossible to achieve annealing this short, because larger amounts of material as needed for joint implant production. The large volume does not reach the desired temperature during this short annealing. Due to this reason, only single step heat treatments are studied in series 2 of CSW rods.

Table 5.6: Grain sizes determined from measured EBSD maps of annealed samples. Recrystallized fraction is given in brackets if the grain size was computed only from part of the measured map.

Average grain size (µm)			
Single-step annealing	800 °C/15 min	1000 °C/15 min	1200 °C/15 min
CSW40	32 ± 14 (0.11)	116 ± 50 (0.81)	163 ± 54
CSW65	–	104 ± 44	163 ± 54
CSW80	17 ± 9 (0.29)	77 ± 35 (0.89)	197 ± 88
Two-step annealing		CSW65	CSW80
1200 °C/2 min + 800 °C/15 min		106 ± 40 (0.91)	95 ± 35

It can be seen from orientation maps shown above, that [110] texture vanishes with recrystallization. However, the resulting texture after annealing is not completely random. As shown on IPFs on Fig. 5.37, annealing of sample CSW80 gives rise to a weak texture of approximate orientation of [311] in the axial direction. The two component texture in sample annealed at 1000 °C is caused mainly by only partial recrystallization with strong texture of small non recrystallized part.

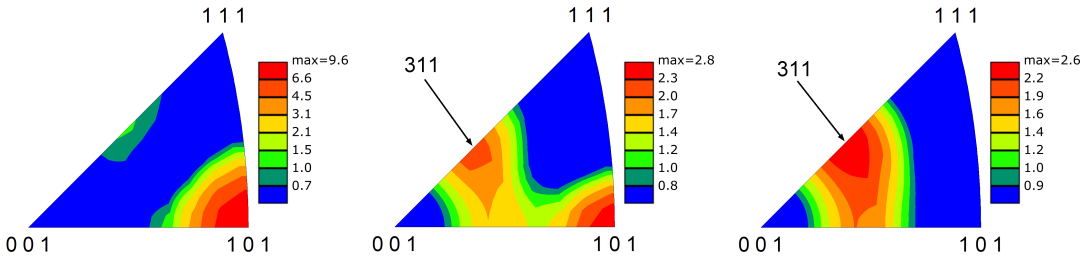

Figure 5.37: IPF's of samples CSW80 after annealing at a) 800 °C, b) 1000 °C and c) 1200 °C.

5.5.3 Cold-swaging series 2

Three rods were cold-swaged at COMTES FHT, a.s., from initial diameter of 15 mm to 8 mm (area reduction 72% - CSW72), 7 mm (area reduction 78% - CSW78) and 6.4 mm (area reduction 82% - CSW82). Close inspection of the cross-sections by SEM proved that any porosity was completely removed by cold-swaging. However, the imposed deformation (deformaion bands) is too high for

observations in SEM using BSE. Due to channeling contrast, not much information could be obtained. Even EBSD measurements have poor quality, so only CSW72 condition was examined by EBSD mapping of 1×1 mm area with step size 1 µm. Overall poor image quality (IQ) and confidence index (CI) of the obtained EBSD scan reflect the homogeneous distribution of deformation in the material. IPF map of CSW72 with IQ as the grayscale is shown in Fig. 5.38a (map with CI-based grayscale is useless for reliable visualization). The majority of the image is very dark due to low IQ, indicating highly deformed structure. Some of the grains in the center of the image have higher image quality, but still, they contain many deformation bands (dark lines).

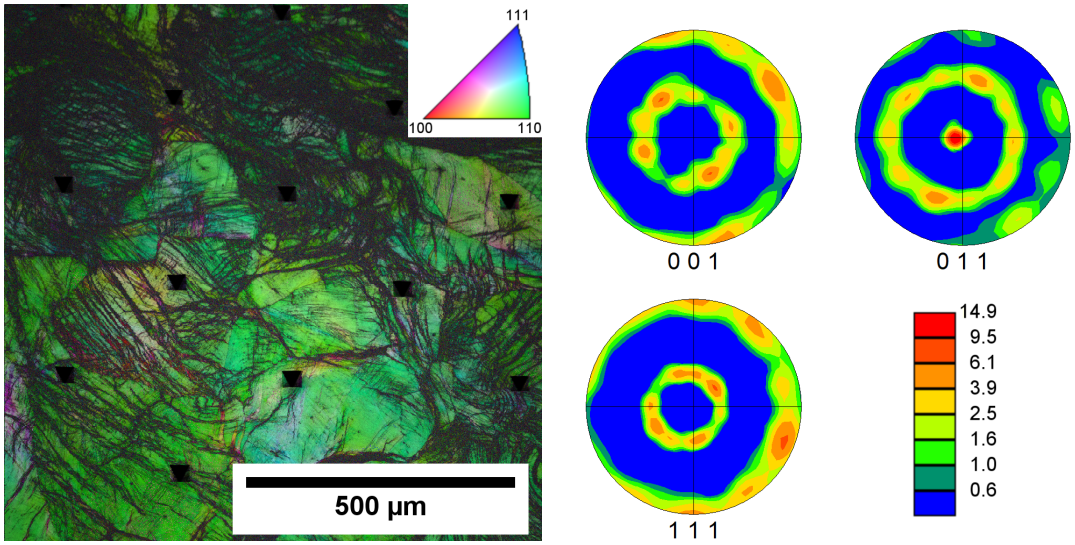

(a) (b)

Figure 5.38: a) IPF map of CSW72 with IQ used as a grayscale, b) PFs of CSW72.

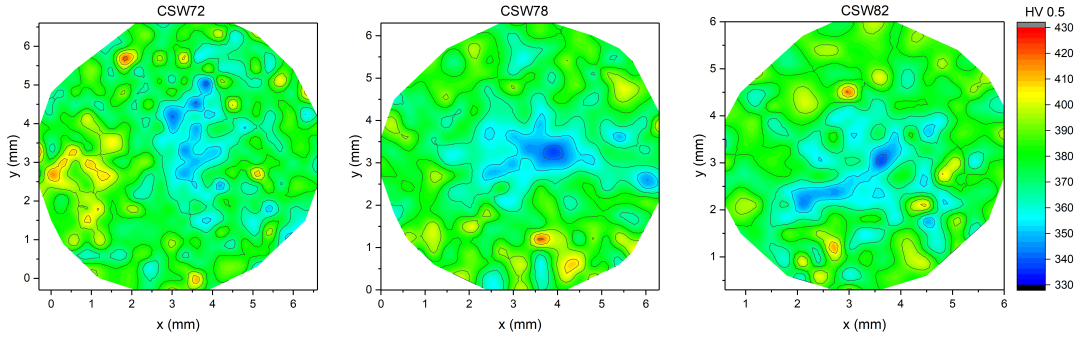

(a) (b) (c)

Figure 5.39: Microhardness maps of cold-swaged rods a) CSW72, b) CSW78, c) CSW82.

The green color prevails in the whole image and as shown in pole figures (PFs) in Fig 4.6.8 b), the [110] texture is present, as expected from previous experiments. There is one significant difference from the texture in cold-swaged rods from series 1 and it is the rotational symmetry. The samples from series

2 were rotated during the cold-swaging and resulting in this symmetry. Due to this symmetry, the dislocation slip (and bands formation) occurs in much larger fraction of grains than in the previous case of cold-swaging without rotation. The main reason is that Schmidt factor of individual grains was changing with each rod orientation change. The maximum texture index is lower than that in Fig. 5.31 for CSW80 sample, mainly because of the distribution with rotational symmetry, but also because the area reduction was slightly lower.

Microhardness maps were measured in the cross-section, as in the previous set of cold-swaged rods. The maps are shown in Fig. 5.39. While most of the cross section has homogeneous microhardness of approx. 380 HV for all three conditions, in the central parts, the microhardness remains at values typical for non-deformed material. This result is completely inverse to that from previous set of cold-swaged rods, where the central part was the hardest. It is thus possible, that rotation of rods during cold swaging has an impact also on the location of less deformed areas (edge for non-rotating and center for rotating rod while cold swaging).

5.5.4 Cold-swaging series 2 + recrystallization annealing

Two rods from series (CSW72 and CSW82) two were annealed at various conditions (temperature and time) in a single-step. Produced conditions are summarized in Table 3.3.

In contrast to series 1, all conditions prepared by annealing of rods cold-swaged in COMTES FHT, a.s., were fully recrystallized, even those with annealing temperature 1000 °C. This, is caused by much more homogeneous distribution of deformation (slip bands) inside all grains. EBSD measurements were taken from all the conditions with scan size of 3 mm×1 mm and various step size, chosen according to the fineness of the measured grain structure.

Table 5.7 summarizes area-fraction based average grain sizes. All conditions were fully recrystallized even after the shortest time of annealing. Therefore prolonging the annealing leads to grain growth. The smallest grain size is achieved in condition cold swaged to 82% of area reduction and annealed at 1000 °C for 5 min.

IPF map of this condition is shown in Fig. 5.40. There is an area in the left part of the image, where the grains with original [110] orientation are separated by only low-angle GBs. These grains were created by recovery process, namely by the formation of dislocation walls inside the grain. The most probable reason for this behavior is that this area is in the center of the rod cross-section where there

Table 5.7: Grain sizes of conditions from annealing of series 2 of cold-swaged rods.

Average grain size (µm)		Annealing temperature		
CSW condition	Anneal. time (min)	1000 °C	1100 °C	1200 °C
CSW72	2	–	64 ± 24	98 ± 37
	5	61 ± 37	96 ± 41	128 ± 50
	15	75 ± 31	113 ± 38	–
CSW82	5	45 ± 21	–	120 ± 44

was less deformation than in other parts (as seen from microhardness maps). Thus, the driving force for nucleation of new grains was not high enough and discontinuous recrystallization did not occur.

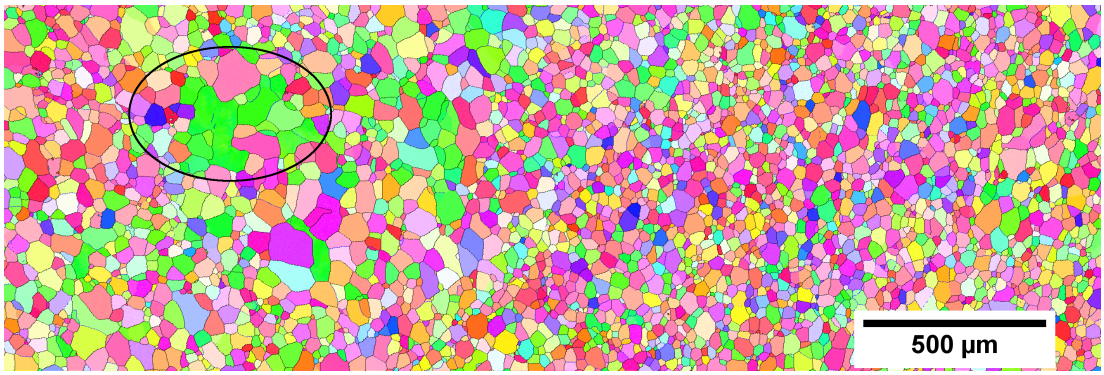

Figure 5.40: IPF map of CSW82 + 1000 °C/5 min annealed condition. Encircled area is has undergone recovery.

Similar recovered area was found in sample annealed at the same conditions but with area reduction only 72% (not shown). On the other hand, all other conditions did not contain such areas. As a result, the smallest homogeneously distributed grain size can be achieved by annealing at 1000 °C for 15 min or at 1100 °C for 2 min. IPF maps of both conditions are shown in Fig. 5.41 for the CSW72 rod. The weak texture [311] was found in all measured samples, sometimes mixed with initial [110] texture, when the continuous recrystallization took part (not shown, texture is similar to that in Fig. 5.37c). The cause of the [311] annealing texture is yet unknown. It could be probably connected to initial [110] texture and dislocation type present in the material. For this research, transmission electron microscopy should be employed to determine the dislocations Burgers vector and slip system. This research goes, however, beyond the scope of this thesis.

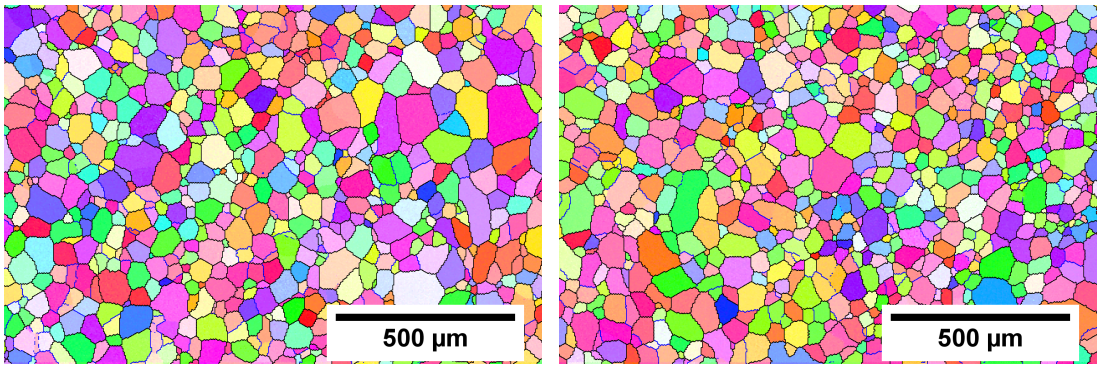

(a) (b)

Figure 5.41: IPF map of CSW72 rod, recrystallized at a) 1000 °C/15 min, b) 1100 °C/2 min.

5.5.5 Summary

Several conditions of the TNTZO alloy subjected to cold-swaging were studied in this section.

First important observation is that the TNTZO alloy can be cold-swaged until AR of 82% even though it contains the high amount of oxygen (0.7%). The achieved AR evidence the high formability even at RT.

It was shown, that it is important, whether the rods are rotated during cold-swaging.

When cold-swaging without rotation of the rod, the amount of macroscopic deformation (i.e. area reduction) significantly affects the homogeniety of deformation distribution in the microscale. Especially with lower area reductions, some grains do not undergo significant plastic deformation by dislocation slip, because of their low Schmidt factor, corresponding to directions of applied force. This effect can be ovecame by rotating the rod in the CSW machine during the process. The rotation leads to homogeneous distribution of deformation bands in the material.

Pores from casting or cracks were not found in any condition with area reduction above 72%. Cold-swaging also significantly affects the microhardness, but its distribution in the cross section is not homogeneous. The CSW without rotation produces rods with a maximum microhardness in the center of the cross-section. On the other hand with rotating the rod during CSW, the microhardness in the center exhibits a minimum, contrary to the CSW without the rotation. The reason for this behaviour is unknown, but could be connected to different propagation of applied stresses during the CSW with or without rotation.

Recrystallization annealing was found to be effective at temperatures exceeding 1000 °C, where complete or nearly complete recrystallization was achieved. In the series 1 of cold-swaged samples, grain size of approx. 100 µm was achieved by single step annealing at 1000 °C for 15 min and by two-step annealing at 1200 °C/2 min + 800 °C/15 min. During the two-step annealing, the new grains are nucleated at the high temperature of 1200 °C and then stabilized at 800 °C.

Recrystallization annealing of series 2 of CSW rods proved that the deformation is indeed more homogeneous than that of rods from series 1. In series 1, large grains with initial [110] texture were present after annealing as the deformation stored inside them was not high enough for recrystallization. On the other hand, in series 2, the microstructure was fully refined and none of the grains had the original size of 1 mm - 2 mm. The smallest grain size of 45 ± 21 µm was achieved in rod with area reduction of 82% annealed at 1000 °C/5 min. However, this condition contains central areas that have localy larger grains and the original [110] texture that formed by recovery without apparent recrystallization. Prolonging the annealing at 1000 °C to 15 min leads to much more homogeneous grain size of 75 ± 31 µm even at rod cold-swaged only to 72%.

Typical strong [110] texture in the axial direction is formed upon cold-swaging. However, it is not preserved during recrystallization and only weak texture approx. [311] direction in the axial direction of rods is formed upon annealing.

Combination of cold-swaging and recrystallization annealing is an effective way of refining the microstructure of TNTZO. The grain size can be reduced by nearly two orders of magnitude while the exposure to high temperatures is very short (15 min). Limited annealing time is favorable with respect to surface

oxidation and cracking propagation.

5.6 Discussion

TM treatment behaviour of TNTZO alloy was studied in several conditions. Let us now summarize results from the previous sections.

For preliminary characterization of alloy behaviour, hot compression tests were conducted (cf. section 5.2). It was found that two mechanisms of plastic deformation can be present. Deformation of material near GBs with progressive recovery inside the grains is found when testing at rather high temperatures and strain rates (1000 °C and $\dot{\varepsilon} = 1\ s^{-1}$). This behaviour was found also in other β-Ti alloys, when deforming at relatively high temperatures (with respect to melting temperature [75, 56].

On the other hand, completely different behaviour is found during deformation at lower temperatures and strain rates. During the deformation, dislocation bands are formed, that pass through entire grain structure. The dislocations are arranged into the low-angle GBs. Similar deformation bands were found in cold-swaged β-Ti alloys [76, 77] and were attributed to "giant faults" caused by dislocation-free plastic deformation (pure shear). It was later proved that dislocation slip is active in this type of alloys instead of formation of the "giant faults" [78].

It was further shown by double-hit tests, that microstructure deformed by the low temperature mechanism can be recrystallized at least continuously.

Two traditional ways of forming metals were employed to process the cast ingot of TNTZO: die-forging and hot rolling. Significant improvement of structural and mechanical properties was achieved by both methods. Hot deformation however, is not very suitable for TNTZO alloy as it results in excessive oxidation and surface cracking.

The die-forging and hot rolling results also show, that solely removing the porosity from cast condition does not improve the fatigue performance. Fatigue limit of 400 MPa is achieved only for the most deformed hot rolled rod with diameter of 20 mm. Other conditions show values similar to the cast condition and the fatigue limit well below 350 MPa. Hot rolling produces much more homogeneous material than die-forging, as shown by microstructural observations, tensile testing and fatigue testing.

Results from both methods suggest that TNTZO alloy can recrystallize by annealing of previously deformed material at temperatures of approx. 1000 °C. Therefore, the last investigated type of processing was cold-swaging followed by recrystallization annealing.

Despite the high oxygen content, successful cold-swaging could be performed up to AR of 80 % because of pure β phase (such high oxygen content leads to embrittlement in α phase).

By recrystallization annealing of cold-swaged material, significant refinement of microstructure and removing of porosity is achieved. The short contact with high temperatures limits oxidation to a minimum. Resulting microstructures look very promising.

It is preferable to use lower amounts of area reduction. For the implant production the desired diameter of rod is 35 mm. Therefore, only 64 mm diameter

of cast ingot is needed for 70% AR, whereas for 80% of AR, the cast ingot diameter needs to be 80 mm. The price of larger ingot is much higher due to manufacturing difficulties.

Due to this reasons, it would be preferable to use area reduction of 72% and annealing at 1000 °C for 15 min for material production. The positive impact of the refined grain structure on tensile and fatigue properties needs to be further verified. However, produced homogeneous equiaxed microstructure with grain size of 75 ± 31 µm seems to be very promising, especially in comparison with results from hot rolling.

The following procedure is proposed for the implant production:

- Casting of initial rod with appropriate diameter.
- Homogenization at suitable temperature (at least 1300 °C [79])
- Cold swaging to 70% of area reduction.
- Implant semi-product die-forging with previous heating to at least 1000 °C - 1100 °C for 15 min (to recrystallize the structure).

Finishing procedures such as machining of final shape and polishing are well established from production of Ti-6Al-4V implants.

6. Results and discussion - New alloys with lower β phase stability

We will now focus on a different topic that is development of new alloys. The motivation and strategy of development were described in chapter 1, especially in the last subsection 1.4.4. The alloy preparation was described in section 3.4. The produced alloys were designed on basis of their e/a ratio. The content of Nb is gradually decreased both in alloys with the original content of Ta and also in alloys that do not contain the Ta. The value of e/a=4.24, reported to decrease the YM to a minimum, is achieved in both least stabilized alloys, Ti-26Nb-6Ta-7Zr-0.7O and Ti-29Nb-7Zr-0.7O.

We will now present some basic microstructural observations and mechanical characterization.

6.1 Scanning electron microscopy

Fig. 6.1 shows microstructure of TNTZO-35-6-7 (Ti-35Nb-6Ta-7Zr-0.7O) after annealing at 850 °C/1h (in Ar filled quartz tubes with water quenching after the annealing). Large β grains are present in the material with the size of the order of 1 mm. The Z-contrast variations indicate that there is a chemical inhomogeneity similar to that present in the cast ingot of TNTZO-35-6-7; cf. section 5.1.1. In both conditions, the inhomogenities are present definitely due to the lack of proper homogenization procedure, as 1000 °C/6 h was not enough and original 1400 °C/2 h annealing in vacuum should have been performed instead. Using higher magnification, the α phase was found on the majority of GBs. An example of such GB decorated with α particles is on Fig. 6.1b. Similar structure and GB α was found in all produced alloys. The least stabilized alloy, TNTZO-26-6-7 (Ti-26Nb-6Ta-7Zr-0.7O), contained the α phase also in the Ti enriched areas of inhomogeneities, as shown in 6.2a (darker areas in the Z-contrast are Ti enriched).

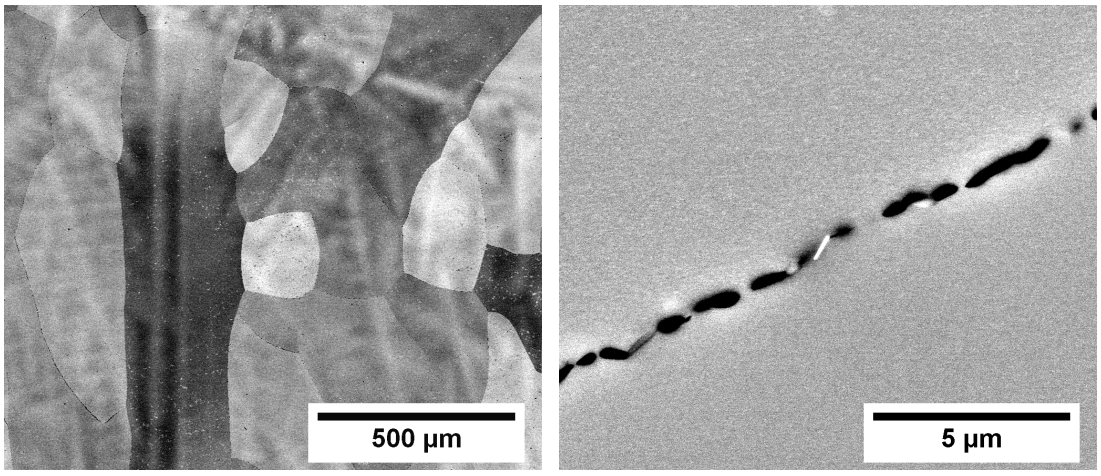

(a) (b)

Figure 6.1: TNTZO-35-6-7 a) overview, b) grain boundary α phase.

Since the annealing at 850 °C/1 h was insufficient to dissolve the GB α phase, samples were annealed at 1000 °C/15 min in air and water quenched. This was finally a successful solution treatment (ST) procedure and even the GB α phase dissolved. However, there were still tiny flat particles around the GBs observed by Z-contrast as in the middle of Fig. 6.1b. These particles were present in all alloys. Fig. 6.2b shows a BSE image of alloy TNTZO-32-6-7. The image contains bright rectangular plate-like particles. These particles must contain some heavy elements (due to their bright contrast even at low voltages). The chemical composition of these particles was inspected by EDX measurements.

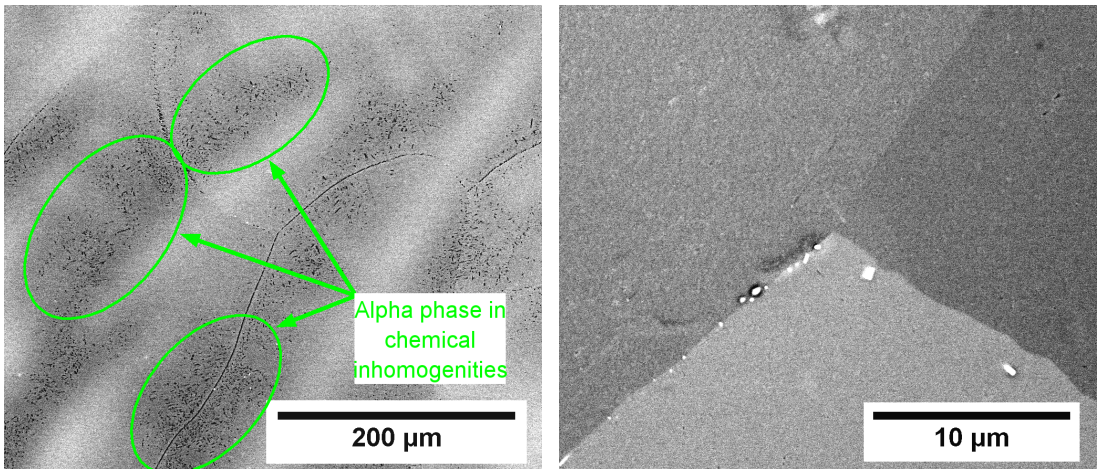

(a) (b)

Figure 6.2: a) α phase precipitated on inhomogenities in TNTZO-26-6-7, b) Heavy elements containing particles on GBs in TNTZO-32-6-7.

6.2 EDX measurements

Measurements by EDX were done both to identify the composition of particles found on GBs and to check the nominal composition of the alloys. Accelerating voltage of 30 kV was employed to ensure the excitation of as many of the energy levels as possible (while resigning on the spatial resolution) to determine the qualitative chemical composition.

Point measurement by EDX was conducted at the unknown particles. The resulting spectrum is shown in Fig. 6.3 of a particle in alloy TNZO-35-7. It was clearly proved that the GB particles with high BSE Z-contrast signal in all studied alloys contain thorium. The thorium particles were most likely introduced into the alloys during their production. First possible reason is the burn-off of tungsten electrode doped by ThO_2 used for electric arc melting. Another possible reason is contamination of initial material by powder of ThO_2, since ThO_2 is used for production of nuclear fuels [80] (UJP, a.s., where the alloys were produced is mainly conducting a research on nuclear fuels). From EDX measurements it is not possible to decide, whether the particles contain only Th the particles are ThO_2, because the Kα peak of oxygen is very close to the Lα peak of titanium and thus not visible.

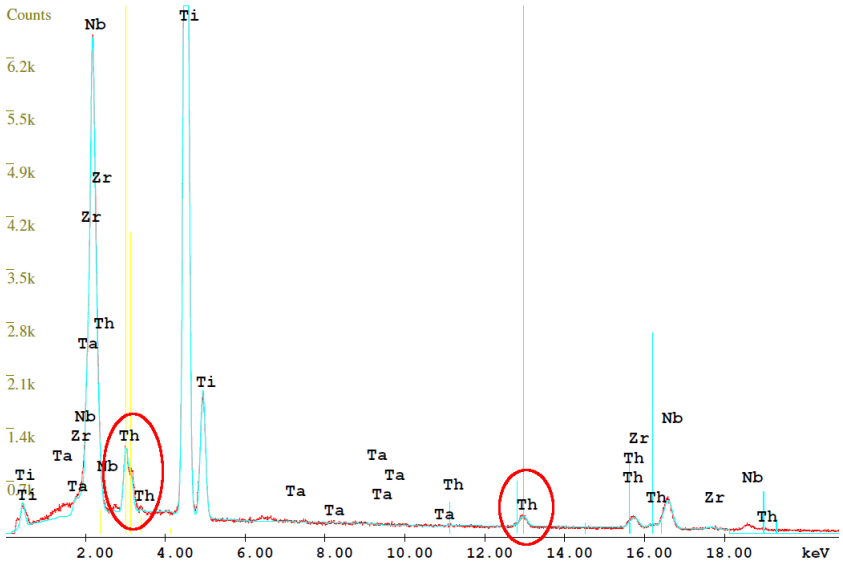

Figure 6.3: EDX spectrum of GB particle in TNZO-35-7. Th peaks are encircled.

The compositions of all produced alloys as determined by EDX measured in large area scans are shown in Table 6.1. Note that Th content determined by EDX is ambiguous, in contrast to precise production of the alloys. Zr content fits the nominal value quite well, but measured Ta content is higher by approx. 4 wt.% and Nb value is 4% - 6% lower.

This difference of measured and nominal composition is probably caused by some systematic error in the measurement or the peak fitting algorithm that cannot separate two peaks correctly or whether the EDX detector sensitivity is poor in the high-energy range, where the peaks of Ta are mainly located. Similar problems were encountered also during measurements of composition of the cast ingot [63], but the producer of the ingot afirmed that the composition was very close to a nominal composition by a very precise method called Inductively coupled plasma atomic emission spectroscopy. Therefore, EDX measurements should be understood only as semi-qualitative – the elements are determined correctly, the compositions are not.

If we look only to relative compositional changes, there is correctly missing Ta in the samples denoted TNZO and Nb content is also changing in a relatively correct sense.

Table 6.1: Composition of the alloys measured by EDX.

Alloy	Ti (%)	Nb (%)	Ta (%)	Zr (%)	Th (%)
TNTZO-35-6-7	50. 6	29.8	6.8	10.3	2.5
TNTZO-32-6-7	52. 7	26.2	6.5	9.2	5.5
TNTZO-29-6-7	58.2	24.9	6.6	10.3	0.0
TNTZO-26-6-7	60.9	22.3	6.5	10.3	0.0
TNZO-35-7	59.4	31.5	6.9	0.0	2.2
TNZO-35-7-a	59.0	31.3	6.9	0.0	2.8
TNZO-29-7	67.0	26.1	6.9	0.0	0.0

6.3 Microhardness measurements

Table 6.2 summarizes microhardness measurements of the alloys after ST at 1000 °C/15 min. Values for alloys with lower/no oxygen content (TNTZ-0.4O and TNTZ) are added for comparison together with the TNTZO-35-6-7 from previous research [41] - for this purpose being denoted as TNTZ-0.7O. It is clear that while addition of small oxygen content of the order of tenths of % can double the microhardness, reducing of theβ stabilizing elements content has no measurable effect. Even after reducing both Nb and Ta content by 6 % (as in the alloy TNZO-29-7), the microhardness remains the same as microhardness of TNTZO-35-6-7. This result also proves that oxygen strengthening is not connected to any interaction with neither Nb nor Ta. The interstitial solution hardening effect of oxygen is so strong that it can compensate even total of 12 wt. % of missing substitutional strengthening elements.

Table 6.2: Microhardness values of produced alloys.

Alloy label	HV 0.5	Alloy label	HV 0.5
TNTZ [41]	164	TNTZO-29-6-7	328 ± 5
TNTZ-0.4O [41]	270	TNTZO-26-6-7	333 ± 5
TNTZ-0.7O [41]	335	TNZO-35-7	337 ± 4
TNTZO-35-6-7	333 ± 5	TNZO-35-7-a	320 ± 6
TNTZO-32-6-7	328 ± 5	TNZO-29-7	328 ± 5

6.4 Tensile testing

One sample in ST 1000 °C/15 min condition was tested from each alloy. The flow curves are shown in Fig. 6.4a.

None of the alloys exhibits double yielding, that is an indicator of pseudoelastic properties (shape memory, super elasticity). Therefore, none of the developed alloys undergoes the $\beta \leftrightarrow \alpha$" martensitic transformation during straining.

All curves exhibit a sharp yield point as expected from microhardness measurements (strengthening by oxygen is present in all alloys). The yield points remain high for all tested alloys (880 MPa – 1040 MPa). It is interesting, that two alloys with the lowest amount of β stabilizing elements achieve the highest yield strength. Whether this is caused by some strengthening particles (ω, α") is an open question and SEM observations of microstructure in the active zones were conducted (see the next section).

The true stress - true strain curves of individual alloys are shown in Fig. 6.4b. Three types of plastic behaviorare observed. Firstly, in the alloy TNTZO-32-6-7, significant deformation strengthening occurs and after achieving the ultimate tensile strength, the necking occurs and the sample fails by a ductile fracture. The achieved elongation is 14%. The second type of behavior is seen in 4 other alloys, that also undergo deformation strengthening, but brittle fracture occurs between 6% and 9% of true strain. This behaviour was explaind by SEM observations, in the next section.

The third group comprises of two least stabilized alloys TNTZO-26-6-7 and TNZO-29-7. Despite having the highest yield point, no deformation strengthening

is obtained. After the yield point, only softening was observed and fracture occurs after a short elongation. Ductility was not probably affected by GB ThO_2 particles, since they were present in all alloys but ductility differed in individual alloys. Particles of some other phases, that could originate during straining may negatively influence the ductility.

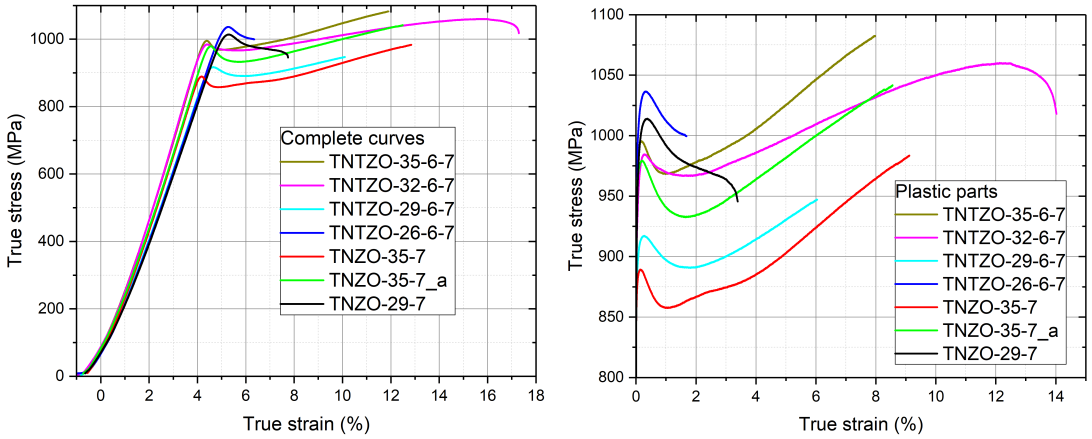

(a) (b)

Figure 6.4: Flow curves from produced alloys, a) Complete curves, b) Plastic parts.

Summary of measured tensile properties is shown in Table 6.3 together with alloys TNTZ, TNTZ-0.4O and TNTZ-0.7O. The apparent difference in the yield strength of TNZO-35-7 and TNZO-35-7-a could be caused by possible contamination by tungsten that could have an impact on solution strengthening although the content was under the detection limit of EDX. It should be further examined, what causes the high strength and low ductility of the two least stabilized alloys. Note that alloys from original research were forged before ST, therefore achieved mechanical properties, especially elongation, were improved as compared to the as-cast condition.

Table 6.3: Tensile properties of produced and reference alloys [41]. Def. str. = deformation strengthening

Alloy label	YS (MPa)	UTS (MPa)	TPTS (%)	Def. str.
TNTZ [41]	447	545	16	YES
TNTZ-0.4O [41]	860	903	11	YES
TNTZ-0.7O [41]	1017	1217	21	YES
TNTZO-35-6-7	995	1082	8.0	YES
TNTZO-32-6-7	984	1060	14.0	YES
TNTZO-29-6-7	917	947	6.0	YES
TNTZO-26-6-7	1036	–	1.7	NO
TNZO-35-7	889	983	9.1	YES
TNZO-35-7-a	979	1041	8.6	YES
TNZO-29-7	1014	–	3.4	NO

6.5 SEM observations of fractured tensile samples

Inspection of longitudinal section through deformed samples by SEM provides the explanation of high ductility of sample from alloy TNTZO-32-6-7. Fig. 6.5 shows active zones near fracture surface of a) TNTZO-35-6-7 and b) TNTZO-32-6-7. Both samples contain elongated grains that have apparent deformation bands visible. However, in TNTZO-35-6-7 the grains are elongated in the direction of incident 45° to the tensile direction, while in TNTZO-32-6-7, the grains are oriented more parallel to the tensile direction. This elongation can affect the ductility and since the preferred crystal orientation of growing grains during solidification is [100] (see subsection 5.1.2), the different active slip systems may be activated causing enhanced ductility.

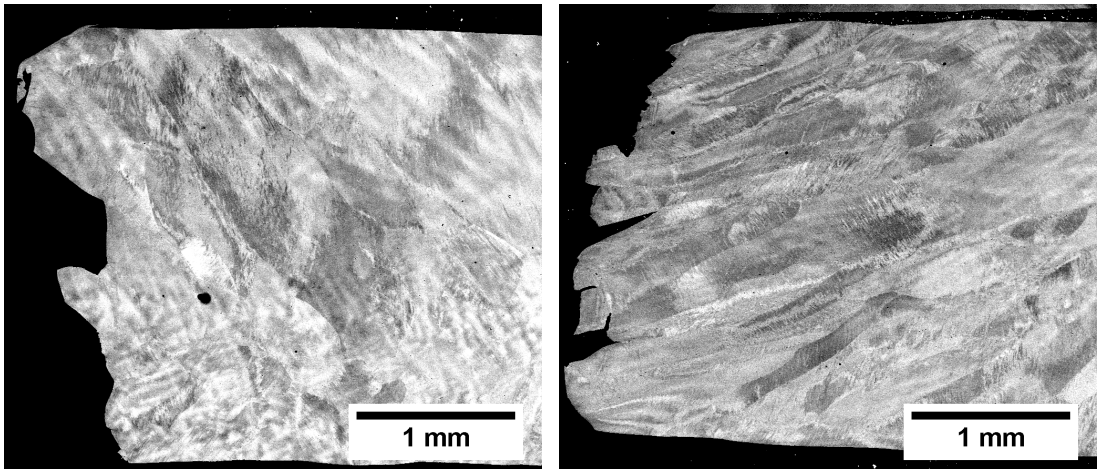

(a) (b)

Figure 6.5: Active zones of tensile samples near fracture surface: a) TNTZO-35-6-7, b) TNTZO-32-6-7.

Fig. 6.6 shows active zones of tensile samples from a) TNTZO-26-6-7, b) TNZO-29-7. The former image is similar to that of TNTZO-35-6-7 that has undergone a deformation strengthening. The latter image is specific in the grain orientation. The grains are rather perpendicular to the tensile direction, although it is questionable whether this can negatively influence the ductility, especially in contrast to TNTZO-26-6-7, for which the ductility was even lower but grain structure is similar to TNTZO-35-6-7.

Even with higher magnification (not shown), no reason for low ductility was found in the individual samples. Perhaps TEM observations could provide more detail (brittleness caused by omega phase?). It is worth to note that inspecting the tensile samples active zones, no stress induced α" phase was found consistently with macroscopic mechanical behavior (no double yielding phenomenon). There is also possibility that the entire alloys that showed low ductility are formed only by α" phase. This will require further research, preferably by x-ray diffraction measurements.

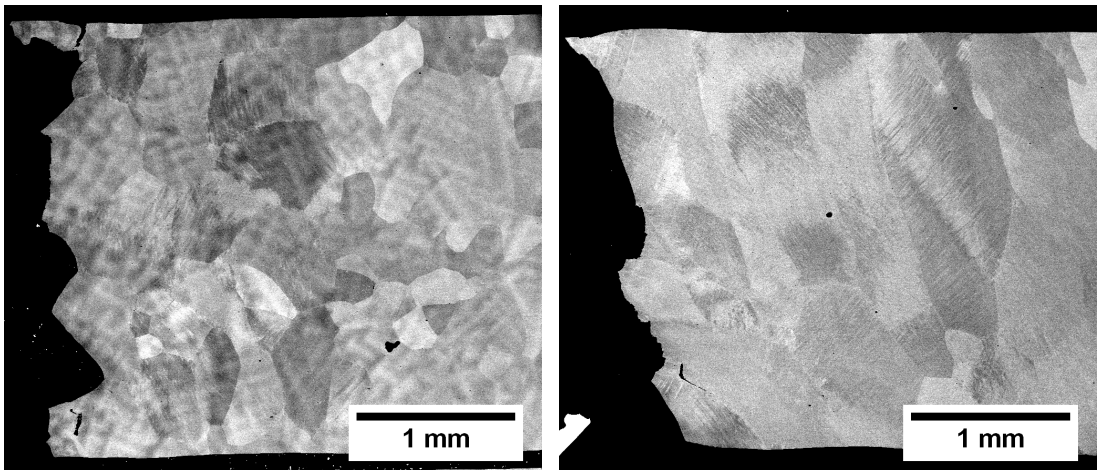

(a) (b)

Figure 6.6: Active zone of tensile samples near fracture surface: a) TNTZO-26-6-7, b) TNZO-29-7.

6.6 Young's modulus measurements

In order to complete the characterization of newly developed alloys, YM was measured by two methods: ARS and RUS. The results are shown in table 6.4.

Table 6.4: Young's modulus of developed alloys measured by ARS and RUS compared to TNTZ and TNTZ-0.4O.

Alloy label	YM (GPa) - ARS	YM (GPa) - RUS
TNTZ [41]	–	63
TNTZ-0.4O [41]	–	81
TNTZ-0.7O [41]	–	80
TNTZO-35-6-7	83	76
TNTZO-32-6-7	73	72
TNTZO-29-6-7	72	66
TNTZO-26-6-7	68	64
TNZO-35-7	72	71
TNZO-35-7-a	72	63
TNZO-29-7	64	59

It is obvious from both methods that YM indeed drops with lowering the β stabilizing element content. There is some disagreement in the results of both methods, namely RUS gives lower values of YM than ARS. The reason can be the fact that samples for RUS have their thinnest direction parallel to axial direction of rods used for ARS. Therefore, the resonance direction of RUS was perpendicular to that of ARS (flexural mode) and since the grains could have a preferential orientation (e.g. direction <100> parallel with rods length), the texture may have lowered the measured YM in the RUS samples. On the other hand, the samples for RUS were so small, that with average grain size of 1 mm, only approx. 24 grains were present in the sample and thus the value of YM is only local. ARS values are therefore measured more reliably, as the samples were

large enough compared to the grain size.

The lowest YM achieved by lowering Nb and Ta content is 64 GPa (ARS value) or 59 GPa (RUS value) in TNZO-29-7 alloy. This value is even lower than in the original alloy Ti-35Nb-6Ta-7Zr without oxygen.

Fig. 6.7 shows, how the YM (measured by ARS) changes with different Nb content, for all alloys, shown in Table 6.4. Data from the original research of TNTZ, TNTZ-0.4O and TNTZ-0.7O are also included (only RUS values are available and shown). We can clearly see that YM value of the original, oxygen-free alloy, can be reached by combined reduction of both Nb and Ta content in the TNZO-29-7 alloy.

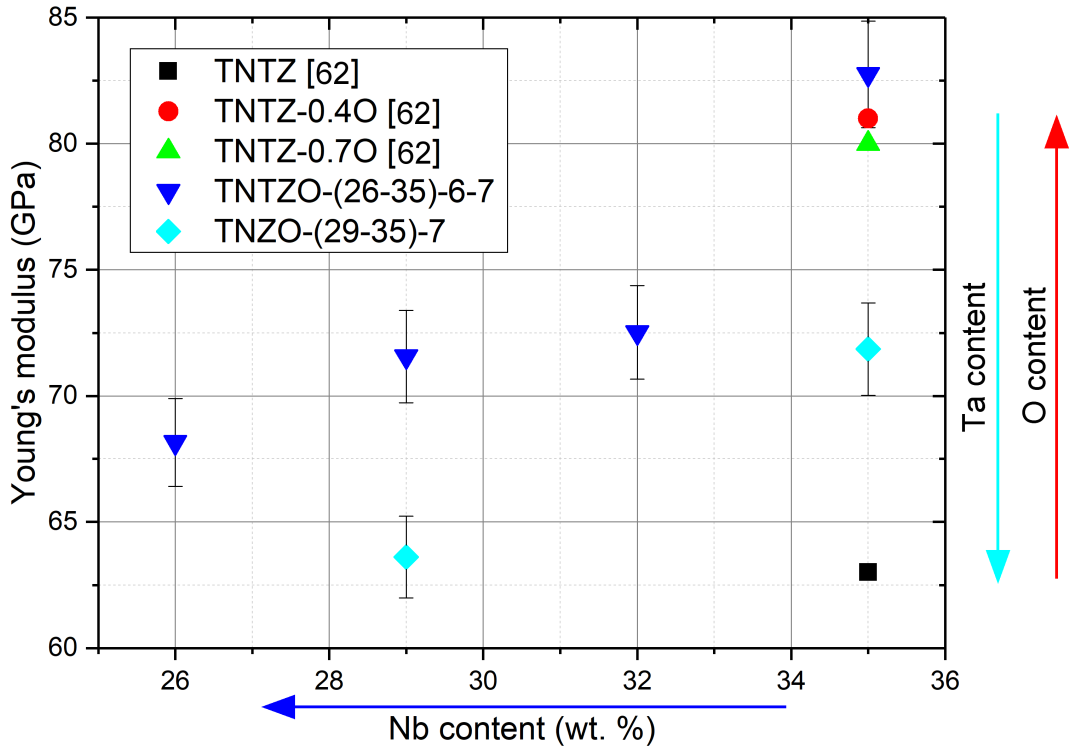

Figure 6.7: YM dependence on Nb content for various alloys. Effect of Nb, Ta and O content on YM is marked by arrows.

6.7 Discussion

In order to compare the achieved mechanical properties of ST alloys with other authors, two graphs were made that are shown in Fig. 6.8a and 6.8b. The first graph shows the dependence of YM vs. microhardness and the second one YM vs. YS. Although in most studies, YM and microhardness have a correlation, this is not true for alloys studied in this chapter. While maintaining the same microhardness caused by interstitial oxygen, YM drops significantly to values comparable to alloys that have almost half microhardness (e.g. the oxygen free TNTZ alloy). In the graph of YM vs. yield strength, the effect is not so obvious, but still, the alloy TNZO-29-7 reaches the sweet spot of lower right part of the graph (high strength over 800 MPa needed for hip implant construction and low

YM). Nearest alloys with YM lower than TNZO-29-7 have the yield strength around the banchmark 800 MPa, thus 200 MPa lower than TNZO-29-7.

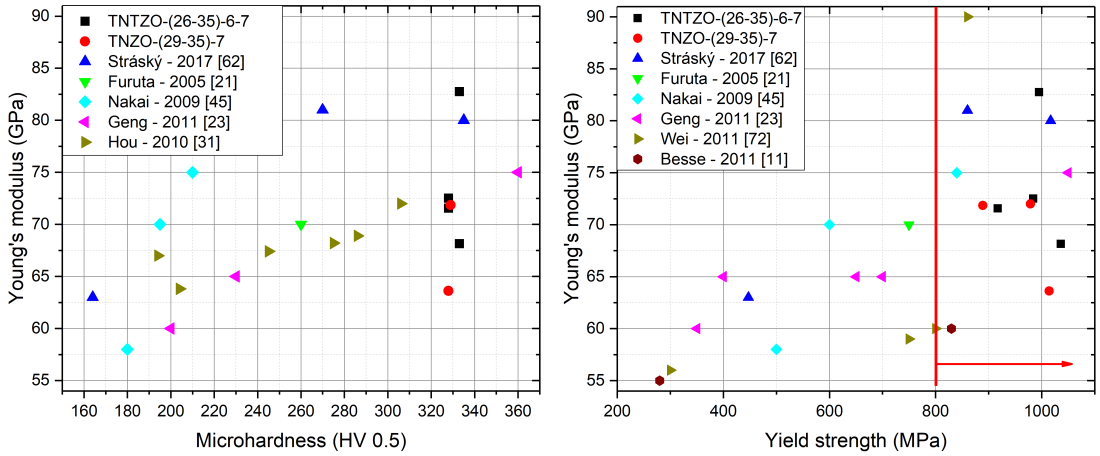

(a) (b)

Figure 6.8: Comparison of achieved mechanical properties in ST condition with other authors: a) YM vs. microhardness, b) YM vs. yield strength.

It was found that interstitial oxygen strengthening effect is not affected even by reduction of β stabilizing alloying elements by 12%. The most probable reason is that the oxygen interstitials are pinning the dislocations by Cottrel atmosphere formation the same way as the carbon interstitials are pinning dislocations in α-Fe, i.e. bcc iron [50]. The same explanation was used for the alloy with original content of Nb and Ta [41, 27, 81]. Since the Zr content was not changed in produced alloys, it is still possible that the strengthening effect of oxygen is connected to nanoclustering of O around Zr atoms [52]. Further work, such as producing Zr-free alloys, is proposed.

The dislocation pinning effect of 0.7% of oxygen is of major importance as in alloys containing only 0.5% O, the sharp yield point was not observed and the strength was significantly affected by only small Nb concentration variations, although these alloys were in severly cold-seaged condition [44].

Thermomechanical processing would provide further enhancement of the strength values, as shown in chapter 5.1 of this thesis.

The stability with respect to $\beta \rightarrow \alpha''$ martensitic transformation was increased by oxygen content (higher e/a ratio) [32], which caused the rise of the Young's modulus [41]. The e/a ratio was decreased by reducing the Nb and Ta content in the newly developed alloys as both the Nb and Ta contain 5 valence electrons whereas Ti has only 4 valence electrons.

Reducing the stability of β phase (i.e. e/a ratio) has indeed resulted in a decrease of Young's modulus as shown in the figures above. Therefore the alloy design described in section 1.4.4 was proven successful.

To summarize achieved results from this chapter:

- Produced alloys contain pure β phase even though its stability is suppressed by Nb and Ta content reduction.
- Microhardness is not changed despite lower of Nb and Ta content.

- Strength of produced alloys varies in the range of 900 MPa – 1050 MPa. The least stabilized alloys show significantly decreased ductility. The reason for low ductility is yet to be found.
- Values of Young's modulus decrease with decreasing e/a ratio caused by lower Nb and Ta content. Low values of YM similar to the oxygen-free TNTZ alloy are achieved.
- Comparison with various studies indicate that produced alloys have the most suitable properties for joint implant production.

Conclusion

This thesis was devoted to two topics. Thermomechanical treatment of biomedical β-Ti alloy Ti-35Nb-6Ta-7Zr-0.7O (TNTZO) and the design and characterization of new alloys with enhanced mechanical properties. The following conclusion can be drawn from this investigation.

- TNTZO alloy was hot deformed at temperatures over 1000 °C by die-forging and hot rolling. Dynamic recovery and limited dynamic recrystallization were identified by EBSD observation.
- Material produced by hot rolling exhibits homogeneous microstructure with no porosity and refined grain structure. Fatigue performance is significantly enhanced when compared to as-cast condition. On the other hand, the achieved fatigue properties are not sufficient for implant material. It was argued, that significant grain refinement is required to improve fatigue performance.
- It was found that material can be rotation cold-swaged up to area reduction of 80%. Several area reductions were produced and characterized.
- Annealing treatment of cold-swaged material resulted in partial or complete recrystallizaion depending on annealing temperature and time. Cold swaging to 70% of area reduction and followed by annealing at 1000 °C/15 min were developed as procedure for complete recrystallization and to achieve grain size below 100 mμ.
- All used thermomechanical treatments were compared and their differences were discussed. The route of preparation of material for implant production was proposed.
- Six new Ti-Nb-Ta-Zr-O alloys with reduced β stabilizing Nb and/or Ta content were produced and characterized.
- All newly designed alloys retain high strength as the interstitial strengthening mechanism of oxygen (pinning the dislocations by oxygen atoms) is independent of Nb and Ta content. At the same time, reduced β phase stability resulted in significantly decreased Young's modulus.
- The combination of high strength and low Young's modulus is unparalleled in comparison with other Ti alloys. Achieved properties are very promising for load-bearing implants manufacturing.

Bibliography

[1] T Brandmuller, A Onnerfors, et al. Eurostat regional yearbook 2011. 2011.

[2] Health at a Glance: Europe - Public Health - European Commission.

[3] H Derar and M Shahinpoor. Recent Patents and Designs on Hip Replacement Prostheses. *The Open Biomedical Engineering Journal*, 9:92–102, March 2015.

[4] Christian Delaunay, Moussa Hamadouche, Julien Girard, and Alain Duhamel. What Are the Causes for Failures of Primary Hip Arthroplasties in France? *Clinical Orthopaedics and Related Research*, 471(12):3863–3869, December 2013.

[5] John P. Paul. Strength requirements for internal and external prostheses. *Journal of Biomechanics*, 32(4):381–393, April 1999.

[6] Catrine Tudor-Locke, Cora L Craig, Yukitoshi Aoyagi, Rhonda C Bell, Karen A Croteau, Ilse De Bourdeaudhuij, Ben Ewald, Andrew W Gardner, Yoshiro Hatano, Lesley D Lutes, Sandra M Matsudo, Farah A Ramirez-Marrero, Laura Q Rogers, David A Rowe, Michael D Schmidt, Mark A Tully, and Steven N Blair. How many steps/day are enough? For older adults and special populations. *The International Journal of Behavioral Nutrition and Physical Activity*, 8:80, July 2011.

[7] Jae-Young Rho, Ting Y. Tsui, and George M. Pharr. Elastic properties of human cortical and trabecular lamellar bone measured by nanoindentation. *Biomaterials*, 18(20):1325–1330, 1997.

[8] Philippe K Zysset, X Edward Guo, C Edward Hoffler, Kristin E Moore, and Steven A Goldstein. Elastic modulus and hardness of cortical and trabecular bone lamellae measured by nanoindentation in the human femur. *Journal of Biomechanics*, 32(10):1005–1012, 1999.

[9] M. G. Joshi, S. G. Advani, F. Miller, and M. H. Santare. Analysis of a femoral hip prosthesis designed to reduce stress shielding. *Journal of Biomechanics*, 33(12):1655–1662, December 2000.

[10] Yuichi Watanabe, Naoto Shiba, Shigeaki Matsuo, Fujio Higuchi, Yoshihiko Tagawa, and Akio Inoue. Biomechanical study of the resurfacing hip arthroplasty: Finite element analysis of the femoral component. *The Journal of Arthroplasty*, 15(4):505–511, June 2000.

[11] D. R. Sumner. Long-term implant fixation and stress-shielding in total hip replacement. *Journal of Biomechanics*, 48(5):797–800, March 2015.

[12] Carlos Oldani and Alejandro Dominguez. Titanium as a Biomaterial for Implants. 2012.

[13] Mitsuo Niinomi. Mechanical biocompatibilities of titanium alloys for biomedical applications. *Journal of the Mechanical Behavior of Biomedical Materials*, 1(1):30–42, January 2008.

[14] H. J. Rack and J. I. Qazi. Titanium alloys for biomedical applications. *Materials Science and Engineering: C*, 26(8):1269–1277, September 2006.

[15] Gerhard Welsch, Rodney Boyer, and E. W. Collings. *Materials Properties Handbook: Titanium Alloys*. ASM International, December 1993. Google-Books-ID: x3rToHWOcD8C.

[16] J. Taylor, S. Keith, L. Cseh, L. Ingerman, L. Chappell, J. Rhoades, and A. Hueber. Toxicological profile for vanadium. *Atlanta, US: Agency for Toxic Substances and Disease Registry*, page 255, 2012.

[17] S. Maya, T. Prakash, Krishna Das Madhu, and Divakar Goli. Multifaceted effects of aluminium in neurodegenerative diseases: A review. *Biomedicine & Pharmacotherapy*, 83(Supplement C):746–754, October 2016.

[18] K. Zaman, A. Zaman, and J. Batcabe. Hematological effects of aluminum on living organisms. *Comparative Biochemistry and Physiology. C, Comparative Pharmacology and Toxicology*, 106(2):285–293, October 1993.

[19] Christoph Leyens and Manfred Peters. *Titanium and titanium alloys*. Wiley Online Library, 2003.

[20] G. Lütjering and J. C. Williams. *Titanium*, volume 2. Springer, 2003.

[21] Paul J. Bania. Beta titanium alloys and their role in the titanium industry. *JOM*, 46(7):16–19, July 1994.

[22] Dipankar Banerjee and J. C. Williams. Perspectives on Titanium Science and Technology. *Acta Materialia*, 61(3):844–879, February 2013.

[23] Yufeng Zheng, Robert EA Williams, Gopal B Viswanathan, William AT Clark, and Hamish L Fraser. Determination of the structure of α-β interfaces in metastable β-ti alloys. *Acta Materialia*, 150:25–39, 2018.

[24] Pavel Zháňal, Petr Harcuba, Michal Hájek, Bohumil Smola, Josef Stráský, Jana Šmilauerová, Jozef Veselý, and Miloš Janeček. Evolution of ω phase during heating of metastable β titanium alloy Ti–15mo. *Journal of Materials Science*, pages 1–9, September 2017.

[25] M. Besse, P. Castany, and T. Gloriant. Mechanisms of deformation in gum metal TNTZ-O and TNTZ titanium alloys: A comparative study on the oxygen influence. *Acta Materialia*, 59(15):5982–5988, September 2011.

[26] W. Elmay, P. Laheurte, A. Eberhardt, B. Bolle, T. Gloriant, E. Patoor, F. Prima, D. Laille, P. Castany, and M. Wary. Stability and elastic properties of Ti-alloys for biomedical application designed with electronic parameters. *EPJ Web of Conferences*, 6:29002, 2010.

[27] F. Geng, M. Niinomi, and M. Nakai. Observation of yielding and strain hardening in a titanium alloy having high oxygen content. *Materials Science and Engineering: A*, 528(16–17):5435–5445, 2011.

[28] Shun Guo, Qingkun Meng, Xinqing Zhao, Qiuming Wei, and Huibin Xu. Design and fabrication of a metastable β-type titanium alloy with ultralow elastic modulus and high strength. *Scientific Reports*, 5, October 2015.

[29] F. Q. Hou, S. J. Li, Y. L. Hao, and R. Yang. Nonlinear elastic deformation behaviour of Ti-30nb-12zr alloys. *Scripta Materialia*, 63(1):54–57, 2010.

[30] Jae Il Kim, Hee Young Kim, Hideki Hosoda, and Shuichi Miyazaki. Shape Memory Behavior of Ti–22nb–(0.5–2.0)O(at%) Biomedical Alloys. *Materials Transactions*, 46(4):852–857, 2005.

[31] Mohamed Abdel-Hady, Hiroki Fuwa, Keita Hinoshita, Haruka Kimura, Yoshifumi Shinzato, and Masahiko Morinaga. Phase stability change with Zr content in β-type Ti–Nb alloys. *Scripta Materialia*, 57(11):1000–1003, December 2007.

[32] Y. L. Hao, S. J. Li, F. Prima, and R. Yang. Controlling reversible martensitic transformation in titanium alloys with high strength and low elastic modulus. *Scripta Materialia*, 67(5):487–490, September 2012.

[33] H. L. Wang, Y. L. Hao, S. Y. He, T. Li, J. M. Cairney, Y. D. Wang, Y. Wang, E. G. Obbard, F. Prima, K. Du, S. J. Li, and R. Yang. Elastically confined martensitic transformation at the nano-scale in a multifunctional titanium alloy. *Acta Materialia*, 135:330–339, August 2017.

[34] M. Tane, Y. Okuda, Y. Todaka, H. Ogi, and A. Nagakubo. Elastic properties of single-crystalline ω phase in titanium. *Acta Materialia*, 61(20):7543–7554, December 2013.

[35] Jitka Nejezchlebová, Michaela Janovská, Hanuš Seiner, Petr Sedlák, Michal Landa, Jana Šmilauerová, Josef Stráský, Petr Harcuba, and Miloš Janeček. The effect of athermal and isothermal ω phase particles on elasticity of β-Ti single crystals. *Acta Materialia*, 110:185–191, May 2016.

[36] E Eisenbarth, D Velten, M Müller, R Thull, and J Breme. Biocompatibility of β-stabilizing elements of titanium alloys. *Biomaterials*, 25(26):5705–5713, November 2004.

[37] D. M. Gordin, R. Ion, C. Vasilescu, S. I. Drob, A. Cimpean, and T. Gloriant. Potentiality of the "Gum Metal" titanium-based alloy for biomedical applications. *Materials Science and Engineering: C*, 44:362–370, November 2014.

[38] Ivana Kopova, Josef Stráskỳ, Petr Harcuba, Michal Landa, Miloš Janeček, and Lucie Bačákova. Newly developed ti–nb–zr–ta–si–fe biomedical beta titanium alloys with increased strength and enhanced biocompatibility. *Materials Science and Engineering: C*, 60:230–238, 2016.

[39] E. Vasilescu, P. Drob, D. Raducanu, V. D. Cojocaru, I. Cinca, D. Iordachescu, R. Ion, M. Popa, and C. Vasilescu. In vitro biocompatibility and corrosion resistance of a new implant titanium base alloy. *Journal of Materials Science: Materials in Medicine*, 21(6):1959–1968, June 2010.

[40] T Ahmed and HJ Rack. Low modulus biocompatible titanium base alloys for medical devices, 1999.

[41] Josef Stráský, Petr Harcuba, Kristína Václavová, Klaudia Horváth, Michal Landa, Ondřej Srba, and Miloš Janeček. Increasing strength of a biomedical Ti-Nb-Ta-Zr alloy by alloying with Fe, Si and O. *Journal of the Mechanical Behavior of Biomedical Materials*, 71:329–336, July 2017.

[42] Josef Stráský. *Optimization of properties of Ti based alloys for biomedical and structural applications*. Doctoral thesis, Charles University in Prague, Prague, 2014.

[43] L. M. Elias, S. G. Schneider, S. Schneider, H. M. Silva, and F. Malvisi. Microstructural and mechanical characterization of biomedical Ti–Nb–Zr(–Ta) alloys. *Materials Science and Engineering: A*, 432(1–2):108–112, September 2006.

[44] Tadahiko Furuta, Shigeru Kuramoto, Junghwan Hwang, Kazuaki Nishino, Takashi Saito, and Mitsuo Niinomi. Mechanical Properties and Phase Stability of Ti-Nb-Ta-Zr-O Alloys. *Materials Transactions*, 48(5):1124–1130, 2007.

[45] Jaroslav Málek, František Hnilica, Jaroslav Veselý, Bohumil Smola, Kamil Kolařík, Jaroslav Fojt, Martin Vlach, and Veronika Kodetová. The effect of Zr on the microstructure and properties of Ti-35nb-XZr alloy. *Materials Science and Engineering: A*, 675:1–10, 2016.

[46] M. Nakai, M. Niinomi, T. Akahori, H. Tsutsumi, and M. Ogawa. Effect of Oxygen Content on Microstructure and Mechanical Properties of Biomedical Ti-29nb-13ta-4.6zr Alloy under Solutionized and Aged Conditions. *Materials Transactions*, 50(12):2716–2720, 2009.

[47] Q. Wei, L. Wang, Y. Fu, J. Qin, W. Lu, and D. Zhang. Influence of oxygen content on microstructure and mechanical properties of Ti–Nb–Ta–Zr alloy. *Materials & Design*, 32(5):2934–2939, 2011.

[48] M. Tane, T. Nakano, S. Kuramoto, M. Niinomi, N. Takesue, and H. Nakajima. ω Transformation in cold-worked Ti–Nb–Ta–Zr–O alloys with low body-centered cubic phase stability and its correlation with their elastic properties. *Acta Materialia*, 61(1):139–150, January 2013.

[49] J. I. Qazi, B. Marquardt, L. F Allard, and H. J. Rack. Phase transformations in Ti–35nb–7zr–5ta–(0.06–0.68)O alloys. *Materials Science and Engineering: C*, 25(3):389–397, May 2005.

[50] A. H. Cottrell and B. A. Bilby. Dislocation theory of yielding and strain ageing of iron. *Proceedings of the Physical Society. Section A*, 62(1):49, 1949.

[51] M. Tane, T. Nakano, S. Kuramoto, M. Hara, M. Niinomi, N. Takesue, T. Yano, and H. Nakajima. Low Young's modulus in Ti–Nb–Ta–Zr–O alloys: Cold working and oxygen effects. *Acta Materialia*, 59(18):6975–6988, 2011.

[52] Naoyuki Nagasako, Ryoji Asahi, Dieter Isheim, David N. Seidman, Shigeru Kuramoto, and Tadahiko Furuta. Microscopic study of gum-metal alloys: A role of trace oxygen for dislocation-free deformation. *Acta Materialia*, 105:347–354, 2016.

[53] Derek Hull and David J. Bacon. *Introduction to dislocations*. Butterworth-Heinemann, 2001.

[54] J. Huang, H. Xing, and J. Sun. Structural stability and generalized stacking fault energies in β Ti–Nb alloys: Relation to dislocation properties. *Scripta Materialia*, 66(9):682–685, May 2012.

[55] Martina Dikovits, Cecilia Poletti, and Fernando Warchomicka. Deformation Mechanisms in the Near-β Titanium Alloy Ti-55531. *Metallurgical and Materials Transactions A*, 45(3):1586–1596, March 2014.

[56] Juan Zhao, Jie Zhong, Fei Yan, Fang Chai, and Matthew Dargusch. Deformation behaviour and mechanisms during hot compression at supertransus temperatures in Ti-10v-2fe-3al. *Journal of Alloys and Compounds*, 710:616–627, 2017.

[57] Takashi Saito, Tadahiko Furuta, Jung-Hwan Hwang, Shigeru Kuramoto, Kazuaki Nishino, Nobuaki Suzuki, Rong Chen, Akira Yamada, Kazuhiko Ito, Yoshiki Seno, Takamasa Nonaka, Hideaki Ikehata, Naoyuki Nagasako, Chihiro Iwamoto, Yuuichi Ikuhara, and Taketo Sakuma. Multifunctional Alloys Obtained via a Dislocation-Free Plastic Deformation Mechanism. *Science*, 300(5618):464–467, April 2003.

[58] Tadahiko Furuta, Shigeru Kuramoto, Junghwan Hwang, Kazuaki Nishino, and Takashi Saito. Elastic Deformation Behavior of Multi-Functional Ti–Nb–Ta–Zr–O Alloys. *Materials Transactions*, 46(12):3001–3007, 2005.

[59] S. Kuramoto, T. Furuta, J. H. Hwang, K. Nishino, and T. Saito. Plastic Deformation in a Multifunctional Ti-Nb-Ta-Zr-O Alloy. *Metallurgical and Materials Transactions: Physical Metallurgy and Materials Science, A; New York*, 37A(3):657–662, March 2006.

[60] W. Guo, M. Z. Quadir, S. Moricca, T. Eddows, and M. Ferry. Microstructural evolution and final properties of a cold-swaged multifunctional Ti–Nb–Ta–Zr–O alloy produced by a powder metallurgy route. *Materials Science and Engineering: A*, 575:206–216, July 2013.

[61] W. Y. Guo, H. Xing, J. Sun, X. L. Li, J. S. Wu, and R. Chen. Evolution of Microstructure and Texture during Recrystallization of the Cold-Swaged Ti-Nb-Ta-Zr-O Alloy. *Metallurgical and Materials Transactions A*, 39(3):672–678, March 2008.

[62] Metalary - Latest and Historical Metal Prices.

[63] Dalibor Preisler. *Metastabilní beta slitiny titanu pro využití v biomedicíně*. Bachelor Thesis, Univerzita Karlova, Praha, 2016.

[64] Dalibor Preisler, Kristína Václavová, Josef Stráský, Miloš Janeček, and Petr Harcuba. Microstructure and mechanical properties of Ti-Nb-Zr-Ta-O biomedical alloy. *METAL 2016: 25rd International Conference on Metallurgy and Materials. Ostrava: TANGER*, pages 1509–1513, 2016.

[65] Matt Danford. Pursuing Perfection with Cold-Formed Cavities, January 2016.

[66] J. Goldstein, D. E. Newbury, P. Echlin, D. C. Joy, A. D. Romig Jr, C. E. Lyman, C. Fiori, and E. Lifshin. *Scanning electron microscopy and X-ray microanalysis: a text for biologists, materials scientists, and geologists*. Springer Science & Business Media, 2012.

[67] James H. Wittke. Signals - Electron Microanalysis Core Facility - Northern Arizona University, 2016.

[68] EN ISO. 6507-1: 2005-Metallic materials-Vickers hardness test. *European Committee for Standardization*, 2006.

[69] ASTM E1876-15. *Standard Test Method for Dynamic Young's Modulus, Shear Modulus, and Poisson's Ratio by Impulse Excitation of Vibration*. ASTM International, West Conshohocken, PA, 2015.

[70] David A. Porter, Kenneth E. Easterling, and Mohamed Sherif. *Phase Transformations in Metals and Alloys, (Revised Reprint)*. CRC press, 2009.

[71] Robert Pederson, Raghuveer Gaddam, and Marta-Lena Antti. Microstructure and mechanical behavior of cast Ti-6al-4v with addition of boron. *Central European Journal of Engineering*, 2(3):347–357, September 2012.

[72] Sung-Il Kim and Yeon-Chul Yoo. Dynamic recrystallization behavior of AISI 304 stainless steel. *Materials Science and Engineering: A*, 311(1):108–113, July 2001.

[73] W.-Y. Guo, J. Sun, X.-L. Li, and J.-S. Wu. Microstructures of Ti-Nb-Ta-Zr-O alloy deformed and recrystallized. *Zhongguo Youse Jinshu Xuebao/Chinese Journal of Nonferrous Metals*, 18(9):1634–1638, 2008.

[74] Andrzej Stefanik, Piotr Szota, Sebastian Mróz, Teresa Bajor, and Sonia Boczkal. Influence of the Deformation Method on the Microstructure Changes in AZ31 Magnesium Alloy Round Rods Obtained by the Rolling Process. *Key Engineering Materials*, 716:864–870, October 2016.

[75] V. V. Balasubrahmanyam and Y. V. R. K. Prasad. Hot deformation mechanisms in metastable beta titanium alloy Ti–10v–2fe–3al. *Materials Science and Technology*, 17(10):1222–1228, 2001.

[76] J. Hwang, S. Kuramoto, T. Furuta, K. Nishino, and T. Saito. Phase-stability dependence of plastic deformation behavior in Ti-Nb-Ta-Zr-O alloys. *Journal of Materials Engineering and Performance*, 14(6):747–754, December 2005.

[77] Wei-dong ZHANG, Yong LIU, Hong WU, Bin LIU, Zi-jin CHEN, and Huiping TANG. Microstructural evolution during hot and cold deformation of Ti–36nb–2ta–3zr–0.35o alloy. *Transactions of Nonferrous Metals Society of China*, 26(5):1310–1316, May 2016.

[78] W. Guo, M. Z. Quadir, and M. Ferry. The Mode of Deformation in a Cold-Swaged Multifunctional Ti-Nb-Ta-Zr-O Alloy. *Metallurgical and Materials Transactions A*, 44(5):2307–2318, May 2013.

[79] M. J. Bermingham, S. D. McDonald, A. J. Buddery, D. H. StJohn, and M. S. Dargusch. Processing considerations for cast Ti–25nb–3mo–3zr–2sn biomedical alloys. *Materials Science and Engineering: C*, 31(7):1520–1525, October 2011.

[80] Thorium dioxide, September 2017. Page Version ID: 800204462.

[81] J. I. Qazi, V. Tsakiris, B. Marquardt, and H. J. Rack. Effect of aging treatments on the tensile properties of Ti-35nb-7zr-5ta-(0.06-0.7)O alloys. In *Titanium, Niobium, Zirconium, and Tantalum for Medical and Surgical Applications*. ASTM International, 2006.

[82] J. I. Qazi, H. J. Rack, and B. Marquardt. High-strength metastable beta-titanium alloys for biomedical applications. *JOM*, 56(11):49–51, November 2004.

List of Abbreviations

AR	area reduction
ARS	acoustic resonant spectroscopy
BSE	back-scattered electrons
bcc	base-centered cubic (structure)
CI	confidence index
CR	cold rolling
CSW	cold-swaging
CW	cold working
e/a	number of electrons per atom
EBSD	electron back-scatter diffraction
FL	fatigue limit
GOS	grain orientation spread
hcp	hexagonal close packed (structure)
IPF	inverse pole figure
IQ	image quality
KAM	kernel average misorientation
PF	pole figure
RT	room temperature
RUS	resonant ultrasound spectroscopy
SE	secondary electrons
SEM	scanning electron microscope
SFE	stacking fault energy
SIM	stress induced martensite
TM	thermomechanical (processing)
T_m	melting temperature
TNTZO	Ti-35Nb-6Ta-7Zr-0.7O (wt.%)
TPTS	total plastic true strain
UCS	ultimate compressive strength
UTS	ultimate tensile strength
WQ	water quenching
YM	Young's modulus
YS	yield strength

Attachments

Attachment 1: Review of composition, preparation route, mechanical properties and phase composition of Ti-Nb based alloys.

Composition (%)	O content (%)	TM treatment	YM (GPa)	YS (MPa)	UTS (MPa)	Micro-hardness (HV)	Phase composition	Ref.
Ti-35.6Nb-2.1Ta-3.0Zr	0.32	CR 90 % + ST 850 °C 30 min WQ	60	830	880	-	β	[25]
Ti-35.8Nb-2.1Ta-3.1Zr	-	CR 90 % + ST 850 °C 30 min WQ	55	280	400	-	$\beta + \alpha$”	[25]
Ti-28.3Nb-11.1Ta-5.1Zr	-	CR 75 % + ST 750 °C 30 min WQ	63	-	320	-	β	[26]
Ti-28.3Nb-11.1Ta-5.1Zr	-	CR 75 %	66	-	700	-	β	[26]
Ti-28.3Nb-11.1Ta-5.1Zr	-	CR 75 % + aging 400 °C 10 min	42	-	430	-	$\beta + \omega$	[26]
Ti-35.9Nb-6.9Zr	-	CR 75 % + ST 750 °C 30 min WQ	67	-	350	-	β	[26]
Ti-35.9Nb-6.9Zr	-	CR 75 %	64	-	700	-	β	[26]
Ti-35.9Nb-6.9Zr	-	CR 75 % + aging 400 °C 10 min	50	-	710	-	-	[26]

Composition (%)	O content (%)	TM treatment	YM (GPa)	YS (MPa)	UTS (MPa)	Micro-hardness (HV)	Phase composition	Ref.
Ti-36.9Nb	-	CR 75 % + ST 750 °C 30 min WQ	60	-	420	-	$\beta + \alpha$"	[26]
Ti-36.9Nb	-	CR 75 %	47	-	600	-	$\beta + \alpha$"	[26]
Ti-36.9Nb	-	CR 75 % + aging 400 °C 10 min	42	-	640	-	$\beta + \omega$	[26]
Ti-35.8Nb-2.1Ta-3.1Zr	0.32	ST 1000 °C 1 h WQ	70	750	-	260	β	[58]
Ti-35.8Nb-2.1Ta-3.1Zr	0.32	ST 1000 °C 1 h WQ + CSW 20 %	60	900	-	260	β	[58]
Ti-35.8Nb-2.1Ta-3.1Zr	0.32	ST 1000 °C 1 h WQ + CSW 40 %	58	900	-	260	β	[58]
Ti-35.8Nb-2.1Ta-3.1Zr	0.32	ST 1000 °C 1 h WQ + CSW 60 %	55	900	-	260	β	[58]
Ti-35.8Nb-2.1Ta-3.1Zr	0.32	ST 1000 °C 1 h WQ + CSW 80 %	55	950	-	260	β	[58]
Ti-35.8Nb-2.1Ta-3.1Zr	0.32	ST 1000 °C 1 h WQ + CSW 90 %	55	1050	-	260	β	[58]

Composition (%)	O content (%)	TM treatment	YM (GPa)	YS (MPa)	UTS (MPa)	Micro-hardness (HV)	Phase composition	Ref.
Ti-30.0Nb-2.0Ta-2.7Zr	0.49	ST 1050 °C 30 min WQ + CSW 96 %	58	-	1100	-	$\beta + \omega$	[44]
Ti-31.9Nb-2.1Ta-2.7Zr	0.49	ST 1050 °C 30 min WQ + CSW 96 %	55	-	1200	-	β	[44]
Ti-32.9Nb-2.0Ta-2.7Zr	0.49	ST 1050 °C 30 min WQ + CSW 96 %	50	-	1250	-	-	[44]
Ti-33.9Nb-2.1Ta-2.7Zr	0.49	ST 1050 °C 30 min WQ + CSW 96 %	51	-	1300	-	β	[44]
Ti-36.1Nb-2.2Ta-2.7Zr	0.47	ST 1050 °C 30 min WQ + CSW 96 %	60	-	1500	-	β	[44]
Ti-28.7Nb-12.7Ta-4.4Zr	0.14	Hot rolling 1000 °C 83 % AC	65	400	650	220	β	[27]
Ti-28.7Nb-12.7Ta-4.4Zr	0.14	Hot rolling 1000 °C 83 % AC + ST 730 °C 1 h WQ	60	350	600	200	β	[27]
Ti-28.7Nb-12.8Ta-4.6Zr	0.33	Hot rolling 1000 °C 83 % AC	65	650	870	250	β	[27]

Composition (%)	O content (%)	TM treatment	YM (GPa)	YS (MPa)	UTS (MPa)	Micro-hardness (HV)	Phase composition	Ref.
Ti-28.7Nb-12.8Ta-4.6Zr	0.33	Hot rolling 1000 °C 83 % AC + ST 810 °C 1 h WQ	65	700	800	230	β	[27]
Ti-28.9Nb-12.7Ta-4.7Zr	0.70	Hot rolling 1000 °C 83 % AC	75	1050	1050	370	β	[27]
Ti-28.9Nb-12.7Ta-4.7Zr	0.70	Hot rolling 1000 °C 83 % AC + ST 970 °C 1 h WQ	75	1050	1050	360	β	[27]
Ti-35.8Nb-2.1Ta-3.1Zr	0.32	CR 90 % + ST 850 °C 30 min WQ	60	830	880	-	β	[37]
Ti-36.8Nb-2.0Ta-2.7Zr	0.44	ST 1000 °C 1 h WQ + CSW 96 %	45	880	940	280	$\beta + \omega$	[78]
Ti-30.0Nb-12.0Zr	0.08	Forging 850 °C + ST 850 °C 30 min WQ	67	non-linear	545	194	$\beta + \alpha" + \omega$	[29]
Ti-30.0Nb-12.0Zr	0.09	Forging 850 °C + ST 850 °C 30 min WQ	64	non-linear	720	204	$\beta + \alpha" + \omega$	[29]
Ti-30.0Nb-12.0Zr	0.20	Forging 850 °C + ST 850 °C 30 min WQ	67	non-linear	675	245	$\beta + \alpha" + \omega$	[29]

Composition (%)	O content (%)	TM treatment	YM (GPa)	YS (MPa)	UTS (MPa)	Micro-hardness (HV)	Phase composition	Ref.
Ti-30.0Nb-12.0Zr	0.29	Forging 850 °C + ST 850 °C 30 min WQ	68	non-linear	720	275	$\beta + \alpha" + \omega$	[29]
Ti-30.0Nb-12.0Zr	0.37	Forging 850 °C + ST 850 °C 30 min WQ	69	non-linear	850	286	$\beta + \alpha" + \omega$	[29]
Ti-30.0Nb-12.0Zr	0.50	Forging 850 °C + ST 850 °C 30 min WQ	72	non-linear	995	306	$\beta + \alpha" + \omega$	[29]
Ti-35.2Nb	0.41	CSW 98.5 %	-	non-linear	1300	-	-	[30]
Ti-35.2Nb	0.41	CSW 98.5 % + ST 900 °C 30 min WQ	-	450	900	-	-	[30]
Ti-35.2Nb	0.55	CSW 98.5 %	-	non-linear	1370	-	-	[30]
Ti-35.2Nb	0.55	CSW 98.5 % + ST 900 °C 30 min WQ	-	500	1050	-	-	[30]
Ti-35.3Nb	0.14	CSW 98.5 %	-	non-linear	950	-	-	[30]
Ti-35.3Nb	0.14	CSW 98.5 % + ST 900 °C 30 min WQ	-	170	700	-	-	[30]

Composition (%)	O content (%)	TM treatment	YM (GPa)	YS (MPa)	UTS (MPa)	Micro-hardness (HV)	Phase composition	Ref.
Ti-35.3Nb	0.28	CSW 98.5 %	-	non-linear	1150	-	-	[30]
Ti-35.3Nb	0.28	CSW 98.5 % + ST 900 °C 30 min WQ	-	350	850	-	β	[30]
Ti-35.4Nb	-	CSW 98.5 %	-	non-linear	700	-	-	[30]
Ti-35.4Nb	-	CSW 98.5 % + ST 900 °C 30 min WQ	-	350	500	-	-	[30]
Ti-29.0Nb-13.2Ta-4.7Zr	0.12	ST 790 °C 1 h WQ	58	500	600	180	β	[46]
Ti-29.0Nb-13.2Ta-4.7Zr	0.12	ST 790 °C 1 h WQ + aging 450 °C 72 h WQ	88	900	1000	275	$\beta + \alpha$	[46]
Ti-29.1Nb-12.7Ta-4.5Zr	0.20	ST 800 °C 1 h WQ	70	600	700	195	β	[46]
Ti-29.1Nb-12.7Ta-4.5Zr	0.20	ST 800 °C 1 h WQ + aging 450 °C 72 h WQ	93	1200	1250	325	$\beta + \alpha$	[46]
Ti-29.3Nb-12.8Ta-4.4Zr	0.42	ST 820 °C 1 h WQ	75	840	900	210	β	[46]

Composition (%)	O content (%)	TM treatment	YM (GPa)	YS (MPa)	UTS (MPa)	Micro-hardness (HV)	Phase composition	Ref.
Ti-29.3Nb-12.8Ta-4.4Zr	0.42	ST 820 °C 1 h WQ + aging 450 °C 72 h WQ	98	1300	1400	370	$\beta + \alpha$	[46]
Ti-34.6Nb-5.6Ta-7.1Zr	0.68	ST 900 °C 30 min WQ	-	1081	1097	-	β	[82]
Ti-34.6Nb-5.6Ta-7.1Zr	0.68	ST 900 °C 30 min WQ + aging 427 °C 8 h AC	-	1222	1252	-	$\beta + \alpha$	[82]
Ti-34.6Nb-5.6Ta-7.1Zr	0.68	ST 900 °C 30 min WQ + aging 482 °C 8 h AC	-	1288	1362	-	-	[82]
Ti-34.6Nb-5.6Ta-7.1Zr	0.68	ST 900 °C 30 min WQ + aging 538 °C 8 h AC	-	1036	1180	-	-	[82]
Ti-34.6Nb-5.6Ta-7.1Zr	0.68	ST 900 °C 30 min WQ + aging 593 °C 8 h AC	-	893	1036	-	-	[82]
Ti-34.6Nb-5.6Ta-7.1Zr	0.68	ST 900 °C 30 min WQ + aging 260 °C 4 h AC + aging 427 °C 8 h AC	-	1234	1260	-	$\beta + \alpha$	[82]
Ti-34.6Nb-5.6Ta-7.3Zr	0.46	ST 840 °C 30 min WQ	-	937	1014	-	β	[82]
Ti-34.6Nb-5.6Ta-7.3Zr	0.46	ST 840 °C 30 min WQ + aging 427 °C 8 h AC	-	1007	1055	-	$\beta + \alpha + \omega$	[82]

Composition (%)	O content (%)	TM treatment	YM (GPa)	YS (MPa)	UTS (MPa)	Micro-hardness (HV)	Phase composition	Ref.
Ti-34.6Nb-5.6Ta-7.3Zr	0.46	ST 840 °C 30 min WQ + aging 482 °C 8 h AC	-	1060	1149	-	-	[82]
Ti-34.6Nb-5.6Ta-7.3Zr	0.46	ST 840 °C 30 min WQ + aging 538 °C 8 h AC	-	806	929	-	-	[82]
Ti-34.6Nb-5.6Ta-7.3Zr	0.46	ST 840 °C 30 min WQ + aging 593 °C 8 h AC	-	765	861	-	-	[82]
Ti-34.6Nb-5.6Ta-7.3Zr	0.46	ST 840 °C 30 min WQ + aging 260 °C 4 h AC + aging 427 °C 8 h AC	-	1202	1244	-	$\beta + \omega$	[82]
Ti-35.3Nb-4.9Ta-7.2Zr	0.06	ST 850 °C 30 min WQ	-	530	590	-	β	[82]
Ti-35.3Nb-4.9Ta-7.2Zr	0.06	ST 850 °C 30 min WQ + aging 427 °C 8 h AC	-	630	686	-	$\beta + \omega$	[82]
Ti-35.3Nb-4.9Ta-7.2Zr	0.06	ST 850 °C 30 min WQ + aging 482 °C 8 h AC	-	503	534	-	-	[82]
Ti-35.3Nb-4.9Ta-7.2Zr	0.06	ST 850 °C 30 min WQ + aging 538 °C 8 h AC	-	493	537	-	-	[82]
Ti-35.3Nb-4.9Ta-7.2Zr	0.06	ST 850 °C 30 min WQ + aging 593 °C 8 h AC	-	508	549	-	-	[82]

Composition (%)	O content (%)	TM treatment	YM (GPa)	YS (MPa)	UTS (MPa)	Micro-hardness (HV)	Phase composition	Ref.
Ti-35.3Nb-4.9Ta-7.2Zr	0.06	ST 850 °C 30 min WQ + aging 260 °C 4 h AC + aging 427 °C 8 h AC	-	593	753	-	$\beta + \omega$	[82]
Ti-35.3Nb-5.7Ta-7.3Zr	0.06	Forging 1100 °C + ST 1000 °C 2 h WQ	65	450	550	163	β	[41]
Ti-35.3Nb-5.7Ta-7.3Zr	0.40	Forging 1100 °C + ST 1000 °C 2 h WQ	81	850	900	270	β	[41]
Ti-35.3Nb-5.7Ta-7.3Zr	0.70	Forging 1100 °C + ST 1000 °C 2 h WQ	80	1000	1200	330	β	[41]
Ti-34.2Nb-2.1Ta-3.1Zr	0.09	ST 850 °C 30 min WQ	69	-	-	-	$\beta + \alpha$"	[51]
Ti-35.2Nb-2.0Ta-2.9Zr	0.51	ST 1050 °C 30 min WQ	67	-	-	-	β	[51]
Ti-35.6Nb-2.1Ta-2.7Zr	0.30	ST 850 °C 30 min WQ + CSW 90 %	65	-	-	-	β	[51]
Ti-36.1Nb-2.2Ta-2.7Zr	0.47	ST 1050 °C 30 min WQ + CSW 90 %	67	-	-	-	β	[51]
Ti-36.3Nb-2.1Ta-2.9Zr	0.36	ST 850 °C 30 min WQ	67	-	-	-	β	[51]

Composition (%)	O content (%)	TM treatment	YM (GPa)	YS (MPa)	UTS (MPa)	Micro-hardness (HV)	Phase composition	Ref.
Ti-36.5Nb-1.6Ta-2.8Zr	0.06	ST 850 °C 30 min WQ + CSW 90 %	67	-	-	-	$\beta + \alpha$"	[51]
Ti-35.0Nb-2.1Ta-3.1Zr	-	Hot rolling 950 °C + ST 780 °CC 30 min AC	56	300	540	-	β	[47]
Ti-35.0Nb-2.1Ta-3.1Zr	0.13	Hot rolling 950 °C + ST 780 °CC 30 min AC	59	750	770	-	β	[47]
Ti-35.0Nb-2.1Ta-3.1Zr	0.27	Hot rolling 950 °C + ST 780 °CC 30 min AC	65	650	750	-	β	[47]
Ti-35.0Nb-2.1Ta-3.1Zr	0.40	Hot rolling 950 °C + ST 780 °CC 30 min AC	60	800	840	-	β	[47]
Ti-35.0Nb-2.1Ta-3.1Zr	0.53	Hot rolling 950 °C + ST 780 °CC 30 min AC	90	860	883	-	β	[47]